

THESE DE DOCTORAT  
présentée à

L'UNIVERSITE DE LILLE 1

Ecole Doctoral Régionale Sciences Pour l'Ingénieur Lille Nord-de-France



pour obtenir le grade de

DOCTEUR EN SCIENCES

Dans la spécialité:

Micro et Nano Technologies, Acoustique et Télécommunications  
par

VOLODYMYR TURCHENIUK

# Functionalization and modification of nanoparticles and their biomedical application

Soutenue le 3 OCTOBER 2016 devant le jury composé de :

Rapporteurs : Olga ZAPOROZHET, Professeur, Kiev National University,  
Cyrille GRANDJEAN, Chargé de Recherche, Université de Nantes,

Directeur de Thèse : Pr. Sabine SZUNERITS, Professeur, Université Lille 1

Co-Directeur de Thèse : Pr. Vladimir ZAITSEV, Professeur, Kiev National University



## ACKNOWLEDGEMENT

Over the past two years, I have received support and encouragement from great number of individuals to make my academic stay in France fruitful.

First of all, I would like to give my warmest gratitude to my Ph.D. supervisor Prof. Sabine Szunerits for her continued support, guidance, scientific discussion and encouragement throughout my study period and le I was fortunate to find her not only as a mentor but also as a guardian thousand miles from my country, Ukraine. Her guidance has made this journey thoughtful and rewarding. I am also very grateful to her for providing me opportunities to explore researches and to learn different techniques in other labs outside France.

Of course deepest thanks to Prof. Vladimir Zaitsev, he always supported me and when I was in panic I could ask him and then everything started to be fine.

My deepest thanks go to Dr. Rabah Boukherroub for his suggestions, sharpening my scientific thinking which is essential for research field and for organizing lab meeting every week which helped me to learn different techniques and to broaden my knowledge in material science research.

I would like to thank Dr. Aloysius Siriwardena for suggestions and scientific discussions that he shared to us via email and phone and being available even after his busy schedule whenever I need to discuss my work. It was big pleasure to work with him. Sadly, he passed away recently and this work is thus dedicated to him, as his input was of high importance.

I would like to thank Dr. Alexandre Barras for his valuable suggestions during my research work. He always helped me when I didn't know something

Also, I would like to thanks Amer, Pawan, Roxane, Flori, Nadia, Wang Qi, and all the lab members for maintaining the ambiance and peaceful working environment in lab and I truly appreciate the nature of sharing the ideas among lab mates. Special for Amer and Pawan for making me company outside the laboratory)

I would like to thank all the Ukrainian friends in Lille and in Ukraine specially; Ugeen and Svitlana for care, giving me company during my hard and good times, Alexandre and polish guy Artour for a lot of fun days. I will definitely miss the gathering and fun with you all.

I am always grateful to my mother, grandmother, brother who has supported my decision to study miles away from hometown, kept patience for years, and provided continuous emotional support and inspiration.

And the biggest gratitude for my brother Dr. Kostiantyn Turcheniuk, without him there would be no PhD) Sometime he was angry on me and forced me to work; but I very much appreciate it at the end.

Another biggest gratitude for my first teacher. Without her I've never started to study chemistry.

I have no words to explain my gratitude to my beloved girlfriend for continuous support, encouragement and keeping faith on me during my academic carrier. She has taught me to stay positive even in the worst condition. I am indebted to his unconditional love and understanding nature despite of long distance relationship.

## ABSTRACT

Functionalized nanoparticles continue to attract interest in biomedical applications and bioassays and have become a key focus in nanobiotechnology research. The use of nanomaterials in biomedical applications is of great interest since their size scale is similar to biological molecules and structures. One of the primary focus of the research work was the development of versatile surface functionalization strategies for different nanoparticles ranging from diamond nanostructures to gold nanorods and nanocomposites.

One particular aim was the use of reduced graphene oxide (rGO) and silica coated gold nanorods for the photothermal and photodynamic ablation of pathogens. Embedding of verteporfin, a clinically approved photosensitizer, into silica-coated gold nanorods allowed an efficient eradication of a virulent strain of *E. coli* associated with urinary tract infection. The great heating effect of graphene-coated gold nanorods when illuminated with a near-infrared laser allowed for a photothermal destruction of the same pathogenic strain.

In parallel, we have shown the interest of using diamond nanoparticles (NDs) modified with menthol as well as different sugars as antibacterial agent against Gram-positive (*Staphylococcus aureus*) and Gram-negative (*Escherichia Coli*) bacteria. We developed a strategy for the covalent attachment of sugars by taking advantage of the photochemistry of arylazides, which upon light activation convert to reactive nitrenes. The highly reactive nitrene intermediate formed is believed to interact with glycans through C-H and N-H insertion reactions, creating highly robust covalent linkages. The resulting glyco-NDs maintained their expected binding affinity and specificity towards their partner lectins. Through a fluorescent based agglutination assay, we showed that mannan-NDs display *E. coli* agglutination at concentrations of  $\approx 10 \mu\text{g mL}^{-1}$ , being much lower than free mannan and mannose-NDs.

## TABLE OF CONTENT

<b>ACRONYMS</b>	<b>10</b>
<b>OBJECTIVES</b>	<b>12</b>

### **CHAPTER I: Nanoparticles for biological applications**

1.1. Introduction	16
1.2. Gold nanoparticles (GNPs)	17
1.2.1. Introduction	17
1.2.2. Plasmonic photothermal therapy	20
1.2.3. Photodynamic treating with GNPs	22
1.3. Nanodiamonds (NDs)	23
1.4. References	28

### **CHAPTER II: Glycans-Modified Nanodiamonds**

2.1. Introduction	32
2.2. Synthesis of glyco-NDs via photoactivation of perfluorophenylazide-modified NDs	35
2.3. Lectin binding assays	42
2.4. Effect of mannose-NDs and mannan-NDs on agglutination of <i>E. coli</i> UTI89 strains	44
2.4.1. Fluorescence-based agglutination assay in the presence of mannose and mannose-NDs	44
2.4.2. Fluorescence-based agglutination assay in the presence of mannan and mannan-NDs	45
2.5. Conclusions	46
2.6. References	47

### **CHAPTER III: Menthol Modified Nanodiamonds and their antibacterial properties**

3.1. Introduction	49
3.2. Synthesis and physico-chemical properties of ND-Menthol particles	50
3.3. Antimicrobial activity of the ND-menthol particles	53
3.4. Conclusions	58
3.5. References	58

### **CHAPTER IV: Highly effective photodynamic eradication of *Escherichia Coli* pathogenic organisms by using golden nanorods/SiO<sub>2</sub> core-shell nanostructures with included verteporfin**

4.1 Introduction	63
4.2 Synthesis and photodynamic properties of AuNRs@SiO <sub>2</sub> VP	64
4.3. Conclusions	70
4.4. References	70

## **CHAPTER V: Plasmonic photothermal cancer therapy with gold nanorods/reduced graphene oxide core/shell nanocomposites**

5.1. Introduction	74
5.2. Synthesis and physic-chemical properties of AuNRs@rGO particles	75
5.3. Photothermal features of Au NRs@rGO-PEG and photothermal eradication cells of UM87MG <i>in vitro</i> .	78
5.4. NIR fluorescence imaging and biodistribution	83
5.5. <i>In vivo</i> photothermal therapy of mice with implanted cells of U87MG tumors.	86
5.6. Conclusions	88
5.7. References	89

## **CHAPTER VI: Reduced graphene oxide nanosheets decorated with AuPd bimetallic nanoparticles : a multioperational material for the Photothermal Treatment of Cancer Cells**

6.1. Introduction	93
6.2. Synthesis and characteristics of AuPd NPs-rGO-Peg nanocomposites	94
6.3. Photothermal efficacy and photothermal removing of cancer cells	99
6.4. Conclusions	102
6.5. References	102

## **CHAPTER VII: CONCLUSIONS AND PERSPECTIVES** **106**

### **APPENDIX**

#### **Experimental Part** **109**

7.1. Materials	109
7.2. Synthesis of organic compounds	110
7.2.1. Synthesis of menthol derivative (2)	110
7.2.2. Synthesis of 4-azido-N-(3,4-dihydroxyphenethyl)-2,3,5,6-tetrafluorobenzamide (1)	111
7.2.2.1. 4-Azidotetrafluorobenzoic acid	111
7.2.2.2. N-Succinimidyl-4-azidotetrafluorobenzoate	111
7.2.2.3 4-azido-N-(3,4-dihydroxyphenethyl)-2,3,5,6-tetrafluorobenzamide	112
7.3. Synthesis of nanoparticles	112
7.3.1 Nanodiamonds (NPs)	112
7.3.1.1. Formation of ND-PFPA	112
7.3.1.2. Photochemical linkage of glycans to ND-PFPA	112
7.3.1.3. Preparation of menthol-modified NDs (ND-menthol)	112
7.3.2. Gold nanoparticles (Au NPs)	113
7.3.2.1. Synthesis of gold nanorods (AuNRs)	113
7.3.2.2. Preparation of AuNRs@SiO <sub>2</sub> particles	113
7.3.2.3. Loading of AuNRs@SiO <sub>2</sub> particles with verteporfin (VP)	114
7.3.2.4. Synthesis of pegilated rGO-wrapped gold nanorods (AuNRs@rGO-PEG)	114

7.3.2.5. Conjugation of AuNRs@rGo-PEG with Cy7 or FITC and Tat protein vector	115
7.3.2.6. Synthesis of AuPd NPs-rGO nanocomposite materials	115
7.3.2.7. Functionalization of AuPd NPs@rGO with polyethylene glycol (PEG)	115
7.4 Determination of carbohydrate loading on the NDs	117
7.5 Lectin binding assay	117
7.6. Fluorescence-based agglutination assay	118
7.7. Biological assay	118
7.7.1. Antimicrobial assays	118
7.7.2. Cell culture and cellular uptake of Au NRs@rGO-PEG-FITC and Au NRs@rGO-PEG-Tat/FITC	120
7.7.3. Cellular toxicity of AuNrs@rGO-PEG	120
7.8. Photothermal experiments	121
7.8.1. <sup>1</sup> O <sub>2</sub> quantum yield estimation	121
7.8.2. Single oxygen detection	121
7.8.3. Photodynamic ablation of bacteria solutions	121
7.8.4. Photothermal <i>in vitro</i> experiment	122
7.8.5. <i>In vivo</i> photothermal therapy and histology	122
7.9. Instrumentations	123
7.9.1. Fourier transformed infrared spectroscopy	123
7.9.2. Micro-Raman spectroscopy	124
7.9.3. X-ray photoelectron spectroscopy	124
7.9.4. Absorption spectra	124
7.9.5. Transmission electron microscope (TEM)	124
7.9.6. Scanning electron microscope (SEM)	125
7.9.7. Confocal microscopy	125
7.9.8. Thermogravimetric analysis (TGA)	125
7.9.9. Particle size measurements	125
7.9.10. Measurements of the photothermal effect	126

## List of publications

127

## ACRONYMS

ACN	Acetonitrile
APTMS	4-aminopropyltrimethoxysilane
ATP	Adenosine triphosphate
Au NRs	Gold nanorods
Au NRs@rGO-PEG	Pegylated reduced graphene oxide wrapped gold nanorods
BSA	Bovine serum albumin
CDCl <sub>3</sub>	Deuterated chloroform
CMC	Critical micellar concentration
Cu (I)	Copper iodide
CuI(PPh <sub>3</sub> )	Copper iodide triphenylphospine
DAPI	4'-6-diamidino-2-phenylindole
DCC	N,N'-dicyclohexylcarbodiimide
DCM	Dichloromethane
DMAEMA	2-(Dimethylamino)ethyl methacrylate
DMAP	4-Dimethylaminopyridine
DMEM	Dulbecco modified Eagle medium
DMF	Dimethylformamide
DMSO	Dimethyl sulfoxide
DNA	Deoxyribonucleic acid
DOP-N <sub>3</sub>	Azide-terminated dopamine derivative
DOP-PEG	Polyethylene glycol-terminated dopamine derivative
DSPE	1,2-distearoyl- <i>sn</i> -glycero-3-phosphoethanolamine- N-[carboxylic acid (polyethylene-glycol)]
E.coli	<i>Echerichia coli</i> ( <i>Katushka</i> )
EDTA	Ethylenediaminetetraacetic acid
EDC	<i>N</i> -(3-Dimethylaminopropyl)- <i>N'</i> -ethylcarbodiimide hydrochloride
ER	Endoplasmic reticulum
EPR	Enhanced permeability and retention
ESI	Electron spray ionization
EtoAc	Ethyl acetate
FCS	Fetal calf serum
FDA	Food and Drug Administration
FT-IR	Fourier transformed-infrared spectroscopy
GFP	Green fluorescence protein
GNPs	Gold nanoparticles
G-Ins	Gluconic acid-modified insulin
HCC	Hepatocellular carcinoma
HCV	Hepatitis C Virus
HCVcc	HCV cell culture systems
HCVpp	HCV pseudotyped particles
Hex	Hexane
HIV	Human Immunodeficiency Virus

HLB	Hydrophilic lipophilic balance
HNO <sub>3</sub>	Nitric acid
H <sub>2</sub> SO <sub>4</sub>	Sulfuric acid
HS	Heparin sulfate
HTS	High throughput screening
Huh-7	Hepatocyte derived cellular carcinoma cell line
IFN $\alpha$	Interferon-alpha
IC <sub>50</sub>	Half maximal inhibitory concentration
IRES	Internal ribosome entry site
JAM	Junction-associated adhesion molecule
JFH	Japanese Fulminant Hepatitis
KBr	Potassium bromide
LDLR	Low-density lipoprotein receptor
LiAlH <sub>4</sub>	Lithium aluminium hydride
LNCs	Lipid nanocapsules
MAb	Monoclonal antibody
Man-9	Mannanose-di-(N-acetyl-D-glucosamine)
MLV	Murin leukemia virus
MPS	Mesoporous silica
MPS	Mononuclear phagocyte system
MRI	Magnetic resonance imaging
MTS	Cell Proliferation Assay
nAb	Neutralizing antibody
NaCl	Sodium chloride
NaOH	Sodium hydroxide
NC	Non-coding
NDs	Nanodiamonds
ND-PFPA	Pentafluorozidobenzoate modified nanodiamond
NHS	<i>N</i> -Hydroxysuccinimide
NH <sub>2</sub> -PEG-NH <sub>2</sub>	Poly(ethylene glycol)bis(3-aminopropyl)
NIH	National Institute of Health
NMR	Nuclear magnetic resonance
NPs	Nanoparticles
NPC	Nuclear pore complexes
NS	Non-structural
(N-V)-	Nitrogen-vacancy center
PBS	Phosphate buffer saline
pDNA	Plasmid deoxyribonucleic acid
PEG	Polyethylene glycol
PEI	Polyethylenimine
PET	Positron emission tomography
PDI	Polydispersity index
PIT	Phase-inversion temperature
pKa	Ionization constant

PLGA	Poly(lactic- <i>co</i> -glycolic acid)
PLL	Poly-L-lysine
PS-ON	Phosphorothioate oligonucleotides
Rcf	Relative centrifugal force
RISC	RNA-induced silencing complex
RNA	Ribonucleic acid
ROS	Reactive oxygen species
SEM	Scanning electron microscope
siRNA	Silencer RNA
SOCl <sub>2</sub>	Thionyl chloride
SRB1	Scavenger receptor class B type 1
SPIO	Superparamagnetic iron oxide nanoparticle
TEA	Triethylamine
TEM	Transmission electron microscope
TEOS	Tetraethyl orthosilicate
TGA	Termogravimetric analysis
THF	Tetrahydrofuran
THP-1	Human macrophage-like cells
TNF	Tumor necrosis factor
UTR	3'Untranslated region
VP	Verteporfin
VSVg	Vesicular stomatitis virus glycoprotein G
XPS	X-ray photoelectron spectroscopy
ZO	Zona occludens

## OBJECTIVES

The past decade has observed significant advancement in the field of nanobiotechnology. Functionalized nanoparticles continue to attract interest in biomedical applications and bioassays and have become a key focus in nanobiotechnology research. The use of nanomaterials in biomedical applications is of great interest since their size scale is similar to biological molecules and structures. Recent studies have shown that integrating biological components with nanomaterials can revolutionize the field of pharmacology and help to tackle diseases at a molecular level. In this thesis, different surface modification strategies have been developed. An effort was put mainly on the surface modification of nanodiamonds (NDs), gold NPs (Au-NPs), Au-Pd bimetallic nanocomposites, graphene. These particles were investigated for their possibility to inhibit Gram-positive (*Staphylococcus aureus*) and Gram-negative (*Escherichia coli*) bacteria and destruct of human glioblastoma astrocytoma (U87MG).

After a general overview on nanoparticles for biological applications (Chapter 1), a brief description of nanoparticles, their synthesis, modification and perspectives in nanomedicine. Chapter 2 outlines the synthesis and characterizations of the azido-modified nanodiamonds and their ability of photochemical reaction with sugars. We described the affinity of glycans-modified NDs toward lectins and *Echerichia coli*. In Chapter 3, we elucidate the effect of menthol modified nanodiamond particles (ND-menthol) on bacterial viability against Gram-positive (*Staphylococcus aureus*) and Gram-negative (*Escherichia coli*) bacteria. We show that while ND-menthol particles are non-toxic to both pathogens, they show significant antibiofilm activity

We described the development of novel nanostructures for photodynamic therapy comprising silica-encased gold nanorods modified with verteporfin as photosensitizer and the efficiency of these nanostructures for killing of pathogens in Chapter 4. From another site gold nanorods are known for their efficient conversion of photon energy into heat, resulting in hyperthermia and suppression of tumor growth *in vitro* and *in vivo*. Au NRs are thus of great promise for photothermal therapy (PTT) of different cancers. In Chapter 5 we investigate the potential of polyethylene glycol functionalized reduced graphene oxide (rGO-PEG) enrobed Au NRs for the

photothermal destruction of human glioblastoma astrocytoma (U87MG) cells in mice. Based on these results we showed in Chapter 6 a simple and green solution phase synthetic approach for the formation of bimetallic AuPd NPs on rGO nanosheets for photothermal therapy. Chapter 7 summarizes the results and gives some perspectives of the work.

# CHAPTER I

## Nanoparticles for biological applications

### 1.1. Introduction

Nanoparticles, widely used over more than 35 years now, have made important contributions to a variety of different domains, including the biomedical field. The nanometric size of nanoparticles change the physico-chemical properties when compared to the bulk substantially, thus opening new possibilities in nanomedicine. The use of nanomaterials in medicine has several advantages. Nanomaterials have the characteristics of high surface-to-volume ratios enabling packaging multiple agents onto the same nanoparticles. Using these nanomaterials it might be possible to overcome problems associated with the use of high doses of drugs. Moreover, this type of approach provides also the possibility of targeting specific biological sites actively or passively. Because of their unique features such as nanometric size and controllable hydrophobicity/lipophilicity, such nanocarriers can target drugs to specific tissues or organs, while modification of nanocarrier surfaces enables them to reach particular therapeutics with the results of minimizing side effects onto healthy cells and tissue. With respect to intravenous administration, due to their small size, nanoparticles can circulate in the bloodstream without being retained by the pulmonary capillaries or up taken by the reticuloendothelial system (RES). Indeed, the most frequently used approach to increase the longevity of nanocarriers to avoid the RES uptake is to modify their surface with hydrophilic polymers such as polyethylene glycol (PEG) units.

Various nanocarriers have been proposed over the years and some of the most currently considered are listed in **Figure 1.1**. Next to dendrimers, liposomes and polymeric nanostructures (**Figure 1.1A**), inorganic nanoparticles (**Figure 1.1B**) such as gold, silver, iron oxide, etc have found their application in nanomedicine (2, 3). In this work, we focused on the use of gold nanoparticles (GNPs) as well as nanodiamonds (NDS) and the interest in these nanostructures will be outlined below.

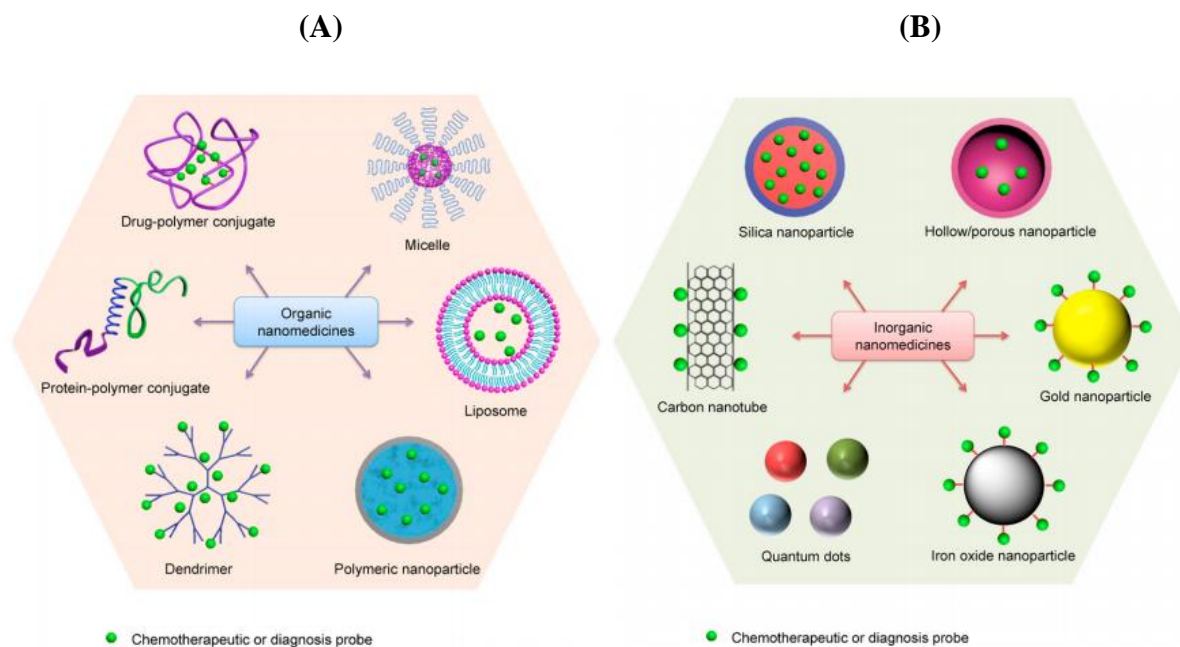


**Figure 1.1:** Classification of nanomaterials that are commonly used as nanomedicine. Some examples of widely used organic (A) and inorganic nanomedicines (B) (1).

## 1.2. Gold nanoparticles (GNPs)

### 1.2.1. Introduction

Gold has been among the first metals, which were discovered by people, and the history of its research and use is at least several thousand years old approximately. The first mention about colloid gold is able to be discovered in tracts by Indian, Chinese and Arabic researchers, who got colloid gold as long ago as in the fourth and fifth centuries B.C. and used it, particularly, in medical purposes (the Indian “liquid gold” and the Chinese “golden solution”). In the European Middle Ages, colloid gold was researched and used in laboratories of alchemists. Namely, Paracelsus informed about the medicinal features of *quinta essentia auri*, which he had got by mixing auric chloride with oil plant extracts or alcohol. He employed “potable gold” in order to heal syphilis and certain mental disorders. Also, Paracelsus stated that chemistry is for producing

drugs, but not for getting gold out of metals. Another researcher of his age, Giovanni Andrea used aurum potable for the treatment of ulcer, leprosy, diarrhea and epilepsy. In 1583, David de Planis-Campy, who was a surgeon of Louis XIII, the King of France, recommended an “elixir of longevity”, which was an aqueous colloid gold solution, as a tool of prolongation of life. The first book on colloid gold, which has preserved to these days, was published in 1618 by doctor of medicine and philosopher Francisco Antonii (4). It includes data on the preparation of colloid gold and its healing applications. This book also includes practical suggestions.

In 1880, in order to treat alcoholism through intravenous injection of colloid gold solution, a way was brought forward (5). This method was called “golden cure”. In 1927, the application of colloid gold was offered in order to alleviate the suffering of inoperable patients with cancer (6). Since the first half of the 20th century, colloid gold in color reactions to blood-serum and spinal-fluid proteins has been taken advantage of (7). Colloid solutions of the Au golden isotope (half-life time, 65 h) were medically successful at oncological institutions (8). More recent cases of using of colloid gold contain transport of substances into cells by endocytosis, catalytic processes and electron transport in biomacromolecules, improvement of PCR effectiveness and researching of cell motility.

In spite of the centuries-long history, a “immuno-chemical revolution”, which was associated with the application of golden particles in biological studies, occurred in 1971 (9). That year, two British scientists, G. M. Taylor and W. P. Faulk, issued the article, which was named “An immunocolloid method for the electron microscope.” This article described technology of conjugating antibodies with colloid gold for immediate electron microscope view of Salmonella surface antigens, which was presenting for the first time when colloid gold conjugation served as an immunochemical marker (10). After this, the application of colloid-gold bio-specific conjugates in different biological and medical areas has become very frequent. There is a lot of information, which relates to the use of functionalized golden nanoparticles (GNPs; conjugates with recognizing biomacromolecules, for example, antibodies, aptamers, enzymes or lectins) (11) in the researches of morphologists, microbiologists, biochemists, cytologists, immunologists, physiologists, and other specialists.

The scope of applications of GNPs in modern biological and medical studies is very large, ranging from biosensorics, optical bio-imaging, targeted delivery of medicines to the photothermolysis of cancer cells and microorganisms (**Figure 1.2**).

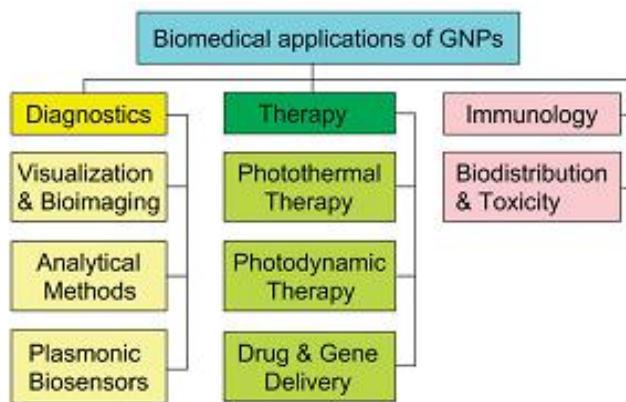


**Figure 1.2:** Generalized scheme for the biomedical application of GNPs. Along with basic applications in diagnostics and therapy, this review briefly discusses the immunological properties of GNPs (12).

This large scope of application is founded on the unique chemical and physical features of GNPs. The exceptional optical properties of GNSs, including large optical field enhancements and their addressability via spectroscopic techniques have made them of particular interest as labels and for biosensing. The optical properties are dominated by the excitation of collective oscillations of the nanoparticles' conduction band electrons, called localized surface plasmon resonances (LSPR), by the incoming electromagnetic waves. At the LSPR, the incoming light is absorbed or scattered by the GNSs, and concurrently, there is an electromagnetic field enhancement close to the surface of the particle. The position of the plasmonic resonance depends on the particle size, shape, composition, interparticle distance as well as the dielectric environment.

However, the use of as-synthesized Au NPs (**Figure 1.3**) in biological systems is limited due by the particle instability and nonspecific binding. These limitations are even increasingly pronounced in high ionic strength media, such as those used for biological assays. The particle aggregation depends strongly on the type of ligand used to passivate the nanoparticles' surface.

The ligands can be displaced or even cross-linked due to the multitude of ionic species present in solution. Care has, in addition, to be paid to the biocompatibility of the particle ligand. For instance, cetyltrimethylammonium bromide (CTAB) modified gold nanorods can be routinely prepared and display good colloidal dispersibility and stability. However, one of the major concerns is related to the cytotoxicity of the surfactant, CTAB, used to stabilize the particles. CTAB molecules can induce cytotoxicity by disrupting cellular membranes CTAB is not only toxic to cells, but also very difficult to remove completely.

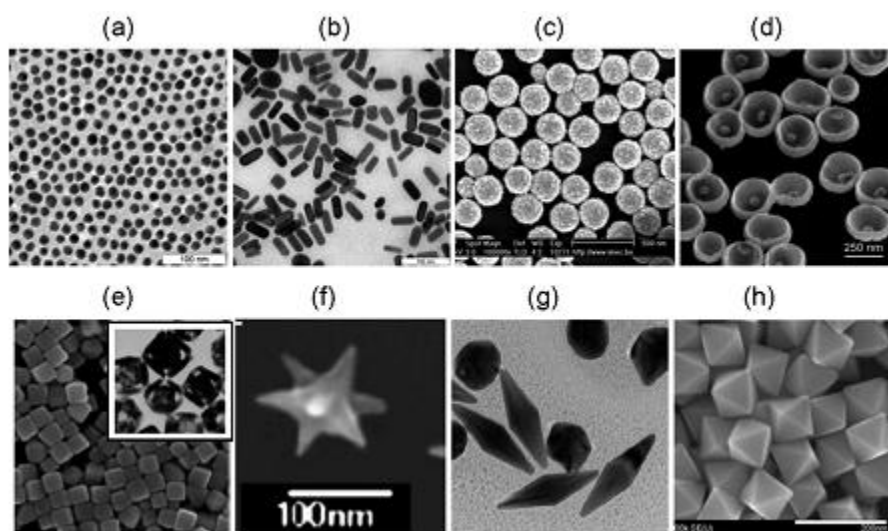


**Figure 1.3:** TEM images of 15-nm nanospheres (a), 15 50-nm GNRs (b), 160(core)/17(shell)-nm silica/gold nanoshells (c, SEM), 250-nm Au nanobowls with 55-nm Au seed inside (d), silver cubes and gold nanocages (inset) (e), nanostars (f), bipyramids (g), and octahedrals (h) (12).

### 1.2.2. GNPs based photothermal therapy (PTT)

While the high surface area is primordial for efficient drug and gene loading, the possible strong optical absorption in the near infrared light (NIR) region makes gold nanocomposites suitable for photothermal therapy (PTT). The first report of GNPs used it in photothermal therapy (13) of cancer calls. Indeed, local heating of cancer cells, known as hyperthermia (warming to 41°–47° C for 1 h) leads to unalterable damage to the cells, caused by destruction of cell membrane permeability and denaturation of proteins. In the case of GNPs based PTT, the generation of heat

is based on laser irradiation of the tumor cells. Pitsillides et al. (14) described in this sense a new technology for selective injuring of target cells, which is based on the using of 20 and 30 nm gold nanospheres that irradiated with 20 ns laser radiation (532 nm) in order to create local heating. **Figure 1.4** displays the example of successful treating of an implanted tumor in mice (15). One of the current modalities for PTT is the use of NIR light absorbing agents. The use of NIR has the advantage that water, melanin and hemoglobin have absorption minima in this region and light between 700-900 nm is most likely to pass directly through tissues without significant absorption and heat generation. (16) GNP nanomaterials exhibit strong visible to NIR absorption owing to the localized surface plasmon resonance effects, rendering them the most power agents for PTT cancer treatment and bacteria killing.

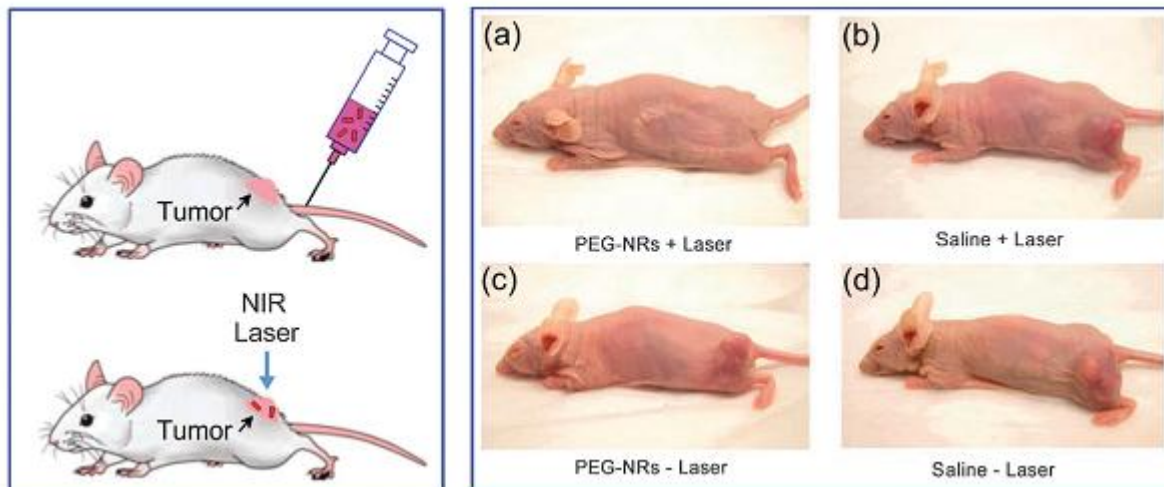


**Figure 1.4:** Scheme and the results of an experiment on the photothermal destruction of an implanted tumor in a mouse (2–3 weeks after injection of MDA-MB-435 human cancer cells). Laser irradiation (a, b; 810 nm,  $2 \text{ W cm}^{-2}$ , 5 min) was performed at 72 h after injection of gold nanorods functionalized with poly(ethylene glycol) (PEG) (a, c; 20 mg Au per kg) or of buffer (b, d). It can be seen that the tumor continued developing after particle-free irradiation (control b), as it did after particle or buffer administration without irradiation (controls c and d), and that complete destruction was obtained only in the experiment (a). Designations: NIR, near-IR region; NRs, nanorods.

The interest of using GNPs is also linked to the possibility of targeted therapy, which has two significant aspects: increasing of the particle concentration in the target and decreasing of side effects, which are caused by GNPs gathering in other parts of a body, mainly in the spleen and liver). *In vivo*, PEGylated nanoparticles primarily gather in tumor tissue, thanks to the enhanced permeability of the vessel of tumor and are held in it thanks to the reduced lymph outflow (17). Moreover, PEGylated nanoparticles are less available to the immune system (stealth methods). This delivery technology is named passive, unlike the active variant, which applies antibodies (**Figure 1.5**). The active technology of delivery is more relevant and efficient, using antibodies to certain tumor markers, most often to receptor of epidermal growth factor (EGFR) and its variations (for example, Her2) (18), and to tumor necrosis factor (TNF) (19). Certain prospects are offered by the synchronous using of GNP–antibody conjugates for PPTT and diagnosis (this technology is called theranostics). Besides antibodies, active delivery can as well apply folic acid, which acts as a ligand for the many folate receptors of hormones and tumor cells (20).

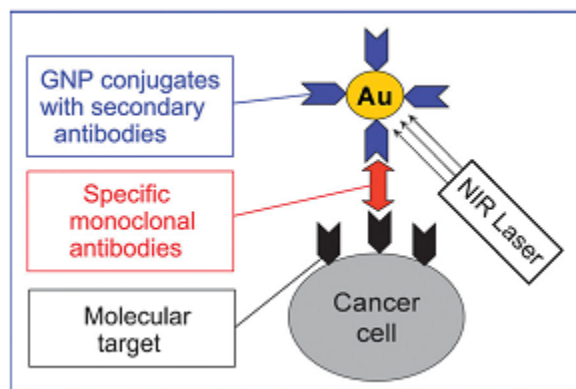


**Figure 1.5:** Scheme for a PPTT employing active delivery of GNPs to cancer cells (21).

### 1.2.3 Photodynamic treating with GNPs

The photodynamic way of treating of certain skin or infectious diseases and oncological diseases is based on the using of light-sensitizing substances, which are called photosensitizers (including dyes) and, commonly, of visible lights at a specific wavelengths (21). As a rule, sensitizers are injected intravenously, but oral and contact using is also possible. The agents, which are used in

photodynamic treating (PDT) are able to selectively gather in tumors or other target objects (cells). The infected tissues are irradiated by laser light at a wavelenths, which corresponds to the maximum of dye absorption (21). At the same time, besides the usual warm emission by absorption, a significant role is played by another mechanism, which is associated with the photochemical generation of singlet oxygen (**Figure 1.6.**) and the forming of highly active radicals, which bring apoptosis and necrosis in tumor cells.

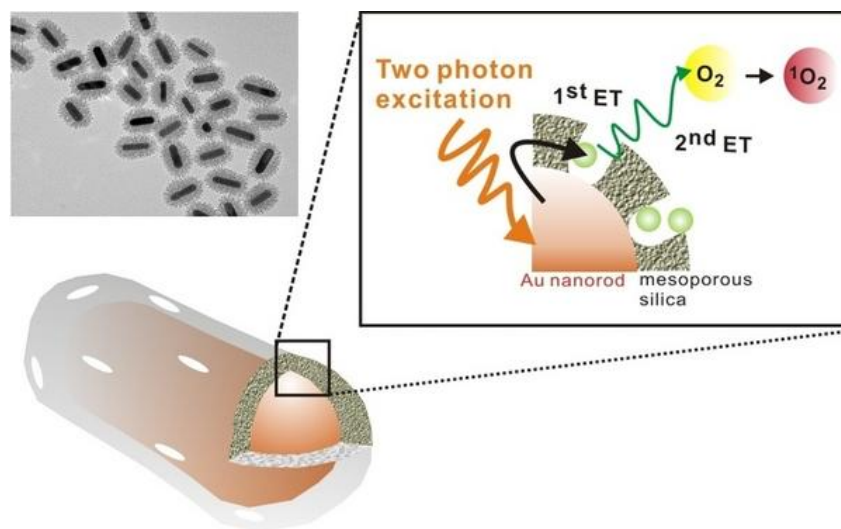


**Figure 1.6:** two-photon-activated photodynamic therapy (TPA-PDT) using mesoporous silica-encased gold nanorods (21).

PDT also undermined the tumor nutrition and brings to its death by injuring its micro-vessels. The main PDT shortcoming is that the photosensitizer stays for a long time in the organism, leaving tissues of a patient highly sensitive to light. Although, the efficiency of dye application for selective tissue warming is low because of the little cross section of chromophore absorption (21).

### 1.3. Nanodiamonds

The first record of the production of ND particles dates back to the 1960s, when a group of Soviet scientists discovered single crystals of cubic diamond particles in soot produced by detonating an

oxygen-deficient TNT/hexogen composition in inert media without using any extra carbon source (22) (**Figure 1.7.**)

This man-made diamond did not attract much attention at the beginning due to a continued failure in disintegrating ND particles into primary particles (23). While the particle size of its primary crystallites is ~5 nm with a very narrow size distribution (23, 24), due to harsh conditions in the reaction chamber, detonated ND particles exist mainly in the form of strongly bound agglomerates. The particles are not only linked by the usual electrostatic interactions by also *via* covalent bonds between surface functional groups as well as by soot structures surrounding each primary particle (25, 26).

The detonation soot can be purified using oxidizing mineral acids (HNO<sub>3</sub>, mixtures of H<sub>2</sub>SO<sub>4</sub> and HNO<sub>3</sub>, K<sub>2</sub>Cr<sub>2</sub>O<sub>7</sub> in H<sub>2</sub>SO<sub>4</sub>, KOH/KNO<sub>3</sub>, HNO<sub>3</sub>/H<sub>2</sub>O<sub>2</sub> under pressure, etc) (27), as the reactivity of disordered sp<sup>2</sup> carbon is higher than that of diamond, thus removing non-diamond impurities. During the cleaning step, the surface of NDs is covered with a variety of functional groups such as hydroxyl, carbonyl, carboxyl, anhydride and lactone moieties.

These purified ND particles show still a strong tendency to agglomerate, which can withstand ultrasonic treatment. To overcome this limitation, de-aggregation process in suspension by milling detonated NDs with ceramic microbeads (ZrO<sub>2</sub>, SiO<sub>2</sub>) or by microbead-assisted ultrasonic disintegration can be applied to NDs (28-30), leading to stable colloidal solutions of individual ND particles of 4-5 nm in diameter. However, contamination of NDs with difficult-to-remove zirconia, the high cost of zirconia microbeads, and NDs amorphization (or even graphitization) in the course of milling are major drawbacks of the microbeads-assisted milling. Retreatment of the de-agglomerated particles with oxidizing chemicals is therefore needed, which results in a partial re-aggregation of the primary particles. Other attempts have been undertaken to limit the NDs' agglomeration. ND aggregates disintegration using mechano-chemical treatment, that is, milling in the presence of chemicals such as surfactants and electrolytes (e.g., sodium oleate) was investigated (31, 32). Mechanical action was applied in the form of grinding or sonication in the

presence of sodium oleate and resulted in a reduction of the aggregate size of the treated ND in water from 2  $\mu\text{m}$  down to 40-60 nm. However, no particles smaller than 20 nm were observed. More recently, dry salt- or sucrose-assisted milling was successfully used as simple, inexpensive, and efficient alternative method for the disaggregation of NDs (33). The technique uses non toxic and non-contaminating compounds such as sodium chloride and sucrose, which can be easily removed at the end of the milling process. By using the dry media assisted milling with subsequent pH adjustment, it is possible to produce stable aqueous NDs colloidal solutions with particles <10 nm in diameter.

High-temperature hydrogen treatment resulted, moreover, in stable single particle aqueous NDs suspension of 4-5 nm (34). Independent of the method chosen, one concern that needs to be addressed in any case is the possibility of re-aggregation over time, during drying and/or after surface functionalization due to capillary forces or attractive van der Waals forces, pulling the particles together.

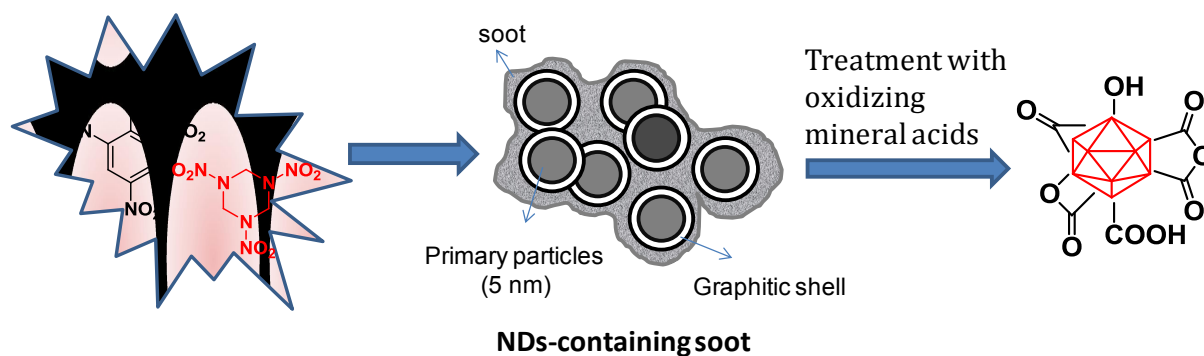


**Figure 1.7:** Formation of detonation NDs with well-defined surface termination: A mixture of TNT (60 wt%) and hexogen (40 wt %) is detonated in a closed metallic chamber in an atmosphere of  $\text{N}_2$ ,  $\text{CO}_2$  and liquid or solid water forming a diamond-containing soot. The soot is purified with oxidizing mineral acids to produce oxidized NDs (23, 27, 35).

Independent on their treatment, such detonation ND particles have been rapidly gaining popularity for biological applications. This is related to the presence of various functional groups

enabling quite complicated surface functionalizations without compromising of the helpful features of the diamond center Reactive C–Cl and C–F surface species, which are created by halogen hardening and photochemical chlorination have been applied in many wet chemical reactions (36). Nanodiamond with O–H terminations was used in esterification with acetyl chlorides, which then were terminated by long alkyl chain (37), and in silanization/de-aggregation (38). Other reactions were also applied (39, 40). They include those ones, which are especially convenient for biomedical using (41). Diazonium chemistry was also employed with hydrogenated nanodiamond (42) in order to form C–C bindings between the adhered part and diamond center, and with hydroxylated nanodiamond (38) in order to form C–O–C bindings. Therefore, nanodiamond gives many variants for surface functionalization, but the result sharply depends on the clearing and uniformity of the surface chemistry of the starting substance. As already noted, functionalization also impacts the stability of diamond surfaces. One task in the area is to discover methods for quantitative analysis of different surface groups of nanodiamond. By now, most of the data are qualitative.

Thanks to the various clearing procedures, which are used by different producers, and the multiple variants for surface change, the toxicity of nanodiamonds is of legitimate doubt (43). *In vivo* and *in vitro* studies have been carried out in order to examine features as diverse as cell vitality, activity of gene program, and *in vivo* physiological and mechanistic behavior (43, 44). Nanodiamonds, which are instilled onto trachea, were noted to be of low pulmonary toxicity, with the number of nanodiamonds in the alveolar area reducing with time, and macrophages bore by nanodiamonds were monitored in the bronchia for 28 days after subjecting (45). Intravenously delivered nanodiamond complexes in high dosages did not modify serum indicators of systemic and liver (46).

In order to assess the fate of nanodiamonds and their influence on stress response activities and worm reproduction, nanodiamond aggregates with average size of ~120 nm were fed and microinjected in the semitransparent *Caenorhabditis elegans* worm, and then monitored for some days (47). Bald nanodiamonds usually stayed in the worm lumen, where nanodiamonds were covered with bovine or dextran serum albumin (BSA), were absorbed by intestinal cells.

Nanodiamonds, which were injected into worm gonads, were moved into the larvae and offspring, but this had no influence on the reproductive abilities or survival of these worms. Subsequent experiments, which involved DAF-16:GFP (DAF-16 is a group of genes that controls the stress and immune cell responses; GFP is green fluorescent protein), proved that fluorescent nanodiamond is not toxic and does not bring stress in the worm model, therefore ensuring support for its application in *in vivo* imaging. However, given the number of surface modifications, which are probable, it is essential to be certain that the functionalized nanodiamonds, which are intended for biomedical applications, stay safe. Thus, we have lately compared the cytotoxicity and osteoblast proliferation and gene expression impacts of octadecylamine modified nanodiamond (ND-ODA), carboxylated nanodiamond, and compounds of poly(L-lactic acid) with ND-ODA (48). Despite no harmful impacts were found in these materials, toxicity and biocompatibility testing of new nanodiamond-based materials must be continued.

**In this thesis we took advantage of the interesting surface properties of gold nanorods and diamond nanoparticle and investigated their use for biomedical applications.** In particular the design and development of new antibacterial treatments could be based on novel nanoparticles. We will show in more details the use of particles for the treatment of uropathogenic *E. coli*. Complications related to infectious diseases have significantly reduced, particularly in the developed countries, due to the availability and use of a wide variety of antibiotics and antimicrobial agents. However, excessive use of antibiotics and antimicrobial agents increased the number of drug resistant pathogens, and this has resulted in a significant threat to public health. The inexorable rise in the incidence of antibiotic resistance in bacterial pathogens, coupled with the low rate of emergence of new clinically useful antibiotics, has refocused attention on finding alternatives to overcome antimicrobial resistance. Among the various approaches, the use of engineered nanoparticles is currently the most promising strategy to overcome microbial drug resistance by improving the remedial efficiency due to their high surface-to-volume ratio and their intrinsic or chemically incorporated antibacterial activity. We show in this thesis that diamond nanoparticles (NDs) as well as gold nanorods are revealing themselves to have great promise as useful materials for combating microbial infections, in particular

## 1.4. References

1. Tang L, Cheng J. Nonporous silica nanoparticles for nanomedicine application. *Nano today*. 2013 ;8(3):290-312.
2. Jana NR, Chen Y, Peng X. Size-and shape-controlled magnetic (Cr, Mn, Fe, Co, Ni) oxide nanocrystals via a simple and general approach. *Chemistry of materials*. 2004; 16(20):3931-5.
3. Kass DA, Champion HC, Beavo JA. Phosphodiesterase type 5 expanding roles in cardiovascular regulation. *Circulation research*. 2007;101(11):1084-95.
4. Antonii F. *Panacea aurea-auro potabile*. Hamburg: Ex Bibliopolio Frobeniano.1618:250.
5. Keeley LE. The So-Called Gold Treatment of Inebriety. *British medical journal*. 1892; 2(1647):182.
6. Ocshner D. The use of colloidal gold in inoperable cancer. *J Med & Surg*. 1927.
7. Green F. The colloidal gold reaction of the cerebrospinal fluid. *Canadian Medical Association journal*. 1925; 15(11):1139.
8. Rogoff EE, Romano R, Hahn EW. The Prevention of Ehrlich Ascites Tumor Using Intraperitoneal Colloidal 198Au: Dose vs. Size of Inoculum 1. *Radiology*. 1975; 114(1):225-6.
9. Beesley J, editor *Colloidal gold: a new revolution in marking cytochemistry*. Proc R Microsc Soc; 1985.
10. Faulk WP, Taylor GM. Communication to the editors: an immunocolloid method for the electron microscope. *Immunochemistry*. 1971; 8(11):1081-3.
11. Hermanson G. *Bioconjugate Techniques* Academic Press, san Diego. CA; 1996.
12. Khlebtsov NG, Dykman LA. Optical properties and biomedical applications of plasmonic nanoparticles. *Journal of Quantitative Spectroscopy and Radiative Transfer*. 2010; 111(1):1-35.
13. Hirsch LR, Stafford R, Bankson J, Sershen S, Rivera B, Price R, et al. Nanoshell-mediated near-infrared thermal therapy of tumors under magnetic resonance guidance. *Proceedings of the National Academy of Sciences*. 2003;100(23):13549-54.
14. Pitsillides CM, Joe EK, Wei X, Anderson RR, Lin CP. Selective cell targeting with light-absorbing microparticles and nanoparticles. *Biophysical journal*. 2003; 84(6):4023-32.

15. von Maltzahn G, Park J-H, Agrawal A, Bandaru NK, Das SK, Sailor MJ, et al. Computationally guided photothermal tumor therapy using long-circulating gold nanorod antennas. *Cancer research*. 2009; 69(9):3892-900.
16. Weissleder RA. A clearer vision for in vivo imaging. *Nat Biotechnol*. 2001; 19(4):316.
17. Jain RK, Booth MF. What brings pericytes to tumor vessels? *The Journal of clinical investigation*. 2003; 112(8):1134-6.
18. Loo C, Lowery A, Halas N, West J, Drezek R. Immunotargeted nanoshells for integrated cancer imaging and therapy. *Nano letters*. 2005; 5(4):709-11.
19. Visaria RK, Griffin RJ, Williams BW, Ebbini ES, Paciotti GF, Song CW, et al. Enhancement of tumor thermal therapy using gold nanoparticle–assisted tumor necrosis factor- $\alpha$  delivery. *Molecular cancer therapeutics*. 2006; 5(4):1014-20.
20. Lu W, Xiong C, Zhang G, Huang Q, Zhang R, Zhang JZ, et al. Targeted photothermal ablation of murine melanomas with melanocyte-stimulating hormone analog–conjugated hollow gold nanospheres. *Clinical cancer research*. 2009; 15(3):876-86.
21. Wilson R. The use of gold nanoparticles in diagnostics and detection. *Chemical Society Reviews*. 2008; 37(9):2028-45.
22. Danilenko VV. *Phys Solid State*. 2004; 46:595.
23. Krüger A, Katoako F, Ozawa M, Fujino T, Suzuki Y, Aleksesnii AE, et al. *Carbon*. 2005; 43:1722.
24. Shenderova OA, Zhirnov VV, Brenner DW. *Crit Rev Sol State Mater Sci*. 2007; 27:38.
25. Krüger A, Ozawa M, Jarre G, Liand Y, Stegk J, Lu L. *Phys Stat Sol (a)* 2007;204:2881.
26. Osswald S, Yushin G, Mochalin V, Kucheyev SO, Gogotski Y. *J Am Chem Soc*. 2006; 128:11635.
27. Ushizawa K, Sato Y, Mitsumori T, Machinami T, Ueda T, Ando T. *Chem Phys Lett*. 2002; 351:105.
28. Ozawa E. *Diamond Rel Mater*. 2007; 16:2018.
29. Ozawa E. Single-nano buckydiamond particles: Synthesis strategies, characterization methodologies and emerging applications. Ho D, editor. New York: Springer; 2010. 1-33 p.

30. Ozawa M, Inaguma M, Takahashi M, Kataoka F, Krüger A, Ōsawa E. Preparation and Behavior of Brownish, Clear Nanodiamond Colloids. *Adv Mater.* 2007; 19:1201-6.
31. Xu X, Yu Z, Zhu Y, Wang B. Effect of sodium oleate adsorption on the colloidal stability and zeta potential of detonation synthesized diamond particles in aqueous solutions *Diamond Relat Mater.* 2005; 14:206-12.
32. Xu X, Zhu Y, Wang B, Yu Z, Xie S. Mechanochemical dispersion of nanodiamond aggregates in aqueous media. *J Mater Sci Technol.* 2005; 21:109.
33. Pentecost A, Gour S, Mochalin V, Knoke I, Gogotsi Y. *ACS Appl Mater Interfaces.* 2010; 2:3289.
34. Williams OA, Hees J, Dieker C, Jager W, Kirste L, Nebel CE. Size-dependent reactivity of diamond nanoparticles. *ACSNano.* 2010; 4:4824-30.
35. Krüger A. New Carbon Materials: Biological Applications of Functionalized Nanodiamond Materials. *Chem-Eur J.* 2008;14:1382-90.
36. Liu Y, Gu Z, Margrave JL, Khabashesku VN. Functionalization of nanoscale diamond powder: fluoro-, alkyl-, amino-, and amino acid-nanodiamond derivatives. *Chemistry of materials.* 2004;16(20):3924-30.
37. Krueger A, Boedeker T. Deagglomeration and functionalisation of detonation nanodiamond with long alkyl chains. *Diamond and related materials.* 2008; 17(7):1367-70.
38. Liang Y, Ozawa M, Krueger A. A general procedure to functionalize agglomerating nanoparticles demonstrated on nanodiamond. *ACS nano.* 2009; 3(8):2288-96.
39. Krueger A. Diamond nanoparticles: jewels for chemistry and physics. *Advanced Materials.* 2008; 20(12):2445-9.
40. Krueger A. The structure and reactivity of nanoscale diamond. *Journal of Materials Chemistry.* 2008; 18(13):1485-92.
41. Krueger A, Stegk J, Liang Y, Lu L, Jarre G. Biotinylated nanodiamond: simple and efficient functionalization of detonation diamond. *Langmuir.* 2008; 24(8):4200-4.
42. Yeap WS, Chen S, Loh KP. Detonation nanodiamond: an organic platform for the suzuki coupling of organic molecules. *Langmuir.* 2008; 25(1):185-91.

43. Schrand A, Johnson J, Dai L, Hussain S, Schlager J, Zhu L, et al. Safety of Nanoparticles. *Nanostructure Science and Technology* Springer. 2009:159-87.
44. Schrand AM, Huang H, Carlson C, Schlager JJ, Osawa E, Hussain SM, et al. Are diamond nanoparticles cytotoxic? *The journal of physical chemistry B*. 2007; 111(1):2-7.
45. Yuan Y, Wang X, Jia G, Liu J-H, Wang T, Gu Y, et al. Pulmonary toxicity and translocation of nanodiamonds in mice. *Diamond and Related Materials*. 2010; 19(4):291-9.
46. Chow EK, Zhang X-Q, Chen M, Lam R, Robinson E, Huang H, et al. Nanodiamond therapeutic delivery agents mediate enhanced chemoresistant tumor treatment. *Science translational medicine*. 2011; 3(73):73ra21-73ra21.
47. Mohan N, Chen C-S, Hsieh H-H, Wu Y-C, Chang H-C. *In vivo* imaging and toxicity assessments of fluorescent nanodiamonds in *Caenorhabditis elegans*. *Nano letters*. 2010;10(9):3692-9.
48. Zhang J, Su DS, Blume R, Schlögl R, Wang R, Yang X, et al. Surface Chemistry and Catalytic Reactivity of a Nanodiamond in the Steam-Free Dehydrogenation of Ethylbenzene. *Angewandte Chemie International Edition*. 2010; 49(46):8640-4.

## CHAPTER II

### **Affinity of Glycans-Modified Nanodiamonds towards Lectins and Uropathogenic *Escherichia Coli***

#### **2.1. Introduction**

Gram-negative bacteria are usually responsible for the majority of the urinary infections and Uropathogenic E.coli (UPEC) is one of them and may cause up to 90% of the infections of the urinary tract. Despite of the presence of different defense mechanisms, such as cytokine triggered recruitment of neutrophils that is followed by the superficial infected tissue exfoliation, production of specific antimicrobial factors, bacteria may remain unaffected even with the constant presence of the antibiotic treatment. Basing on that, new methods of treatment of the diseases that are caused by these bacteria need to be created (1).

One of the most efficient practices in terms of the treatment was considered the usage of nanoparticles (NP) since it allows sensing the presence of microbes and in addition to it, requires less costs for equipment and consumes less time. A protocol that is based on functionalized gold NPs (Au-NPs) and carries quaternary ammonium salts was developed by Rotello and colleagues, and it allows to trigger the detection, based on enzyme-enhanced pathogen. Other Au-NPs reports also are capable of detection of bacteria, viruses and proteins. Besides that, Au-NPs may be used for the detection of other elements such as gadolinium sulfide, silver, iron oxides and nanomaterials of carbons that also may be used for the detection of the bacteria that are considered to be pathogenic (2).

Nevertheless, it should be noted that most of the current methods are based on the electrostatic interactions of the NPs that respond to the viruses, proteins and microbes that are detected (3).

This interaction is characterized by non-selectiveness and it means that the process of selectivity cannot be applied to specific type of bacteria. Selectivity problem can be resolved in terms of the conjugation with specific molecules that should be able to remove bacteria on a NP-based platform. Since the majority of bacteria show specificity to certain types of saccharides, carbohydrates can be useful for the indicated aim. That is why it is necessary to design specific nanoparticles that are capable of the selective detection of the specific saccharide motifs and will be able to remove various bacterial strains.

With the usage of the indicated approach, several aspects need to be fulfilled: availability should be broad, surface functionalization should be stable, dispersibility on aqueous solutions should be stable as well, medical and environmental nanoparticles should be benign. The material that is able to maintain indicated requirements is nanoscale diamond (ND). It is available in rather big amounts, it is hydrophilic, can be used (functionalized) in different ways and it is also safe and biocompatible. It has some advantages in comparison with other nanoparticles and objects, for example, carbon nanotubes and polymer NP, since it is an inert particle and will not well in any other solvents, it can be used on labeling applications, can stand high temperatures (it is thermal, up to 4508 C), has very low toxicity and shows stability in terms of mechanics.

Glyco-nanodiamonds (glyco-NDs) are only described in few reports (4-7) . Multistep reaction was presented by Krueger and his colleagues, specifically in Diels–Alder cycloaddition of 1,2-dimethylbromide phenol to the ND surface, followed by a classical aromatic sulfonation and reduction to thiol (5). For allyl-modified glycans in a “thiol-ene” type reaction, thiol-modified NDs were used as anchors and it allowed efficient detection and removal of bacteria that are considered to be pathogenic. Inhibition of bacterial adhesion was presented more recently and it occurs due to the potential stored in thiourea-bridged ND glycoconjugates (6). Glyco-NDs were constructed via the propargyl-terminated sugar components to azide-functionalized NDs conjugation (4), together with azide-terminated sugars to propargyl-terminated NDs conjugation (4, 8). As result, we were able to show that glyco-NDs inhibit type 1 fimbriae-mediated yeast-agglutination bind in a sugar-selective manner with human bladder-cell adherence. Consequently,

indicated inhibitory efficiency of the ND-mannose was higher than other glycan-modified particles and nanostructures directed against *E. coli*.

This passage reports and presents the application and synthesis of a new, saccharide-modified ND material, which is capable of detection of bacteria. The construct itself, which is considered to be synthetic, consists of a nanoscale diamond core (**Figure 2.1a**) and is adjusted with the linker moiety that allows photoinduction of covalent attachment to unmodified sugars (**Figure 2.1b**). Interaction of glycosylated ND is possible with the bacterial cells, for example, fluorescing *E. coli* (**Figure 2.1c, d**), which occurs because of the certain interactions of protein–carbohydrate. It is a typical bacterial function to bind with the carbohydrates that are usually utilized in order to attach to their target cells via glycosylated surface. It can eventually lead to the infection of the entire host organism and also lead to the formation of biofilms.

In order to perform adhesion effectively, the majority of bacteria have hairy protein appendages that are usually named pili or fimbriae. Indicated parts of the bacteria expose protein domains and are also functioning as lectins and are able to mediate interaction of molecules with the certain carbohydrates for which their selectiveness is usually shown. Type 1 fimbriae are organized the best and are able to recognize terminal  $\alpha$ -D-mannoside units with the high specificity in high-mannose type glycoproteins on the host-cell surface. The unit responsible for the mannoside binding, is a lectin domain and is located on the fimbrial tips and is called FimH. Throughout the family of Enterobacteriaceae, Type 1 fimbriae are very common and include highly pathogenic strains of EHEC and UPEC. As a result, we have chosen mannose specificity of the bacterial binding as an object of investigation and research the role of glycosylated ND in removal and detection of the bacteria.

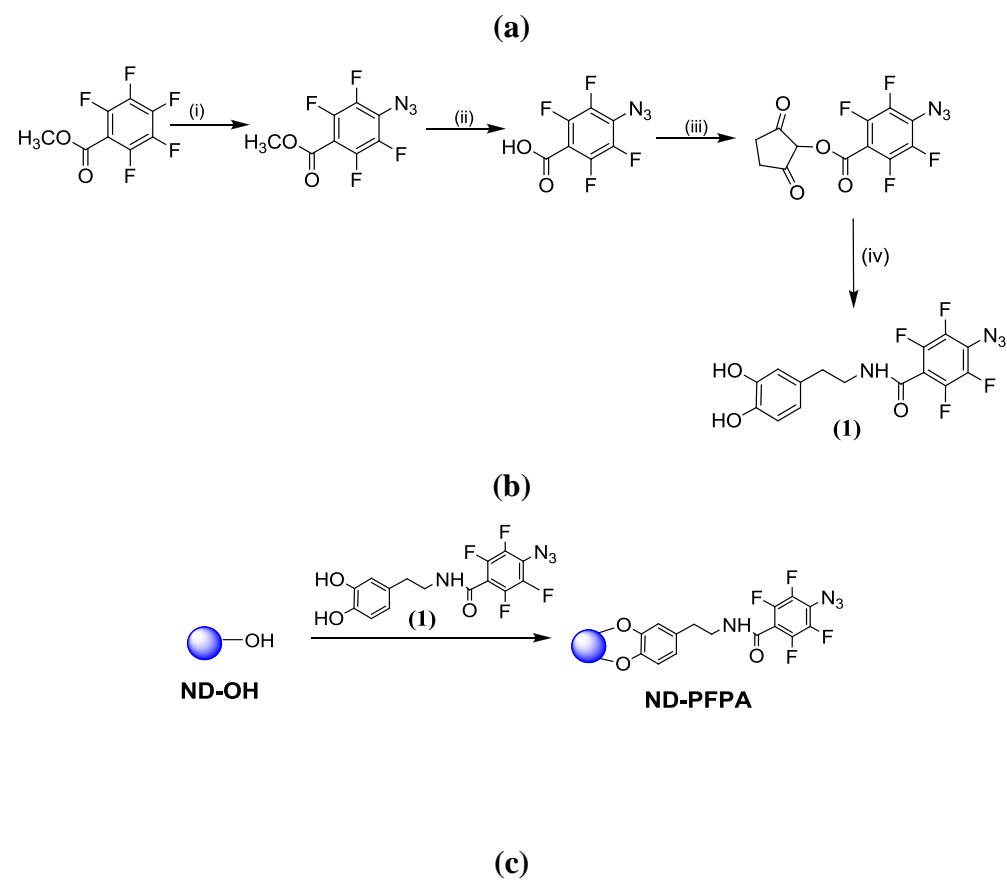
The aim of the work is to create photochemical strategy that will be useful for the formation of different glyco-NDs. In case when created glyco-NDs will maintain their affinities to lectins, cross-selective and binding studies were performed with the usage of fluorescently labeled lectins in order to determine the validity. Indicated study may have one drawback that is presented in the

non-specificity of the coupling reaction, when the glycans to NDs' attachment is not happening with the usage of the reducing ends. We will also show that when monosaccharides such as mannose are linked, binding affinities of glyco-NDs to lectins are partially sacrificed, while it is fully preserved for binding of disaccharides and oligosaccharides. Moreover, it was checked whether glyco-NDs are capable of presenting affinity to uropathogenic *Escherichia coli* strain (*E. coli* UTI89). Type 1 fimbriae have been identified as the main target, which constitute major virulence factors produced by *E. coli* UTI89. Type 1 fimbriae have tubular structure in the size of 0.2-2.0 nm in length and 5-7 nm in diameter and they are located all over the surface of the bacterium. On the extremity of the type 1 fimbriae, lectin is located, FimH, it contributes to the colonization of tissue through the specific recognition of The  $\alpha$ -D-mannopyranosyl terminal units that are located on the glycoproteins surface of the cell. Mannose-modified NDs exhibit anti-adhesive activity for *E. coli* UTI89 that marked and cell-based assays do not display toxicity for the eukaryotic cells (4, 7). Cu<sup>I</sup>-catalyzed Huisgen cycloaddition reaction ("click" reaction) between NDs decorated with surface azidophenyl or propargyl functions and the corresponding synthetic sugar analogue was used as a base for the coupling strategy. Fluorescence-based agglutination assay was used in order to investigate potential of photochemically grafted native mannan and mannose in the interaction with *E. coli* UTI89 (6).

## **2.2. Synthesis of glycol-NDs via photoactication of perfluorophenyl- azide-modified NDs**

We have indicated previously that dopamine is known for having significant interactions with various oxides of metal and structures that are graphene-like and it is an agent that is viable for the nanodiamonds' functionalization (8, 9). Synthesis of a dopamine derivative of perfluorophenylazide (**1**) was performed through the reaction of the *N*-succinimidyl 4-azidotetrafluorobenzoate with the amine groups of dopamine (**Figure 2.1a**). Functionalization of hydroxylated nanodiamonds (ND-OH) was performed via ligand (**1**) (**Figure 2.1b**). ND particles that were functionalized could be characterized with the Fourier transform infrared (FTIR) spectroscopy (**Figure 2.2a**) and X-ray photoelectron spectroscopy (XPS) (**Figure 2.2b**). The spectrum of the FTIR of the as-received ND-OH (**Figure 2.2a**) presents a high measure at 3447

cm<sup>-1</sup> with the reference to the vibration of surface hydroxyl groups or/and adsorbed water molecules, and an additional sharper one at 1633 cm<sup>-1</sup> due to the bending mode d<sub>(OH)</sub> of surface hydroxyl groups on the NDs. In addition, the band at 1107 cm<sup>-1</sup> shows the presence of C-O-C - functional groups of cyclic ethers. After ND-OH particles reacted with ligand **(1)**, another vibration peak at 2125 cm<sup>-1</sup> common for the ν<sub>as(N3)</sub> stretching appears. The C-H stretching vibration modes are detected at 2850–2970 cm<sup>-1</sup> and are partially masked with the large band at 3447 cm<sup>-1</sup>. The band at 1546 cm<sup>-1</sup> must be linked to the NH-C=O bond that is present in ligand **(1)**. The azide group presence on ND-PFPA is additionally confirmed by the N1s high resolution XPS spectrum (**Figure 2.2b**).



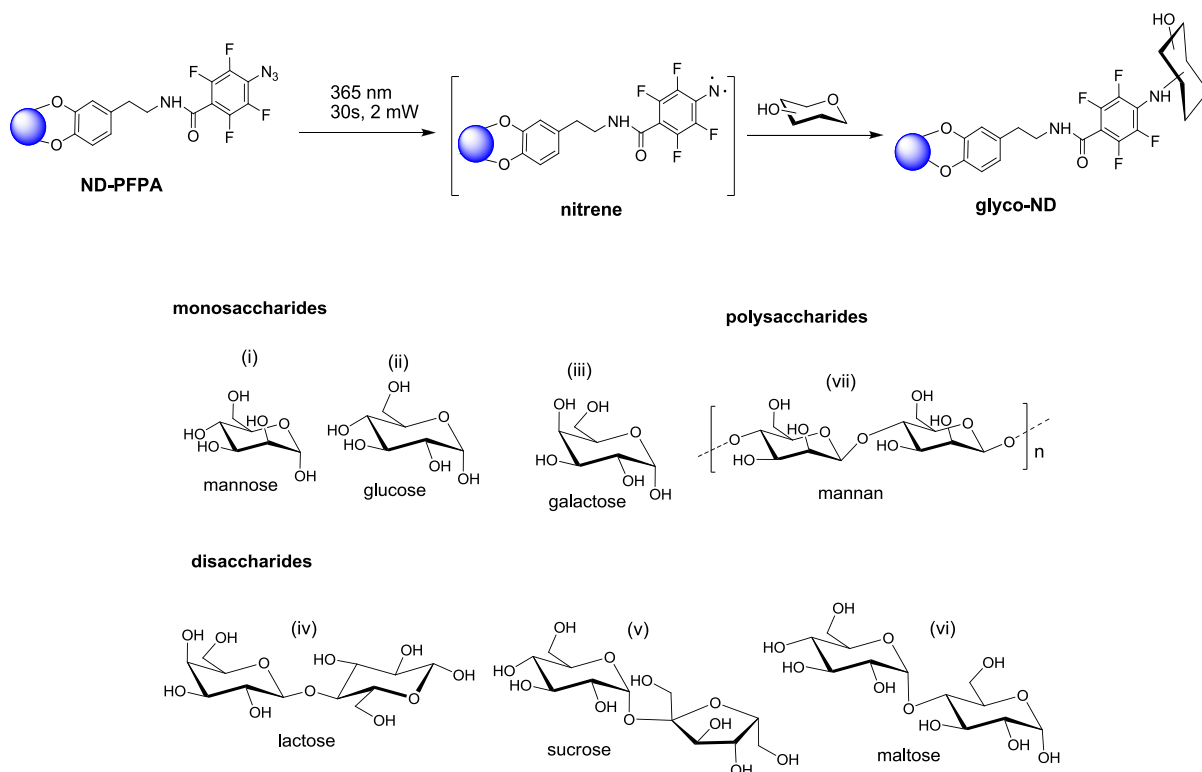


**Figure 2.1:** a) Synthesis of perfluorophenyl azide modified dopamine (**1**): (i)  $\text{NaN}_3$ , acetone/water, 90C, 2h, 85%; (ii) NaOH, water, 3h, RT, 90%, (iii) NHS, DCM, RT, overnight, 95%, (iv) dopamine hydrochloride, TEA, DMF, RT, argon, 91.4%. b) Modification of ND-OH with ligand (**1**) forming NF-PFPA. c) Formation of glycol-NDs through the photochemical linking of mono-, di-, and a polysaccharide onto NDs.

Bands at 405.2 (Ar  $\text{N}=\text{N}^+ = \text{N}$ ) and 401.9 eV (Ar  $\text{N} = \text{N}^+ = \text{N}$ ), characteristic for the N contribution of the NH C=O linkage is seen at 400.6 eV. Bands at 402.7 and 399.2 eV are also present in the initial ND-OH. It most likely corresponds with the nitrogen functions, for instance, N-O and C-N were probably generated during the process of detonation of trinitrotoluene with the NDs' formation. **Table 2.1** presents the results where nitrogen content has 1.5 at % and possible may be in charge of the positive surface potential of ND-OH (**Table 2.1**), which was also reported in different studies. In ND-PFPA particles, the presence of N 1s was increased to 8.4 at % with a F/(N-1.5) ratio of 1.28, which is near the theoretical measure of 1.33. In order to make sure that conjugates are stable and dopamine ligand will not be detached after certain

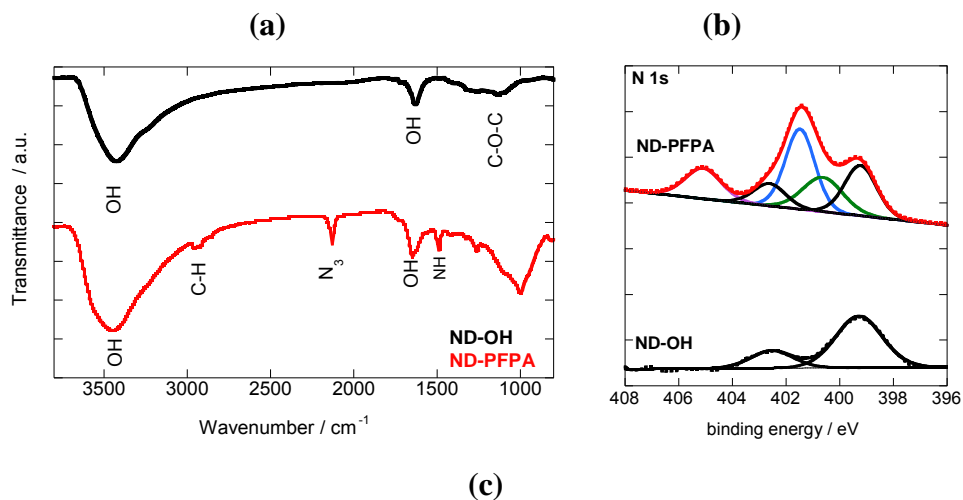
period of time, ND-PFPA particles were immersed for 24 h at various pH (3, 7, and 9) as well as in biological medium such as Dulbecco's modified Eagle medium (DMEM) and the FTIR spectra were recorded.

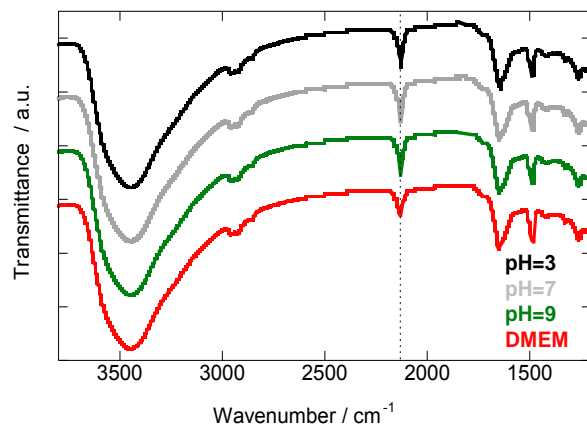
**Table 2.1:** Physical properties of the NDs modified with ligand (1)

Table 2.1 Physical properties of the NDs modified with ligands (1).					
NDs	Diameter [nm]	PI <sup>[a]</sup>	Zeta potential [mV]	N <sup>[b]</sup> [%]	F <sup>[c]</sup> [%]
ND-OH	79 ± 13	0.246 ± 0.002	35 ± 2	1.5	0.0
ND-PFPA	126 ± 3	0.168 ± 0.021	34 ± 2	8.4	6.9

[a] Polydispersity index. [b] Atomic percent according to N 1s XPS spectrum. [c] Atomic percentage according to F 1s XPS spectrum

As it is indicated in the (Figure 2.2c), no strong lowering of the  $\nu_{as}(N_3)$  band at 2125  $\text{cm}^{-1}$  was observed due to immersion into solutions of different pH, and only a slight decrease was observed when incubated in biological medium.





**Figure 2.2:** **a)** FTIR spectra of ND-OH (black) and ND-PFPA (red). **b)** N 1s high-resolution XPS spectra of ND-OH (black) and ND-PFPA (red). **c)** FTIR spectra of ND-PFPA after immersion for 24 h in pH 3, pH 7, pH 9 buffer, and DMEM.

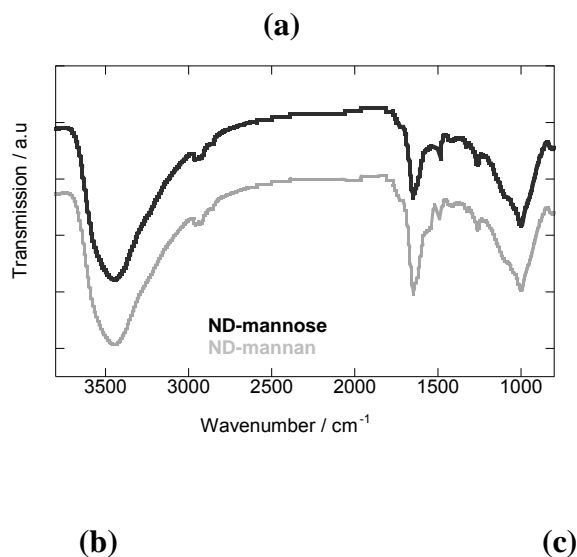
The ether bond between the diamond surface and the aromatic ring of dopamine can be considered as stable in comparison with the organic molecules that take place within the indicated period of time with no hydrolysis. Photochemical linkage of glycans to NDs is better than the photochemistry of arylazides that are converted to the reactive nitrenes because of the light activation (**Figure 2.2c**). Nitrenes that are highly reactive are capable of the direct interaction with any type of glycan due to the C-H and/or N-H reactions of insertion and create highly robust covalent linkage. Mono-, di- and a polysaccharide were photochemically integrated into ND-PFPA particles (**Figure 2.2c**) using the mixture of the solution of ND-PFPA in acetonitrile with aqueous solutions of the respective glycan, and irradiating the mixtures at 365 nm for 30 s at 2 mW.

Representative FTIR spectrum of mannan-modified NDs and mannose are presented in **Figure 2.3 A** and show that characteristic  $N_3$  vibration band at  $2128\text{ cm}^{-1}$  completely disappears, which in its turn suggest consummation of all azido groups in the photochemical process. The band at  $1633\text{ cm}^{-1}$  due to the bending mode  $\delta_{OH}$  increased significantly in the case of ND-mannan.

The N 1s XPS spectra after photochemical linking of mannose also changed significantly. The

conversion of the azide group into C-N bonds is proved by the disappearance of the bands at 405.2 (Ar N=N<sup>+</sup> = N) and 401.9 eV (Ar N=N<sup>+</sup> = N) and the appearance of a band at 400.6 eV due to the formation of C-N bonds. The presence of F 1s signal at 686 eV is an additional indication of the formation of ND-mannose (**Figure 2.3c**).

To validate further the covalent linking of the glycan to ND-PFDA, a solution of ND-PFPA in acetonitrile was mixed with an aqueous solution of mannan and left for 24 h. The characteristic N<sub>3</sub> vibration band at 2128 cm<sup>-1</sup> was still present on ND-PFPA and that confirmed the glycan interaction with the dopamine ligand on the NDs. Representative transmission electron microscopy (TEM) images of ND-mannose and ND-mannan (**Figure 2.3d**) show the presence of spherical particles with a mean diameter of 24 nm for all structures, regardless of the glycan presence on their surface.



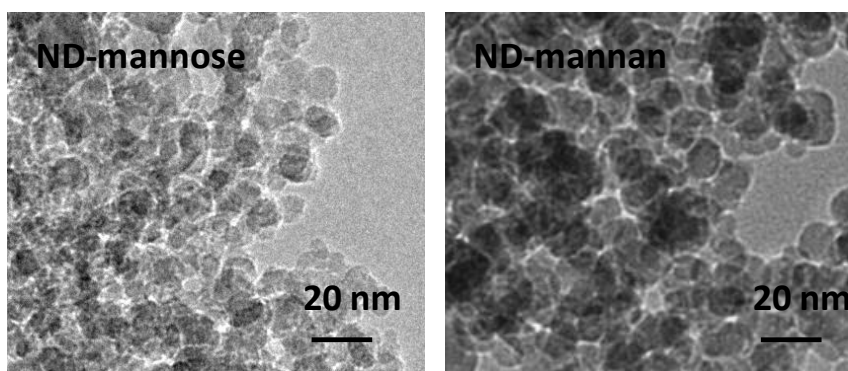
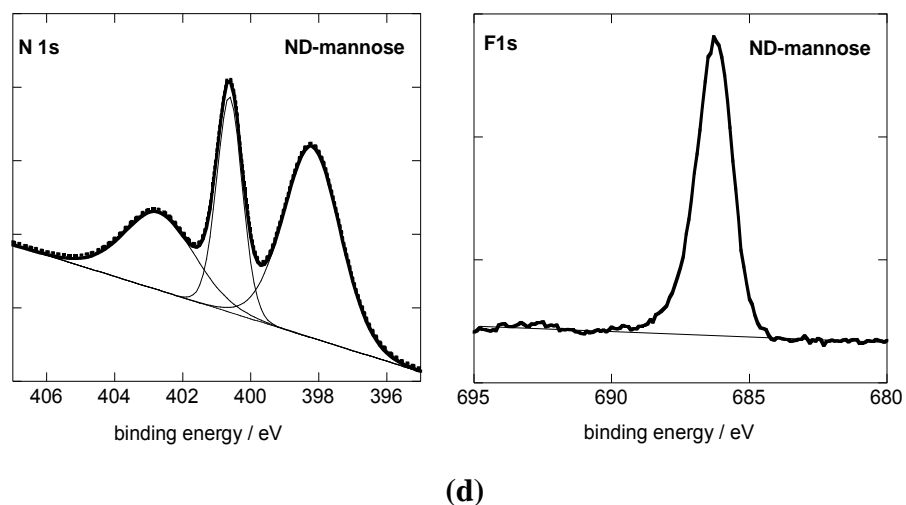


**Figure 2.3:** a) FTIR spectra of ND-mannose (black) and ND-mannan (grey); b) N 1s spectrum of ND-mannose, c) F 1s spectrum of ND-mannose, d) TEM images of ND-mannose and ND-mannan.

The amount of glycans that were gradually integrated into the ND-PFPA was analyzed as well with the usage of the well-established phenol–sulfuric acid assay and that was proved to be glycan dependent (**Table 2.2**).

**Table 2.2:** Physical properties of different glycan-NDs

Table 2. Physical properties of different glycan-NDs.				
Materials	Diameter [nm]	PD <sup>[a]</sup>	Zeta potential [mV]	Sugar loading [ $\mu\text{g mg}^{-1}$ ND]
mannose-NDs	127 ± 7	0.190 ± 0.020	32 ± 2	95 ± 9
glucose-NDs	104 ± 3	0.163 ± 0.031	28 ± 2	89 ± 7
galactose-NDs	113 ± 3	0.145 ± 0.026	30 ± 2	96 ± 10
lactose-NDs	97 ± 3	0.148 ± 0.030	31 ± 2	110 ± 12
sucrose-NDs	105 ± 3	0.159 ± 0.026	25 ± 2	138 ± 15
maltose-NDs	98 ± 3	0.167 ± 0.024	25 ± 2	120 ± 15
mannan-NDs	101 ± 3	0.187 ± 0.025	17 ± 2	315 ± 20

[a] Polydispersity index.

Talking about mannose, it should be noted that the loading of sugar can be compared to the mannose-ND that were formed with the usage of “click”. Disaccharide-modified NDs has the amount of incorporated saccharides which is almost twice higher than in mannose and the highest loading of sugar was common for mannan-NDs.

### 2.3. Lectin binding assays

The affinity binding study was focused on the glyco-NDs that has a range of fluorescently labeled lectins (**Figure 2.4**). FITC-labeled Concanavalin A from *Canavalia ensiformis* (Con A) and FTIR-labeled *Lens culinaris* (LENS) are actually specific to mannopyranoside and were used in terms of the positive controlling. For the negative control for glucose-, mannose-, sucrose-, maltose- and mannan-modified ND particles, the  $\alpha$ -D-galactopyranose specific *Arachis hypogaea* (PNA) was used, while Con A and LENS were negative controls for galactose-modified NDs. It is expected for Lactose-NDs to interact with all lectins since indicated disaccharide is retrieved from the condensation of galactose and glucose-forming  $\beta$ -(1→4)glycosidic linkage.

With the usage of the fluorescence intensities that were recorded after the interaction of glyco-NDs solutions within 30 min with different lectins confirm that the binding affinities of the photolinked sugars are congruent with the expected binding characteristics for each lectin.

Several times larger fluorescence signals were shown by mannose-modified NDs during the incubation with the Con A and LENS in comparison with the incubation with PNA because of the higher binding affinity.

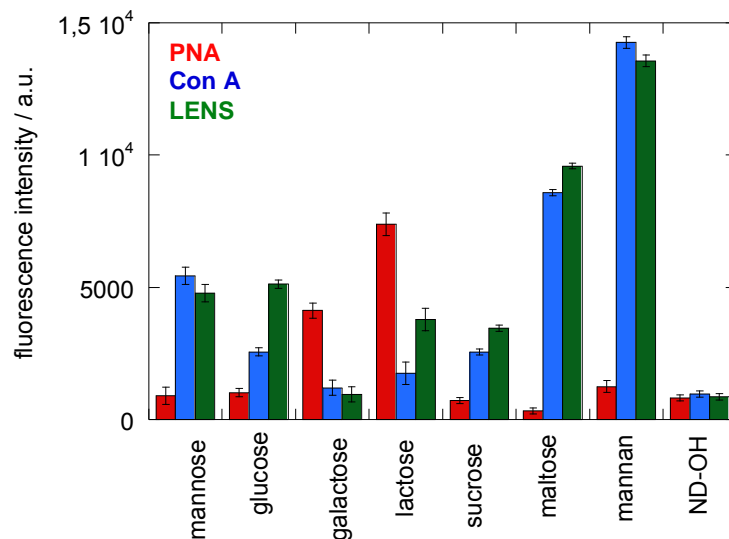


**Figure 2.4:** Fluorescence intensities evaluated using FITC-labeled lectins after reaction with glycan-terminated NDs in a 1/1 ratio ( $1 \text{ mg mL}^{-1}$ ) in tris buffer solution (pH 7.4 containing  $\text{Mg}^{2+}$ ,  $\text{Ca}^{2+}$ ,  $\text{NaCl}$ ): Fluorescent measurements were performed using an excitation wavelength of 485 nm and an emission wavelength of 520 nm; the results are derived from the data of 4 independent experiments.

However, the results were identical for the fluorescence intensity recorded for mannose-NDs in the presence of FITC-labeled PNA that was measured with the ND-OH. Indicated level of fluorescence tends to be most likely linked to non-specific protein interaction with the surface of the particle. Opposite behavior is shown by galactose-modified NDs: strong fluorescence due to the incubation with PNA and weak with Con A and LENS lectins. The fluorescence signal upon incubation is strongest for LENS, lower for Con A, and weak for PNA when we are talking about glucose-NDs. The tetrameric lectin Con A was next to mannose and reported binding site specific to glucose, with a lesser extent. Correlation to the indicated difference in affinity of the lowered fluorescence signal upon incubation of glucose-ND is found due to the comparison with Con A binding to glucose-ND specific LENS.

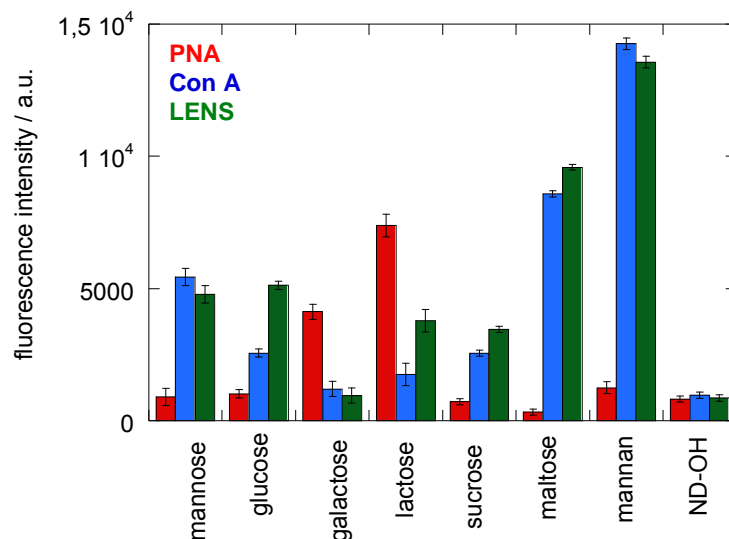


**Figure 2.4:** Fluorescence intensities evaluated using FTIC-labeled lectins after reaction with glycan-terminated NDs in a 1/1 ratio ( $1 \text{ mg mL}^{-1}$ ) in tris buffer solution (pH 7.4 containing  $\text{Mg}^{2+}$ ,  $\text{Ca}^{2+}$ ,  $\text{NaCl}$ ): Fluorescent measurements were performed using an excitation wavelength of 485 nm and an emission wavelength of 520 nm; the results are derived from the data of 4 independent experiments.

For further investigation of the indicated coupling method, together with the specificity of the glycans, disaccharide and polysaccharide that are surface-bonding, they were photochemically linked to ND-PFPA in order to determine their affinity to the three lectins. Lactose-NDs with PNA or LENS interaction resulted into the twice more of the fluorescence signal for PNA. It means that this disaccharide tends to be coupled with the NDs through its glucose end. For sucrose-NDS (a disaccharide that is composed of glucose and fructose) no interaction with PNA was noticed, while the interaction with glucose-specific Con A and LENS was higher, meaning that some of the sucrose is linked via the fructose end to ND-PFPA. With the usage of maltose-ND, two-unit glucose disaccharide formed with an  $\alpha$ -(1 $\rightarrow$ 4) bond, strongly binds with the Con A and LENS, which is stronger than the bind that was observed with mannose. The strongest interaction with Con A and LENS are observed with mannan-modified NDs: these particles showed a three times higher sugar loading than mannose-NDs, which correlates to an approximately three times larger fluorescent signal.

## 2.4. Effect of mannose-NDs and mannan-NDs on agglutination of *E. coli* UTI89 strains

### 2.4.1. Fluorescence-based agglutination assay in the presence of mannose and mannose-NDs

The next step was the examination of mannose-NDs and mannan-NDs affinity to uropathogenic *E. coli* UTI89. As it was already mentioned, FimH, a lectin located at the extremity of type 1 fimbriae, is a major virulence factor produced by *E. coli* UTI89, which contributes to the colonization of tissue due to its specific recognition of the terminal  $\alpha$ -D-mannopyranosyl units present on cell-surface glycoproteins. Interference of the interaction became possible due to the mannose-modified NDs that was formed by “click” as a chemistry of propargyl and/or azide-modified mannose derivatives. In order to research the potential of the mannose-NDs that were formed photochemically, it was necessary to check whether indicated particles show increased agglutination effects to *E. coli* UTI89 in comparison with the free mannose in solution. For the mentioned purpose, fluorescence-based agglutination assay was used (34). It is mainly grounded on the mixture of different concentrations of mannose and mannose-NDs with fluorescently labeled *E. coli* UTI89 formed through genetic modification to express turbo FP635 (Katushka) fluorescent proteins, emitting at 635 nm (upon excitation at 580 nm). Diverse fluorescence images of Katushka expressing *E. coli* after interaction for 4 h at 4 °C with different concentrations of mannose-NDs (1–300 mg mL<sup>-1</sup>) are presented on (Figure 2.5).

For this purpose, the influence of ND-OH and mannose in solution was researched as a controlling aspect. These agglutination tests show that mannose, as expected, shows no *E. coli* UTI89 agglutination in the tested concentration range. In comparison with the free mannose in solution, mannose-NDs display a concentration dependent agglutination behavior at a minimal concentration of 50 mg mL<sup>-1</sup>.

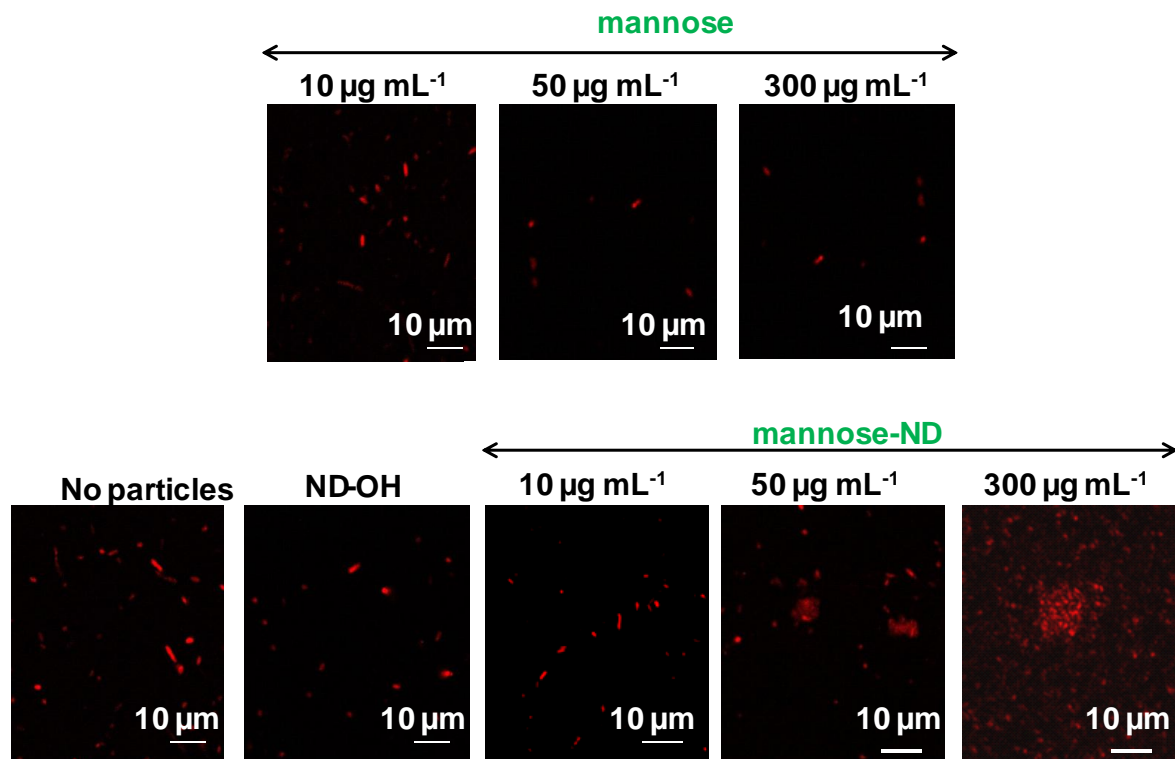


**Figure 2.5:** Fluorescence-based agglutination assay for: Fluorescence images of Turbo FP635 (Katushka protein) expressing *E. coli* UTI89 ( $1 \cdot 10^8$  cfu ml<sup>-1</sup>) in the presence of different concentrations of mannose, in the absence of particles (no particles) and in the presence of ND-OH ( $100 \text{ mg mL}^{-1}$ ) and different mannose-NDs (the values correspond to total mannose concentration in the solution and is directly comparable with the results of free mannose).

#### 2.4.2. Fluorescence-based agglutination assay in the presence of mannan and mannan-NDs

Furthermore, in a comparable manner, the agglutination behavior of mannan and mannan-NDs were investigated. A cell-wall component of microorganisms is called Mannan, which consists of d-mannose residues expanded by  $\alpha$ -(1→6)-,  $\alpha$ -(1→3)-,  $\alpha$ -(1→2)- linkages. Park with the colleagues described the formation of carboxylic mannan-coated iron oxide nanoparticles to target antigen-presenting cells (APCs), including macrophages, by the specific interaction between the mannose ligand and the mannose receptors on APCs. Mannan was chosen as an

integral component in NDs in order to take advantage of the predicted high binding affinity towards *E. coli* UTI89 because of the presence of multiple mannose ligands in this polysaccharide.

(**Figure 2.6**) presents the results of mannan and mannan-NDs addition to a solution of *E. coli* UTI89. In contrast to mannose only (Figure5), addition of 100 mgmL<sup>-1</sup> mannan reveals partial *E. coli* UTI89 agglutination. Moreover, mannan-ND particles have an ability to agglutinate *E. coli* with an onset at concentrations as low as 10 mg mL<sup>-1</sup>. Indicated statement corresponds with the usually presented multivalence of mannan on nanoparticles.

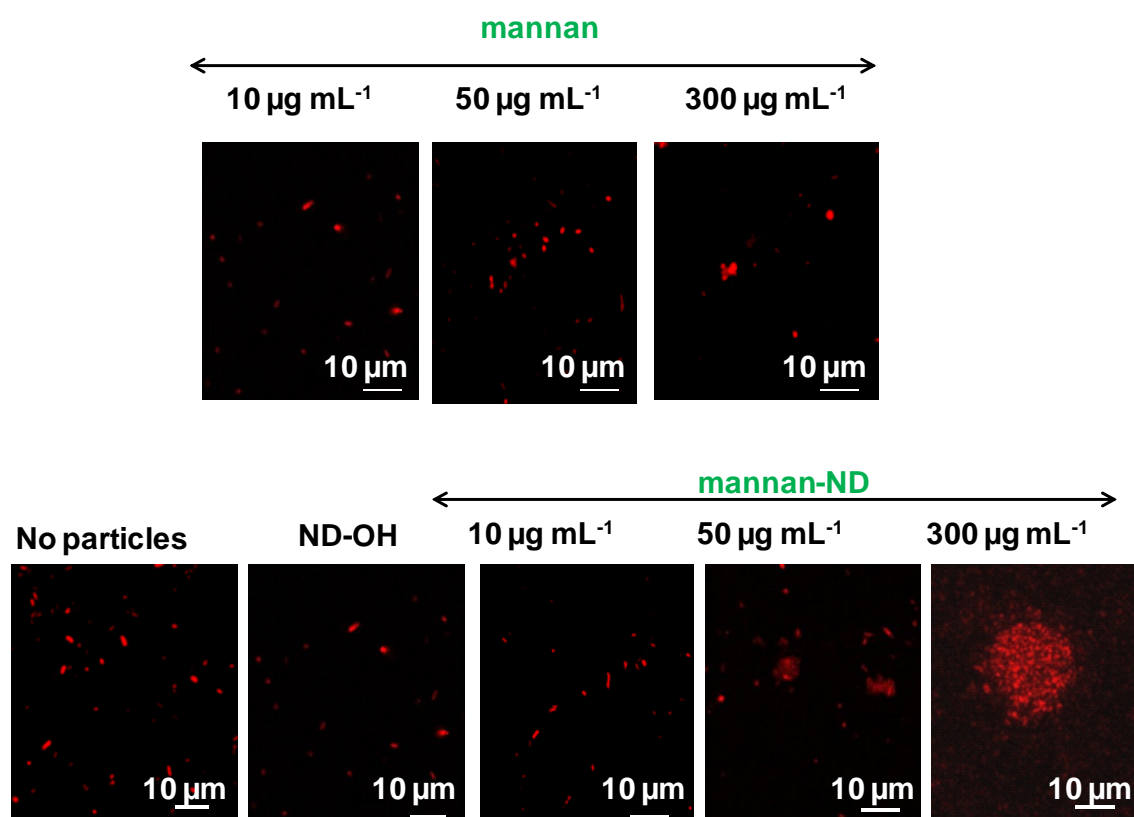


**Figure 2.6:** Fluorescence-based agglutination assay for: Fluorescence images of Turbo FP635 (Katushka protein) expressing *E. coli* UTI89 ( $1 \times 10^8$  cfu mL<sup>-1</sup>) in the presence of different concentrations of mannan, in the absence of particles (no particles) and in the presence of ND-OH (100 mg mL<sup>-1</sup>) and different mannan-NDs (the values correspond to total mannan concentration in the solution and is directly comparable with the results of free mannan).

## 2.5. Conclusions

In conclusion, it should be stated that we have presented that photochemical linking of unmodified mono-, di-, and polysaccharides to nanodiamond particles pre-modified with perfluorophenylazide ligands is a general method for coupling underivatized carbohydrates to diamond nanostructures. The coupling method that is based on photochemically induced CH insertion is considered to be fast and is capable of providing a high coupling yield. Furthermore, the resulting glyco-NDs maintained their predicted binding affinity and specificity towards their partner lectins. Obtained results correspond to the previous researches that were conducted for the description of the effectiveness of photochemically formed glycan surfaces to the selective interaction with specific lectins. The generality of photochemical approach of forming glyco-NDS was additionally demonstrated via the formation of different disaccharide and a polysaccharide modified NDs. It should be noted, however, that with the usage of the disaccharide-modified NDS, lactose preferentially couples through the glucose end to NDs, while with the usage of sucrose, the fructose end has a tendency to bind photochemically. The main reasons for such a behavior are yet to be researched. “Click” chemistry approaches demonstrate a higher control degree for anchoring disaccharides onto particles. However, indicated limitation is not common and is not present in polysaccharides such as mannan and the it is believed to be used only for such kinds of glycans. It became one of the main reasons to research the potential of mannan-NDs’ interaction with *E. coli* U TI89. With the usage of the fluorescence-based agglutination assay, it was showed that mannan-NDs display *E. coli* agglutination at concentrations of  $10 \text{ mg mL}^{-1}$ , which is much lower than for free mannan and mannose-NDs. Taken together, the findings presented here show that such nanostructures should be further developed and evaluated as potential anti-adhesives for countering bacterial colonization and infections *in vivo*.

## 2.6. References

1. Flores-Mireles AL, Walker JN, Caparon M, Hultgren SJ. Urinary tract infections: epidemiology, mechanisms of infection and treatment options. *Nature Reviews Microbiology*. 2015; 13(5):269-84.
2. De M, Ghosh PS, Rotello VM. Applications of nanoparticles in biology. *Advanced Materials*. 2008; 20(22):4225-41.
3. Mochalin VN, Shenderova O, Ho D, Gogotsi Y. The properties and applications of nanodiamonds. *Nature nanotechnology*. 2012; 7(1):11-23.
4. Barras A, Martin FA, Bande O, Baumann J-S, Ghigo J-M, Boukherroub R, et al. Glycan-functionalized diamond nanoparticles as potent *E. coli* anti-adhesives. *Nanoscale*. 2013; 5(6):2307-16.
5. Hartmann M, Betz P, Sun Y, Gorb SN, Lindhorst TK, Krueger A. Saccharide-Modified Nanodiamond Conjugates for the Efficient Detection and Removal of Pathogenic Bacteria. *Chemistry—A European Journal*. 2012;18(21):6485-92.
6. Fessele C, Wachtler S, Chandrasekaran V, Stiller C, Lindhorst TK, Krueger A. Thiourea-Bridged Nanodiamond Glycoconjugates as Inhibitors of Bacterial Adhesion. *European Journal of Organic Chemistry*. 2015; 2015(25):5519-25.
7. Khanal M, Larssonneur F, Raks V, Barras A, Baumann J-S, Martin FA, et al. Inhibition of type 1 fimbriae-mediated *Escherichia coli* adhesion and biofilm formation by trimeric cluster thiomannosides conjugated to diamond nanoparticles. *Nanoscale*. 2015; 7(6):2325-35.
8. Khanal M, Turcheniuk V, Barras A, Rosay E, Bande O, Siriwardena A, et al. Toward multifunctional “clickable” diamond nanoparticles. *Langmuir*. 2015;31(13):3926-33.
9. Barras A, Lyskawa J, Szunerits S, Woisel P, Boukherroub R. Direct functionalization of nanodiamond particles using dopamine derivatives. *Langmuir*. 2011; 27(20):12451-7.

## CHAPTER III

### Menthol modified nanodiamonds and their antibacterial properties

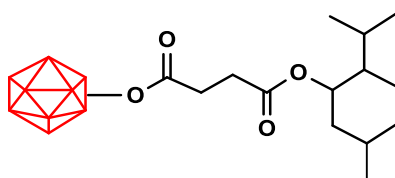
#### 3.1. Introduction

Public health is often threatened by bacterial infections. A lot of effort was put into the development of the methods that are rather sensitive and quick, they also allow to identify pathogen strain, together with the destruction or inhibition of pathogens and their actions (1-3). Even though, many mechanisms of the bacteria infection are already discovered, nanostructured materials are still not capable of displaying properties and features against the biofilms (1, 4, 5) and therefore the development of antibacterial nanostructures is still a crucial task for the modern science. One of the effective solutions against bacterial infections is considered to be the usage of nanoparticles (6, 7). Indicated structures are capable of delivering polyvalent effects on the concentration of antibacterial agents and their surface functions. Enhanced efficacy can be presented with the usage of materials that are considered antibacterial, for example, silver (8, 9). Regardless of the presence of some successful studies (10), general activity is dependent on the shape and size of the particle, smaller parts of which can demonstrate higher activity (11, 12). In addition, some statements about the cytotoxic effects of silver nanoparticles on human body were presented (13). Furthermore, due to the usage of Ag NPs, the loss of antibacterial activity by the aggregation can be noticed (14).

Nanodiamond particles (NDs) can be considered as an alternative compound for the indicated purpose. NDs have several advantages over the carbon-based materials, for example, fullerenes and carbon nanotubes, and are the following: they are optically transparent, completely inert, can be functionalized in many ways, biocompatible depending on the way of application (15, 16). Their surface characteristics *in vivo* define their toxicity (17), and particles of ND are not toxic for cells (17, 18) and can be used in different biomedical applications. In the recent studies, antibacterial activity of diamond particles (19, 20), together with their potential of interference with the biofilm formation (1), were already presented. Anti-adhesive strategy is mainly dependent on the interfering with type 1 fimbriae-mediated mannose recognition events (21). Indicated disrupting activity of biofilm was not present in the observations of other glyco-

nanoparticles (glyco-NPs) such as glycofullerenes, gold-based glyco-NPs or for other multivalent mannose-derived molecules (2, 22). Wehling et al. during their research came up to the conclusion that bactericidal activity of diamond particles is directly linked to their surface chemistry, which becomes the main ground and force for antibacterial effects (20).

In Chapter II, we have highlighted the potential of mannose modified diamond particles to interfere with biofilm formation (21). Motivated by these results, we investigate in this chapter the antimicrobial properties of nanodiamonds modified with menthol (**Figure 3.1**). Menthol, also known as mint camphor, is a naturally occurring cyclic terpene alcohol of plant origin, which has been used since antiquity for medicinal purposes (23, 24). It is a major constituent in the essential oils of *Mentha Canadensis L.* (cornmint) and peppermint possessing well-known cooling characteristics and a residual minty smell of the oil remnants from which it was obtained. Several studies have additionally demonstrated that next to effect of sensory parameters, menthol has antibacterial and antifungal activity (25, 26). However, the antimicrobial activity was reported to be lower compared to antibiotics such as penicillin (27). More recently, Imbert and co-workers showed the *in vitro* activity of terpenes, including that of menthol, against *Candida* biofilms (28). We show here that ND-menthol particles affect moderately *S. aureus* and *E. coli* growth in a concentration dependent manner. In addition, the ND-menthol particles are found to inhibit *S. aureus* and *E. coli*-driven biofilm growth significantly.



**ND-menthol**

**Figure 3.1:** Menthol modified diamond nanoparticles

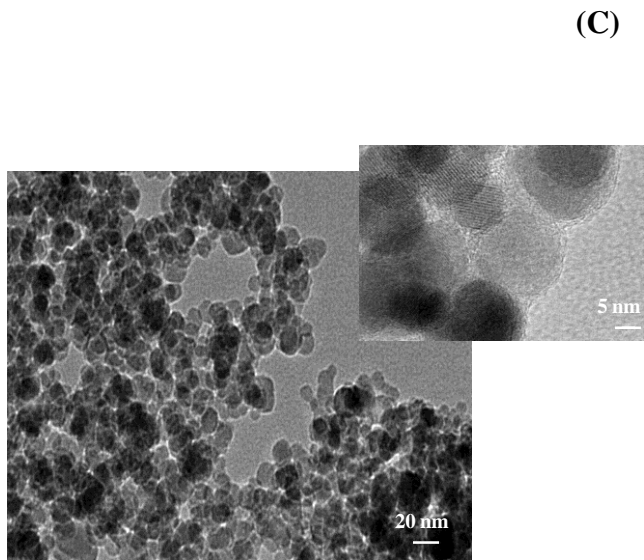
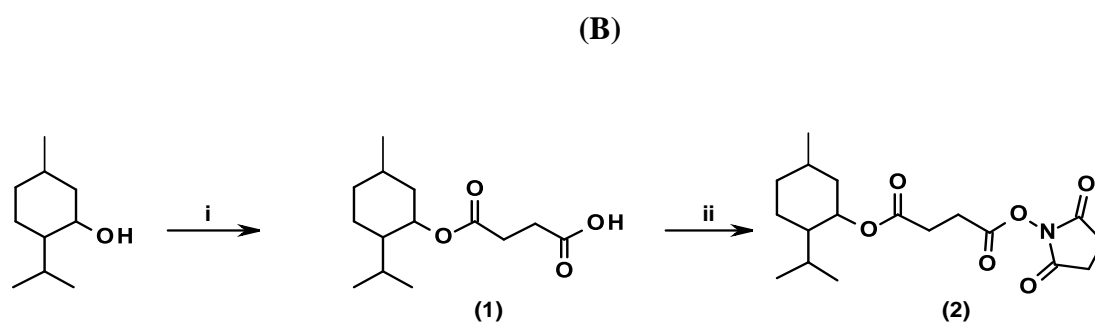
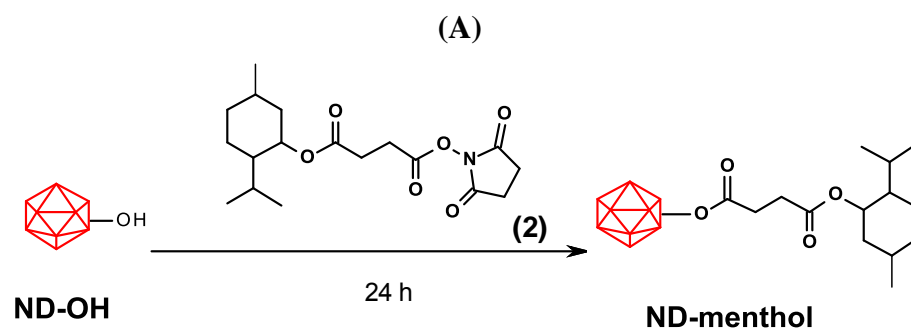
### 3.2. Synthesis and physico-chemical properties of ND-Menthol particles

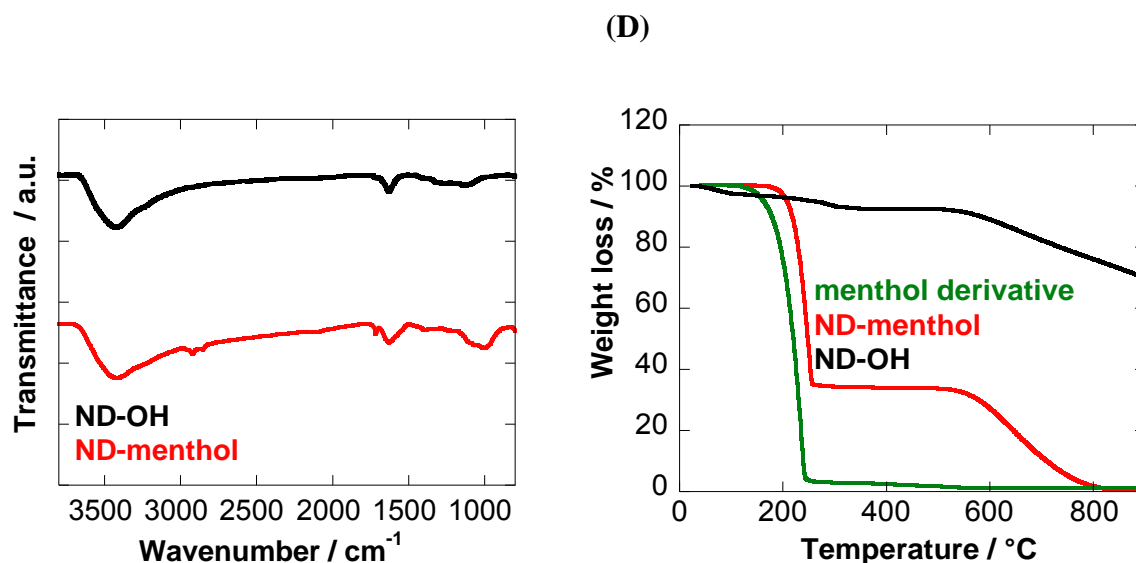
As a reliable strategy to design antibacterial materials, covalent linking of antibacterial agents to surfaces has been considered (29, 30). We performed for the covalent linking of a carboxylic acid

modified menthol derivative (**1**) to the hydroxyl groups of ND particles via the reaction of esterification, aiming to determine the properties of the menthol modified ND particles that are considered to be antibacterial (**Figure 3.1**). Fourier transform infrared spectroscopy (FTIR) allowed successful integration of menthol moiety onto ND (**Figure 3.2A**). ND-OH particles show a broad peak at  $3400\text{ cm}^{-1}$  assigned to the vibration of surface hydroxyl groups or/and adsorbed water molecules, and an additional sharper one at  $1633\text{ cm}^{-1}$  due to the bending mode  $\delta_{(\text{OH})}$  of surface hydroxyl groups on the NDs. Furthermore, the band at  $1107\text{ cm}^{-1}$  is indicative of the presence of C-O-C- functions of cyclic ethers. The FTIR spectrum of the ND-menthol particles displays in addition to bands at  $3400\text{ cm}^{-1}$  (vibration of surface hydroxyl groups or/and adsorbed water molecules,)  $1633\text{ cm}^{-1}$  (bending mode of surface hydroxyl groups) and  $1107\text{ cm}^{-1}$  (C-O-C- functions of cyclic ethers), a band at  $1717$  characteristic of the C=O stretching of the installed ester function. The C-H stretching vibration modes in menthol are seen between  $2850\text{-}2970\text{ cm}^{-1}$ .

TEM images of ND-menthol particles (**Figure 3.2B**) show that spherical particles with a size distribution in the range of  $15\pm 5$  nm in diameter are present. The hydrodynamic diameter of ND-menthol particles is  $92 \pm 10$  nm, comparable to that of ND-OH (89 nm) with a zeta potential of  $29.5 \pm 0.5$  mV, slightly lower than that of ND-OH ( $35.3 \pm 1.6$  mV) (**Table 3.1**).

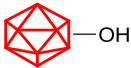
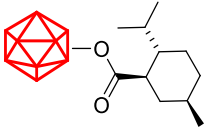
In order to get more information regarding the strength of the bonding between menthol derivative (**2**) to the surface of ND-OH particles, thermogravimetric analysis of ligand (**2**), ND-OH and ND-menthol particles were used (**Figure 3.2C**). The TGA thermogram of the as-received ND-OH particles indicates that they are stable up to  $550\text{ }^{\circ}\text{C}$  without any significant loss of mass(31, 32). TGA measurements show a weight loss of  $\approx 7.45\%$  above  $95\text{ }^{\circ}\text{C}$  mainly because of the absorbed water. Menthol derivative (**2**) decomposes beyond  $\approx 150\text{ }^{\circ}\text{C}$ . The removal of the covalently linked menthol derivative (**2**) shows its decomposition at temperatures above  $\approx 200\text{ }^{\circ}\text{C}$ . The weight loss between  $200\text{ -}300\text{ }^{\circ}\text{C}$  corresponding to the removal of the menthol acid (**1**) is around  $58\%$  indicating a surface loading of menthol derivative (**2**) of  $2.1\pm 0.2\text{ mmol g}^{-1}$ .





**Figure 3.2:** (A) Schematic illustration of the stepwise chemical functionalization of nanodiamond particles (ND) to give the target ND-menthol cluster together with synthetic route to menthol derivative (2): (i) succinic anhydride, 4-DMAP, CHCl<sub>3</sub>, reflux, overnight, 84 %; (ii) NHS, DCC, CH<sub>2</sub>Cl<sub>2</sub>, r.t., overnight, 95%; (B) FTIR spectra of ND-OH (black) and ND-menthol (red); (C) Transmission electron microscopy (TEM) images of ND-menthol particles together with histogram of particle size distribution; (D) Thermogravimetric analysis of and menthol derivative (2) (green), ND-menthol (red) and ND-OH (black).

**Table 3.1:** Physico-chemical properties of of ND-OH and ND-menthol.

		Hydrodynamic diameter (nm)	PI <sup>a</sup>	Zeta potential (mV)
	<b>ND-OH</b>	89 ± 13	0.246 ± 0.002	35.3 ± 1.6
	<b>ND-menthol</b>	92 ± 10	0.232 ± 0.015	29.5 ± 0.5

### 3.3. Antimicrobial activity of the ND-menthol particles

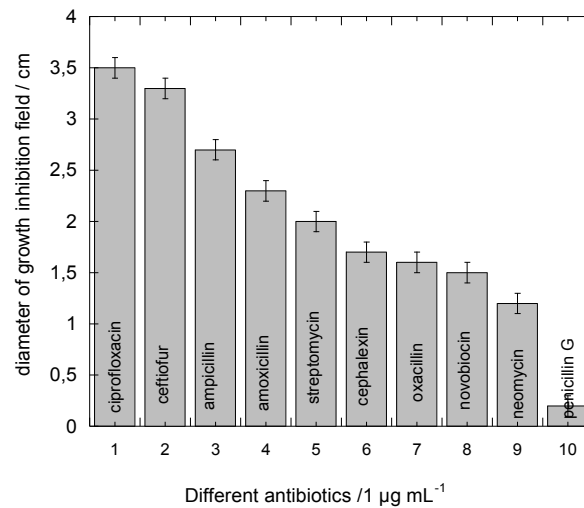
The testing of the ND-menthol particles in terms of the formation and growth of the pathogens and bacteria induced biofilm, Gram-positive *S. aureus* and Gram-negative *E. coli* were used as model organisms. The usage of the indicated bacteria is justified by the following reasons: *S. aureus* are extremely versatile pathogenic bacteria that cause a wide range of syndromes, ranging from minor skin and soft tissue infections to life-threatening pneumonia (33, 34). Gram-negative *E. coli* bacteria that are often used as a control organism in microbiological assays, are present within the gastro- intestinal (GI) tract, or as an intra- or extra-intestinal pathogen. Most of the modern antibiotics are taken orally, and that is why it is important to research effect of the compound on the normal GI flora. The disruption of the GI flora is rather common, however, complete removal of strains or a significant change of the required proportions of the constituent organisms might lead to opportunistic infection by *E. coli*, or any other organisms. Main factors of virulence that are associated with this organism are presented in the attachment of pili that facilitate adherence to the mucosal lining of the GI or urinary tract (35).

In order to research the level of the antimicrobial activity of the ND-menthol particles, they need to be placed against the already known bactericide agents in order to give a positive control. Using a range of 10 common antibiotics at a concentration of  $1 \mu\text{g ml}^{-1}$ , an antibiotic sensitivity test was conducted. The way different antibiotics reacted towards *E. coli* growth was presented by the usage of the standard microbiological technique of measuring the size of the zone of inhibition around the point where the antibiotic was placed (**Figure 3.3**). Significantly weak inhibition was noticed for penicillin G, while ceftiofur and ciprofloxacin showed relatively strong activity. Basing on the results of the sensitivity test, as a classical antibiotic with an intermediate effect, ampicillin was chosen and was also used for the comparison in further experiments

Presence of the ND-menthol particles at different concentrations was maintained within six-hour time period and the presence of the planktonic growths of *S. aureus* and *E. coli* was researched (**Figure 3.3**). The presence of unmodified ND-OH ( $10 \mu\text{g mL}^{-1}$ ) and ampicillin ( $10 \mu\text{g mL}^{-1}$ ) was used as a control method to investigate the effect of bacterial growth. **Figure 3.3A** shows that while ND-OH particles do not influence the planktonic growth of *S. aureus*, ND-menthol

particles had a concentration dependent effect on the growth of *S. aureus* by moderately reducing the growth of the Gram-positive pathogen. However, with the highest concentration tested, the presence of antibiotic significantly reduced the growth of *S. aureus*.

(A)



(B)

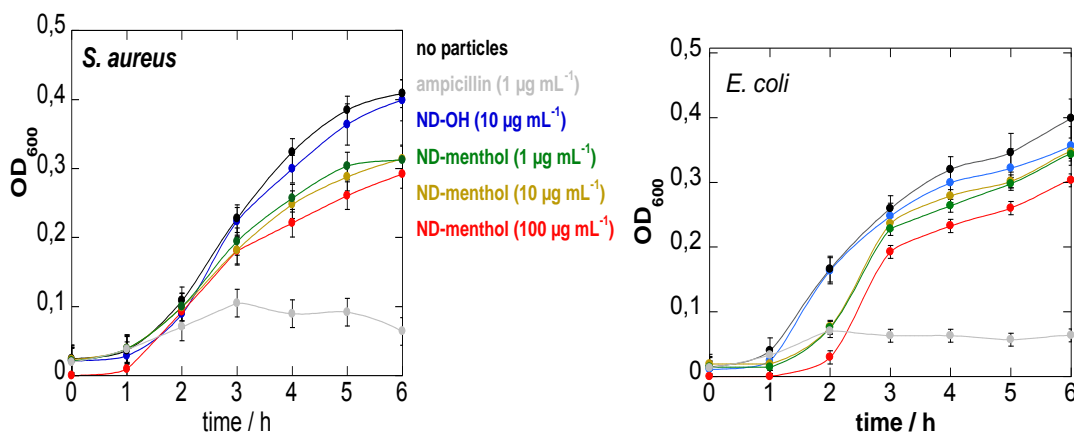


**Figure 3.3:** (A) Antibiotic action on *E. coli* growth on agar plates; (B) . Growth curve of *S. aureus* and *E. coli* in the presence of ND-OH ( $10 \mu\text{g mL}^{-1}$ ), ampicillin ( $10 \mu\text{g/mL}$ ) and ND-menthol at  $1, 10$  and  $100 \mu\text{g mL}^{-1}$ .

For *E. coli*, similar behavior was observed (**Figure 3.4B**). During the first 2 hours, inhibition of the *E. coli* growth was present even with low concentrations of ND-menthol and was compromised after allowing the planktonic growth of *E. coli*. LIVE/DEAD test (Invitrogen), by following the instructions of manufacturer, was used to investigate the effect of ND-menthol on the growth of *S. aureus* and *E. coli*. The fluorescence images in **Figure 3.4** show cell growth for *S. aureus* and *E. coli* in the absence (control) and presence of ND-menthol (100  $\mu\text{g/mL}$ ) and after being stained with the LIVE (green)/DEAD (red) stains.

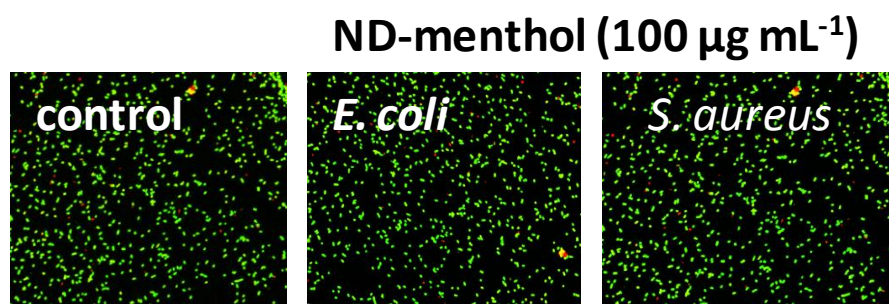


**Figure 3.4:** Viability of *S. aureus* and *E. coli* imaged by the LIVE/DEAD<sup>®</sup> BacLight<sup>™</sup> assay (x 40 magnification) (a) control *E. coli* (no NDs present); (b) ND-menthol. Green fluorescence indicates live cells while red or yellow fluorescence indicates dead or compromised cells.

Obtained results allow to state that ND-menthol particles do not alter the bacterial viability of *S. aureus* and *E. coli*. and can be considered as non-toxic. Toxic effects on the structures of the membrane were used to explain antimicrobial activity of menthol, however, exact mechanism of action are not yet fully researched (25). Menthol effect on the cell permeability is described by penetration between the fatty acid chains making up the membrane lipid bilayers, disrupting lipid packaging and changing membrane fluidity. Indicated process results into the alteration of the surface, together with the morphological modifications of gram-positive and gram-negative bacteria and in leakage of intracellular materials. Linking of menthol to ND particles seems to limit bactericidal activity of menthol. Antibacterial effect of diamond particles is usually described via its zeta-potential, meaning that particles with positive potential demonstrated no effect, but those with negative zeta potential were shown to disrupt the cell wall and cytoplasmic

membrane to release the cytoplasm from the cell (36). ND-OH particles and ND-menthol should have positive zeta-potential (**Table 3.1**). According to Wheling *et al.* (20), antibacterial activity of NDs is linked to the presence of partially oxidized and negatively charged surfaces, specifically those containing acid anhydride groups: they were able to obtain indicated statement due to the research of the bactericidal activity of partially oxidized NDs. Basing on the FTIR image of ND-OH and ND-menthol particles (**Figure 3.2A**), the presence of acid anhydride groups with an absorption band at around 1850-1750  $\text{cm}^{-1}$  is not visible explaining in addition the presence of viable bacteria.

There were strong reasons to believe that ND-menthol particles might affect the adhesion capacitance of the pathogens, even though ND-menthol particles were found to not interference with the development of the planktonically growth of *S. aureus* and *E. coli* (28). That is why there was a need to investigate potential of the different nanostructures to inhibit *S. aureus* and *E. coli* biofilm formation further. For *S. aureus*, dose-dependent inhibition of biofilm formation was present for ND-menthol particles: the results are shown on **Figure 3.5A**. In all cases, for ND-menthol particles, strong biofilm inhibition was observed.

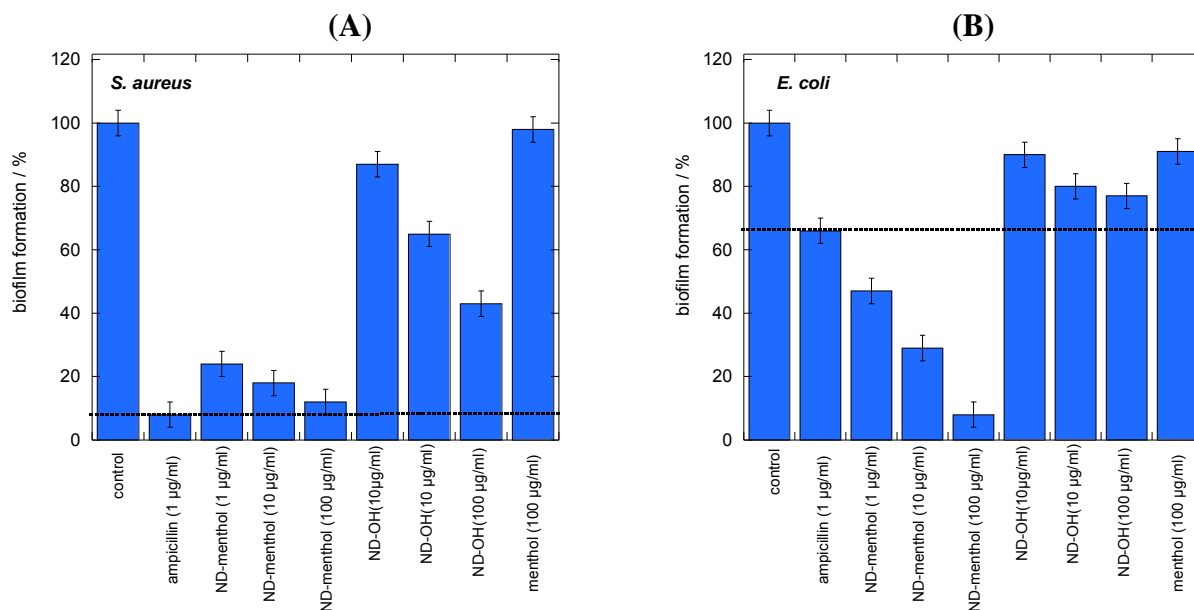


**Figure 3.5:** Biofilm formation of (A) *S. aureus* and (B) *E. coli* in the absence and presence of ND-menthol (1, 10, 100  $\mu\text{g mL}^{-1}$ ), ND-OH, ampicillin (1  $\mu\text{g mL}^{-1}$ ) and menthol (100  $\mu\text{g mL}^{-1}$ ).

At a particle concentration of 100  $\mu\text{g mL}^{-1}$  the inhibition of biofilm formation was almost equal to the effect of the antibiotic ampicillin that was used in the study. Free menthol (100  $\mu\text{g mL}^{-1}$ ) did not present any significant inhibition of the biofilm. ND-OH particles are capable of showing rather moderate inhibition of biofilm at even higher concentrations. One of the possible reasons for the increased biofilm inhibition effect of ND-menthol over free menthol is most likely presented in their more efficient harnessing of a multivalent effect. The difference might also be driven by the intrinsic physiochemical properties of the NDs. More detailed studies are needed in order to fully describe menthol modified NDs' antibiofilm activity, but indicated alteration in bacteria membrane fluidity in the presence of menthol (25) seems to reduce the adherence capacity of *S. aureus*. This is also relevant for *E. coli* biofilms. For *E. coli*, ND-menthol particles can be compared in terms of effect with ampicillin, even at the lowest levels of concentration (**Figure 3.5B**), together with the high ND-menthol concentrations resulted in strong biofilm inhibition.

### 3.4. Conclusions

This thesis was aimed at the demonstration of the menthol-conjugated nanodiamond effects on *S. aureus* and *E. coli*-mediated biofilm formation. The strategy of conjugation was based on the formation of an ester bond between the hydroxyl groups of ND and the carboxylic acid group of a synthetic menthol derivative (**1**) proved to be highly efficient for the coupling of the antibacterial agent. It was noted that ND-menthol particles are capable of effective prevention of bacterial adhesion of Gram-negative and Gram-positive bacteria, and it is consistent with our earlier findings that integration of a biofilm inhibitor onto diamond particles has marked *E. coli* anti-adhesive activity. Furthermore, none of the substances (ND-OH and menthol controls) have shown any anti-adhesive activity, meaning that indicated activities are clearly specific for ND-menthol. Additionally, ND-menthol was capable of showing better inhibition in comparison with ampicillin even if the concentration of particles was low. It should be noted that the results

support driving biofilm-inhibitory activity by the presence of menthol moiety that was observed for the ND-menthol conjugation.

### 3.5. References

1. Barras A, Martin FA, Bande O, Baumann J-S, Ghigo J-M, Boukherroub R, et al. Glycan-functionalized diamond nanoparticles as potent *E. coli* anti-adhesives. *Nanoscale*. 2013; 5(6):2307-16.
2. Durka M, Buffet K, Iehl J, Holler M, Nierengarten J-F, Taganna J, et al. The functional valency of dodecamannosylated fullerenes with Escherichia coli FimH—towards novel bacterial antiadhesives. *Chemical Communications*. 2011; 47(4):1321-3.
3. Laurino P, Kikkeri R, Azzouz N, Seeberger PH. Detection of bacteria using glyco-dendronized polylysine prepared by continuous flow photofunctionalization. *Nano letters*. 2010; 11(1):73-8.
4. Herman A, Herman AP. Nanoparticles as antimicrobial agents: their toxicity and mechanisms of action. *Journal of nanoscience and nanotechnology*. 2014; 14(1):946-57.
5. Allaker RP, Memarzadeh K. Nanoparticles and the control of oral infections. *International journal of antimicrobial agents*. 2014; 43(2):95-104.
6. Akhavan O, Azimirad R, Safa S, Hasani E. CuO/Cu (OH)<sub>2</sub> hierarchical nanostructures as bactericidal photocatalysts. *Journal of Materials Chemistry*. 2011; 21(26):9634-40.
7. Qi G, Li L, Yu F, Wang H. Vancomycin-modified mesoporous silica nanoparticles for selective recognition and killing of pathogenic gram-positive bacteria over macrophage-like cells. *ACS applied materials & interfaces*. 2013; 5(21):10874-81.
8. Das MR, Sarma RK, Saikia R, Kale VS, Shelke MV, Sengupta P. Synthesis of silver nanoparticles in an aqueous suspension of graphene oxide sheets and its antimicrobial activity. *Colloids and Surfaces B: Biointerfaces*. 2011; 83(1):16-22.
9. Kim JS, Kuk E, Yu KN, Kim J-H, Park SJ, Lee HJ, et al. Antimicrobial effects of silver nanoparticles. *Nanomedicine: Nanotechnology, Biology and Medicine*. 2007; 3(1):95-101.
10. Liu J, Sonshine DA, Shervani S, Hurt RH. Controlled release of biologically active silver from nanosilver surfaces. *ACS nano*. 2010; 4(11):6903-13.

11. Panáček A, Kvítek L, Pucek R, Kolar M, Vecerova R, Pizurova N, et al. Silver colloid nanoparticles: synthesis, characterization, and their antibacterial activity. *The Journal of Physical Chemistry B*. 2006; 110(33):16248-53.
12. Pal S, Tak YK, Song JM. Does the antibacterial activity of silver nanoparticles depend on the shape of the nanoparticle? A study of the gram-negative bacterium *Escherichia coli*. *Applied and environmental microbiology*. 2007; 73(6):1712-20.
13. Wong KK, Liu X. Silver nanoparticles—the real “silver bullet” in clinical medicine? *MedChemComm*. 2010; 1(2):125-31.
14. Kong H, Jang J. Antibacterial properties of novel poly (methyl methacrylate) nanofiber containing silver nanoparticles. *Langmuir*. 2008; 24(5):2051-6.
15. Barras A, Lyskawa J, Szunerits S, Woisel P, Boukherroub R. Direct functionalization of nanodiamond particles using dopamine derivatives. *Langmuir*. 2011; 27(20):12451-7.
16. Barras A, Szunerits S, Marcon L, Monfilliette-Dupont N, Boukherroub R. Functionalization of diamond nanoparticles using “click” chemistry. *Langmuir*. 2010; 26(16):13168-72.
17. Marcon L, Riquet F, Vicogne D, Szunerits S, Bodart J-F, Boukherroub R. Cellular and *in vivo* toxicity of functionalized nanodiamond in *Xenopus* embryos. *Journal of Materials Chemistry*. 2010; 20(37):8064-9.
18. Liu K-K, Cheng C-L, Chang C-C, Chao J-I. Biocompatible and detectable carboxylated nanodiamond on human cell. *Nanotechnology*. 2007; 18(32):325102.
19. Perevedentseva E, Cheng C-Y, Chung P-H, Tu J-S, Hsieh Y-H, Cheng C-L. The interaction of the protein lysozyme with bacteria *E. coli* observed using nanodiamond labelling. *Nanotechnology*. 2007; 18(31):315102.
20. Wehling J, Dringen R, Zare RN, Maas M, Rezwani K. Bactericidal activity of partially oxidized nanodiamonds. *ACS nano*. 2014;8(6):6475-83.
21. Wu X-R, Sun T-T, Medina JJ. *In vitro* binding of type 1-fimbriated *Escherichia coli* to uroplakins Ia and Ib: relation to urinary tract infections. *Proceedings of the National Academy of Sciences*. 1996; 93(18):9630-5.

22. Lin C-C, Yeh Y-C, Yang C-Y, Chen C-L, Chen G-F, Chen C-C, et al. Selective binding of mannose-encapsulated gold nanoparticles to type 1 pili in Escherichia coli. *Journal of the American Chemical Society*. 2002; 124(14):3508-9.
23. Patel T, Ishiujii Y, Yosipovitch G. Menthol: a refreshing look at this ancient compound. *Journal of the American Academy of Dermatology*. 2007; 57(5):873-8.
24. A Farco J, Grundmann O. Menthol-pharmacology of an important naturally medicinal “cool”. *Mini reviews in medicinal chemistry*. 2013; 13(1):124-31.
25. Trombetta D, Castelli F, Sarpietro MG, Venuti V, Cristani M, Daniele C, et al. Mechanisms of antibacterial action of three monoterpenes. *Antimicrobial agents and chemotherapy*. 2005; 49(6):2474-8.
26. Iscan G, KIrimer N, Kürkçüoğlu Mn, Baser HC, DEMİrci F. Antimicrobial screening of *Mentha piperita* essential oils. *Journal of agricultural and food chemistry*. 2002; 50(14):3943-6.
27. Kotan R, Kordali S, Cakir A. Screening of antibacterial activities of twenty-one oxygenated monoterpenes. *Zeitschrift für Naturforschung C*. 2007; 62(7-8):507-13.
28. Dalleau S, Cateau E, Bergès T, Berjeaud J-M, Imbert C. *In vitro* activity of terpenes against *Candida* biofilms. *International journal of antimicrobial agents*. 2008; 31(6):572-6.
29. Tiraferri A, Vecitis CD, Elimelech M. Covalent binding of single-walled carbon nanotubes to polyamide membranes for antimicrobial surface properties. *ACS applied materials & interfaces*. 2011; 3(8):2869-77.
30. Al-Bataineh SA, Luginbuehl R, Textor M, Yan M. Covalent immobilization of antibacterial furanones via photochemical activation of perfluorophenylazide. *Langmuir*. 2009; 25(13):7432-7.
31. Krüger A, Liang Y, Jarre G, Stegk J. Surface functionalisation of detonation diamond suitable for biological applications. *Journal of Materials Chemistry*. 2006; 16(24):2322-8.
32. Pichot V, Comet M, Fousson E, Baras C, Senger A, Le Normand F, et al. An efficient purification method for detonation nanodiamonds. *Diamond and related materials*. 2008; 17(1):13-22.
33. Diekema D, Pfaller M, Schmitz F, Smayevsky J, Bell J, Jones R, et al. Survey of infections due to *Staphylococcus* species: frequency of occurrence and antimicrobial

susceptibility of isolates collected in the United States, Canada, Latin America, Europe, and the Western Pacific region for the SENTRY Antimicrobial Surveillance Program, 1997–1999. *Clinical Infectious Diseases*. 2001; 32(Supplement 2):S114-S32.

34. Boakes E, Kearns A, Ganner M, Perry C, Hill R, Ellington M. Distinct bacteriophages encoding Panton-Valentine leukocidin (PVL) among international methicillin-resistant *Staphylococcus aureus* clones harboring PVL. *Journal of clinical microbiology*. 2011; 49(2):684-92.

35. Zhang JP, Normark S. Induction of gene expression in *Escherichia coli* after pilus-mediated adherence. *Science*. 1996; 273(5279):1234.

36. Chwalibog A, Sawosz E, Hotowy A, Szeliga J, Mitura S, Mitura K, et al. Visualization of interaction between inorganic nanoparticles and bacteria or fungi. *Int J Nanomedicine*. 2010; 5:1085-94.

## CHAPTER IV

### Verte porfin modified gold nanorod/SiO<sub>2</sub> nanostructures for the photodynamic eradication of *Escherichia coli*

#### 4.1. Introduction

The combination of nanostructures with light activation to kill microorganisms in a photodynamic and/or photothermal approach has been established over the last years as an alternative bactericidal method to fight against infectious diseases caused by bacteria (1, 2). Kuo *et al.* demonstrated for example the suppression of antibiotic resistant *Staphylococcus aureus* (*S. aureus*) bacteria with toluidine blue modified gold nanorods using a combination of photothermal (PTT) and photodynamic therapy (PDT) (3). While PDT is a promising method to destroy bacteria, gold nanostructures based PDT without PTT in parallel has surprisingly not been investigated so far. PDT requires the using of photosensitizer molecules (such as indocyanine green, methylene blue, porphyrins, chlorine e6 conjunctions, etc), which are inoffensive in the lack of light, in order to cause damage on irradiation at a particular wavelenghts. The resulting photo-toxicity is mainly due to the forming of reactive oxygen species (ROS), remarkable singlet oxygen, generated by electron transfer from the excited state of the sensitizer to molecular oxygen. Key parameters for the choice of the appropriate photosensitizer are, photothermal stability, cytotoxicity in absence of light, high <sup>1</sup>O<sub>2</sub> quantum yield as well as optical characteristics (4). The spectral mismatch between the spectrum of absorption of the photosensitizer and the optimum wavelenghts for tissue penetration (700-950 nm), (5) is now hindering the more spread using of PDT for medical purposes so far. The unique way for improving of the clinical efficiency of PDT is the developing and using of near-infrared (NIR) absorbing photosensitizers (6, 7).

Another approach could be to enhance the photosensitizers exciting field using field enhancement by metallic nanoparticles (8) along with the use of pulsed lasers (9). NIR two-photon activation is really attractive thanks to its deep penetration into a tissue and 3D-spatiotemporal preciseness, which are critical for place-specific therapy that leaves the circumscribing tissues undamaged (10-12). Since TP absorption cross-sections are very little, the restraining factor for effective NIR TD-PDT has been the presence of appropriate photosensitizers with suitable high two-photon cross section, with restrained photo-induced devaluation. Collins conducted experiences on a sequence of porphyrine dimers for the TP-PDT effectiveness (13). The using of photosensitizer verteporfin (VP), which was approved clinically, proved to be seven times more effective than photofrin, because of its higher TP cross-section is an attractive alternate (14).

Similar to VP, golden nanorods (Au NRs) manifest high TP absorption cross-sections. Their magnitude is almost two times higher than that of ordinary organic fluorophores (15-17). They are perfect nanostructures for the photodynamic killing of pathogenic microbes thanks to their chemical inertness, smooth of surface modification, tunable biocompatibility and large-scale preparation capability. In addition, if located surface plasmon resonance (LSPR) bands of golden nanorods are resonated with the absorption band of photosensitizers, the coefficient of absorption of the photosensitizer is largely enhanced by the immediate electric field they generate (18, 19).

In this chapter, the development of silica-coated golden nanorods (Au NRs@SiO<sub>2</sub>) modified with VP as effective nanostructures for NIR PDT is shown. The eradication of a virulent strain of *E. coli* via PDT using a continuous wave laser (activation of one-photon) and a pulsed-two photon laser TP-PDT will be investigated and compared.

## **4.2. Synthesis and photodynamic properties of Au NRs@SiO<sub>2</sub>VP**

The Au NRs@SiO<sub>2</sub>-VP particles was achieved in three steps (**Figure 4.1**). Firstly, the synthesis of Au NRs was conducted in accordance to a surfactant-assisted and seed-mediated procedure, which was adapted from the works of Murphy and El-Sayed (20) and their co-authors (21),

followed by their covering with a silica coat, which was based on the tetraethoxysilane hydrolysis under primary conditions (22).

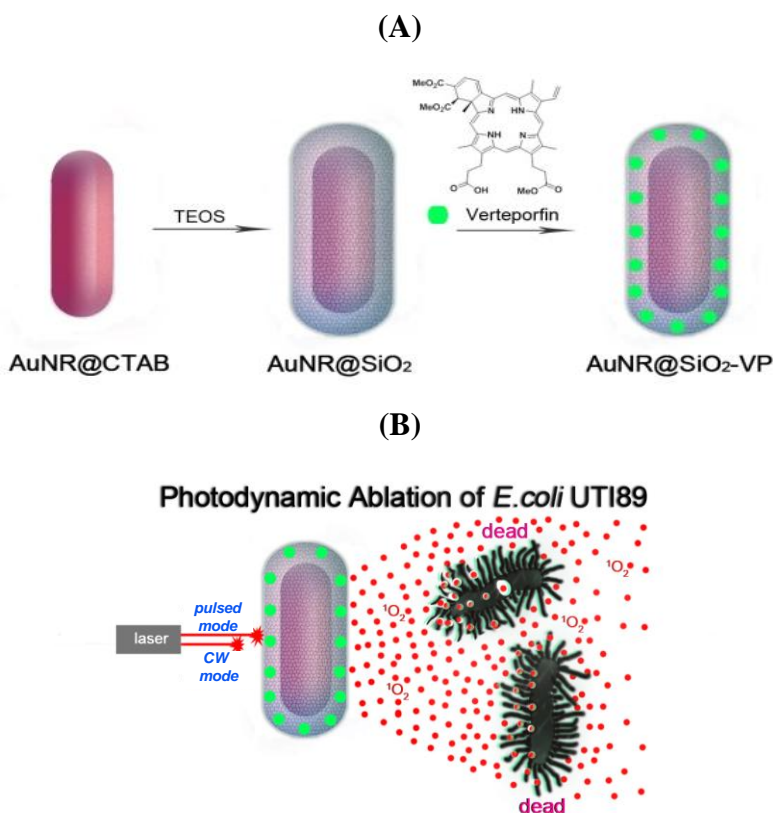


**Figure 4.1:** Illustration of the formation of Au NRs @SiO<sub>2</sub>-VP (A) and their use for the inactivation of *E. coli* UTI89 using PDT with a CW of pulsed-mode laser (B).

**Figure 4.2A** shows the SEM depiction of the created Au NRs@SiO<sub>2</sub>. The density of the silica stratum was estimated as 20±3nm. The approximate aspect ratio (length/diameter) of Au NRs was 3.5±0.3 nm, its resulted lengthwise LSPR maximum at 700 nm (**Figure 4.2B**). The availability of an additional cross vibration band at 512 nm proves the forming of prolonged Au NRs. Upon silica coat integration, a red shift of the lengthwise plasmon band is noticed (**Figure**

**4.2B)** in accordance with information in the literature (23). The SiO<sub>2</sub> covering has a significant impact on the zeta-potential of Au NRs@SiO<sub>2</sub>. Thanks to the availability of CTAB, the surface load of the Au NRs opened a zeta-potential of  $\approx 25\pm 2$  mV, at the same time Au NRs@SiO<sub>2</sub> manifests a surface potential of  $-16\pm 2$  mV (**Table 1**). The stability of the Au NRs@SiO<sub>2</sub> under laser irradiation prevented the Au NRs from surface melting (**Figures 4.2C**). The chemical frame of verteporphin (VP) (**Figure 4.1**) with presented carboxyethyl and carboxylic groups eases non-covalent interrelation with the silica coat *via* hydrogen bonds and load interrelations.

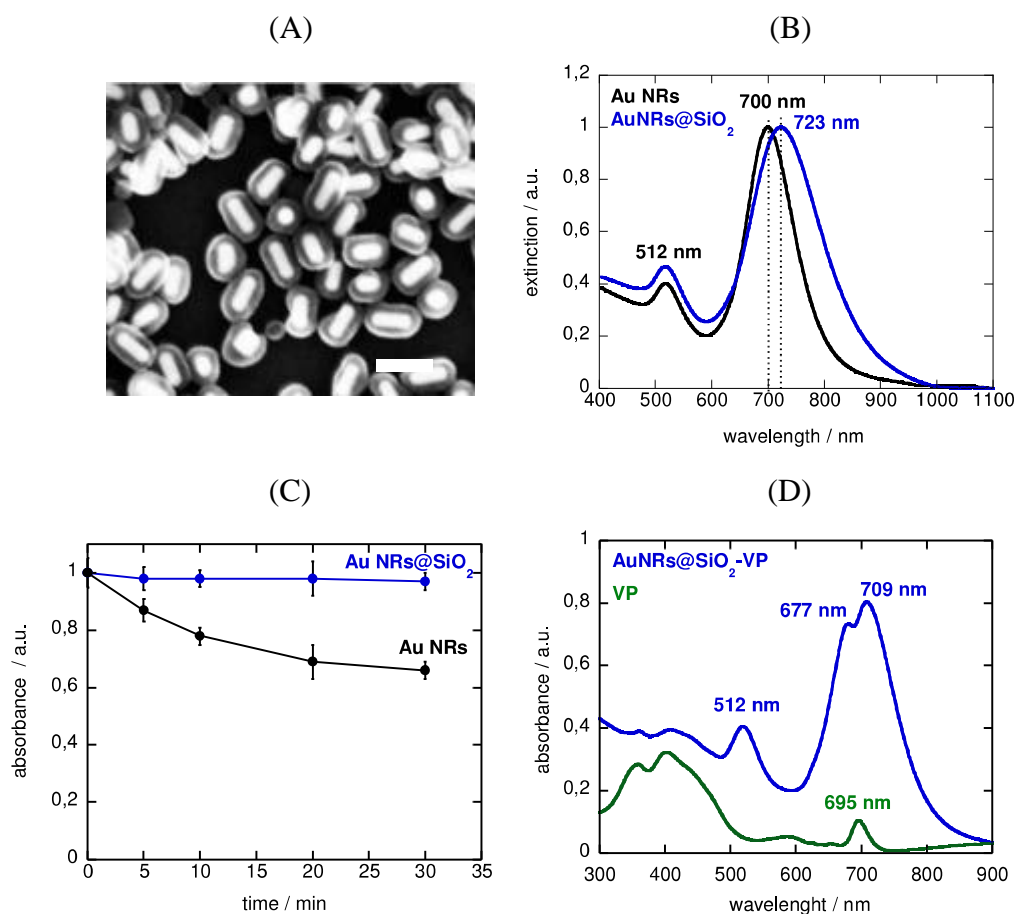


**Figure 4.2:** (A) SEM, scale 100 nm, and (B) (UV/Vis absorption spectra of CTAB-coated Au NRs and Au NRs@SiO<sub>2</sub> nanostructures; (C) Photostability of AuNRs (black) and Au NRs@SiO<sub>2</sub> (blue) solution upon irradiation at 710 nm (5 W) with a pulsed titanium: saphir laser (TP-laser; Chameleon model, Coherent); (D) UV/Vis of Au NRs@SiO<sub>2</sub> with embedded VP (4 μM) together with spectrum of VP (4 μM).

Intensive shaking of VP (20  $\mu\text{M}$ ) with AuNRs@SiO<sub>2</sub> in water/DMSO (2%) for 20 h arises 4  $\mu\text{M}$  of VP onto AuNRs@SiO<sub>2</sub>. The Au NRs@SiO<sub>2</sub> loading capacity for VP was assessed by the VP concentration measuring in this solution before and after loading onto Au NRs@SiO<sub>2</sub>. For this purpose, there were used spectrometric measurements UV/Vis at 695 nm, where VP manifests a featured absorption maximum (**Figure 4.2D**) (24). The potential of surface of the atoms remains negative ( $-14\pm 2$ ) (**Table 4.1**) that shows a deep union of VP with silica. This nanostructure was quite over 4 months at 4 °C AuNRs@SiO<sub>2</sub>-VP. The integration of VP onto AuNRs@SiO<sub>2</sub> is also confirmed by the availability of complementary bands between 350-500 nm and a harsh band at 677 nm near to the AuNRs@SiO<sub>2</sub> plasmon bands of (**Figure 4.2D**). In comparison with VP in watery solution, the absorption band of VP in AuNRs@SiO<sub>2</sub> is blue-shifted, since VP is most likely available as monomers (24, 25).

(A)			
Com.	VP	Au NRs@SiO <sub>2</sub> (700 nm)	Au NRs@SiO <sub>2</sub> -VP (700 nm)
$\Phi_x$	0.05 $\pm$ 0.01 (H <sub>2</sub> O) 0.41 $\pm$ 0.02 (MeOH)	0.10 $\pm$ 0.01	0.41 $\pm$ 0.02
$k, \text{min}^{-1}$	0.05 $\pm$ 0.01(H <sub>2</sub> O) 0.83 $\pm$ 0.02 (MeOH)	0.06 $\pm$ 0.01	1.15 $\pm$ 0.01

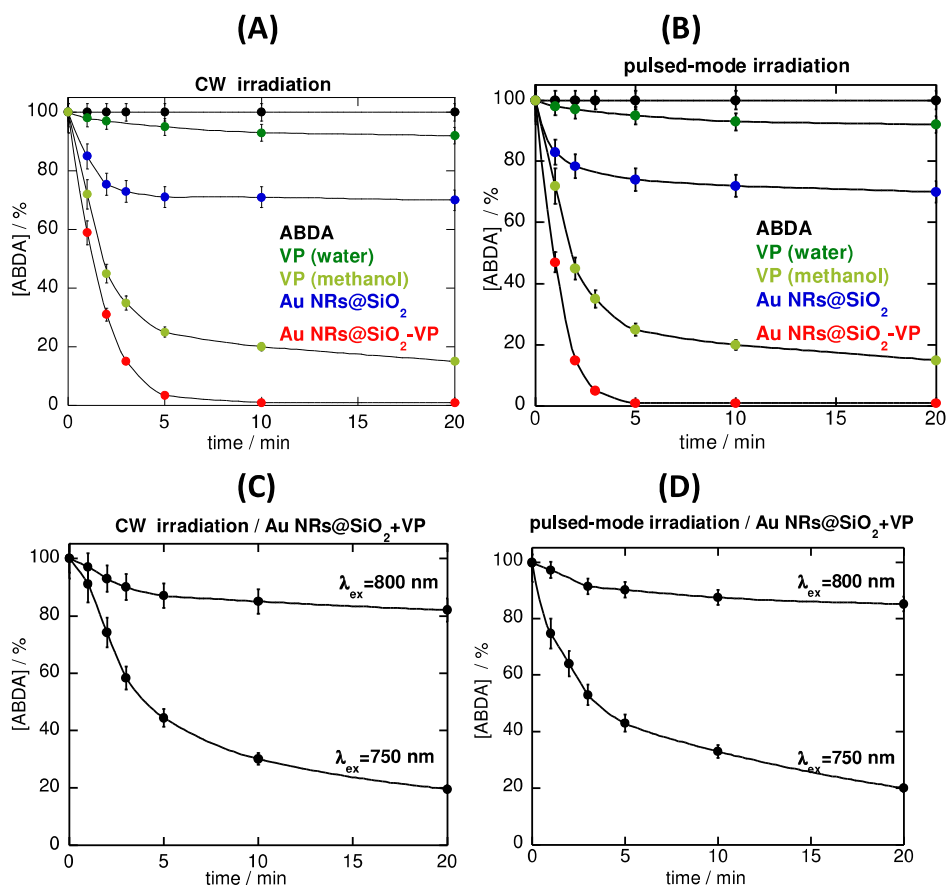
  

(B)				
Au NRs@SiO <sub>2</sub>	800 nm	+VP (800 nm)	900 nm	+VP (900 nm)
$\Phi_x$	0.10 $\pm$ 0.01	0.46 $\pm$ 0.06	0.11 $\pm$ 0.01	0.55 $\pm$ 0.10
$k, \text{min}^{-1}$	0.11 $\pm$ 0.01	1.10 $\pm$ 0.01	0.06 $\pm$ 0.01	0.92 $\pm$ 0.05

**Table 4.1:** Quantum yields of <sup>1</sup>O<sub>2</sub> and pseudo-first-order kinetic parameters determined under pulsed-laser light illumination at 710 nm for (A) VP (4  $\mu\text{M}$  in water and methanol), AuNRs@SiO<sub>2</sub> (230 pM) and AuNRs@SiO<sub>2</sub> -VP (230 pM + 4 $\mu\text{M}$ ) with a longitudinal plasmon band at  $\approx$ 700 nm; (B) AuNRs@SiO<sub>2</sub> (230 pM) and AuNRs@SiO<sub>2</sub>-VP (230 pM + 4 $\mu\text{M}$ ) with longitudinal plasmon bands at  $\approx$ 800 nm and 900 nm respectively under light illumination at 710 nm.

In order to evaluate the energy transmitting of Au NRs@SiO<sub>2</sub>-VP atoms to near oxygen molecules, they observed the photochemical decomposition of 9,10-anthracenediylbis(methylene) dimalonic acid (ABDA) (26). **Figure 4.3** depicts the reducing in optical absorption at 378 nm of

an ABDA solution, which contains Au NRs@SiO<sub>2</sub>-VP, as an operation of irradiation time under pulsed (**Figure 4.3A**) and CW lasers (**Figure 4.3B**), with Au NRs@SiO<sub>2</sub> and VP (4 μM) serving as controls. Independently of the using of the laser, Au NRs@SiO<sub>2</sub>-VP nanostructures manifested a rapid devaluation of ABDA that reflects effective singlet production of oxygen in both conditions. This confirms that it is possible to use these structures for NIR TP-excitation without restraining, taking benefits from the highly localized nature of TP experiments (10-12).



**Figure 4.3:** Photo-induced degradation of ABDA (10 μM) under irradiation over 20 min at 710 nm and laser power of 0.5 W cm<sup>-2</sup> in absence and presence of VP (4 μM in water), VP (4 μM in methanol), Au NRs@SiO<sub>2</sub> (230 pM, water) and Au NRs@SiO<sub>2</sub>-VP (230 pM+4 μM, water) under continuous wave (A) and pulsed-mode (B) irradiation; (C) Photo-induced degradation of ABDA (10 μM) under irradiation over 20 min at 750 nm and 800 nm with a laser power of 0.5 W cm<sup>-2</sup> in absence and presence of VP (4 μM), Au NRs@SiO<sub>2</sub> (230 pM) and Au NRs@SiO<sub>2</sub>-VP (230 pM +4 μM) under one (C) and two-photon (D) excitation.

It is interesting that Au NRs@SiO<sub>2</sub> manifested a stronger effect than free VP solution in water, which indicates that the nanostructure itself acts as a source of energy for PDT thanks to its plasmonic feature. The high effectiveness of Au NRs@SiO<sub>2</sub>-VP in comparison with the same concentration of VP in the solution, is assumed to be thanks to the plasmonic band of the nanostructures and the synergetic effects between the VP absorption band as it has been reported by Kuo et al (27).

In order to determine the Au NRs@SiO<sub>2</sub> and VP nanostructures potential for their using as antibacterial photodynamic probes, the Au NRs@SiO<sub>2</sub>-VP bactericidal character under NIR illumination with using of pulsed and CW lasers has been characterized. Recurring irradiation on Au NRs@SiO<sub>2</sub>-VP treated *E. coli* strains with a pulsed and CW lasers at 710 nm (1 W/cm<sup>-2</sup>) showed that Au NRs@SiO<sub>2</sub> as well as VP of 4 μM do not inactivate *E. coli* UTI89, at the same time as infection dose of 10<sup>4</sup> cfu mL<sup>-1</sup> *E. coli* is extirpated by means of Au NRs@SiO<sub>2</sub>-VP in a manner, which was dependent on time. The solution temperature did not increase above 37 °C during the entire experiment, excluding any photothermal associated eradications (28).

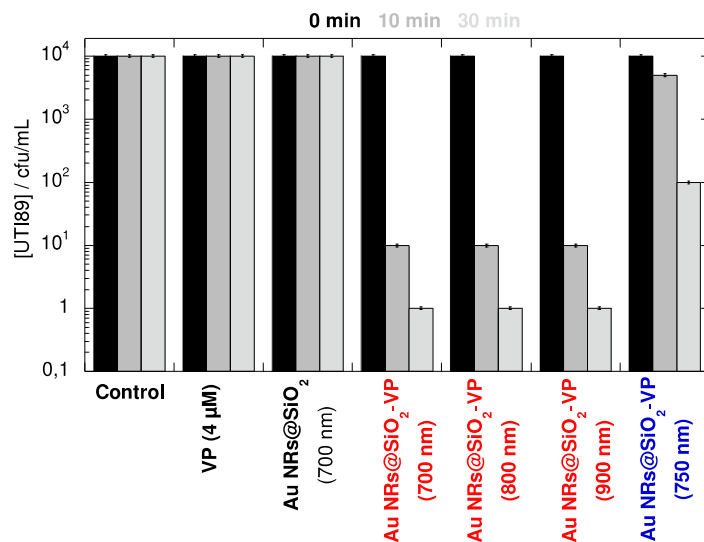


**Figure 4.4:** Treatment of *E. coli* UTI89 (10<sup>4</sup> cfu/mL) with VP (4 μM) and different Au NRs@SiO<sub>2</sub>-VP (230 μM) nanostructures under pulsed-laser irradiation at 710 nm and 1 W cm<sup>-2</sup>.

It has been noticed that 1-photon excitation is also able to contribute to the phototoxicity, which is observed in TP-PDT, thanks to the tail of the 1-photon absorption spectrum with long wavelengths (29). In order to understand whether this is the case for the TP-therapy of the pathogenic organisms (**Figure 4.4**), the energy dependency on the microbial viability was evaluated (30). Plotting the time of irradiation, which is necessary in order to deactivate 50% of pathogenic organisms ( $t_{50}$ ), vs. the laser power ( $P^{-1}$ ) indicates a direct behavior with a direct regression of  $2.19 \pm 0.19$ , which confirms preliminary a behavior of TP (**Figure 4.4**). TP-PDT of microbial contagions would therefore overcome some of the common shortcomings of 1-photon therapy such as injury of over and underlying tissues, which are neighboring to the treated zone.

### 4.3. Conclusions

This chapter describes the development of new nanostructures for NIR two-photon photodynamic treatment that comprises of silica-encased golden nanorods, which have been modified with verteporfin, which serves as photosensitizer. The Au NRs structures were adjusted to be resonated with the maximum of verteporfin absorption. It has been able to be shown that not only the Au NRs@SiO<sub>2</sub>-VP were photothermally firm during a long period of time, but that they resulted in a great amount of reactive oxygen species by irradiation at 700 nm at 500 mW cm<sup>-2</sup> with using a persistent or a pulsed laser sources. The nanostructures potential for the eradication of pathogenic organisms was demonstrated, depending on the wavelengths. The method of such approach may be considered as one of the alternate strategies for destroying of wound-infection antibiotic resistance.

### 4.4. References

1. Givens Bell S. Antibiotic resistance: is the end of an era near? Neonatal Network. 2003; 22(6):47-54.
2. Petty NK, Zakour NLB, Stanton-Cook M, Skippington E, Totsika M, Forde BM, et al. Global dissemination of a multidrug resistant Escherichia coli clone. Proceedings of the National Academy of Sciences. 2014; 111(15):5694-9.

3. Kuo W-S, Chang C-N, Chang Y-T, Yeh C-S. Antimicrobial gold nanorods with dual-modality photodynamic inactivation and hyperthermia. *Chemical Communications*. 2009 (32):4853-5.
4. Khurana M, Ulrich S, Kim A, Moriyama Y, Netchex G, Akens MK, et al. Biodistribution and pharmacokinetic studies of a porphyrin dimer photosensitizer (Oxdime) by fluorescence imaging and spectroscopy in mice bearing xenograft tumors. *Photochem Photobiol*. 2012; 88:1531-8.
5. Eichler J, Knof J, Lenz H. *Radiat Environ Biophys*. 1977; 14:239-42.
6. George S, Hamblin MR, Kishen A, 8, 788. Uptake pathways of anionic and cationic photosensitizers into bacteria. *Photochem Photobiol Sci* 20029; 8:788.
7. Topaloglu N, Gulsoy M, Yuksel S. Antimicrobial photodynamic therapy of resistant bacterial strains by indocyanine green and 809-nm diode laser. *Photomed Laser Surgery*. 2013; 31:155-62.
8. Stockman MI. *Opt Expr*. 2011; 19:22029.
9. Pawlicki M, Collins HA, Denning RG, Anderson HL. Two-photon absorption and the design of two-photon dyes. *Angew Chem Int Ed* 2009; 48:3244.
10. Gary-Bobo M, Mir Y, Rouxel C, Brevet D, Basile I, Maynadier M, et al. *Angew Chem, Int Ed*. 2011;123:11627–31.
11. Croissant JG, Mongin O, Hugues V, Blanchard-Desce M, Cattoën X, Man MWC, et al. Influence of the synthetic method on the properties of two-photon-sensitive mesoporous silica nanoparticles. *J Mater Chem B*. 2015; 3:5182-8.
12. Wang S, Huang P, Nie L, Xing R, Liu D, Wang Z, et al. *Adv Mater*. 2013; 25:3055-61.
13. Collins HA, Khurana M, Moriyama Y, Mariaùpillai A, Dahlstedt E, Balaz M, et al. *Nat Photonics* 2008(2):420.
14. Khurana M, Collins HA, Karotki A, Anderson HL, Cramb DT, Wilson BC. *Photochem Photobiol*. 2007; 83:1441.
15. T. W, D. H, D. H, Feldman M, Milner TE. *Biomed Opt Expr*. 2013;4:584.
16. Zijlstra P, Chon JWM, Gu M. *Nature*. 2009; 459:410.

17. Wang H, Huff TB, Zweifel DA, He W, Low PS, Wei A, et al. Proc Natl Acad Sci USA 2005; 102:15752.
18. Chu Z, Yin C, Zhang S, Lin G, Li Q. Surface plasmon enhanced drug efficacy using core-shell Au@SiO<sub>2</sub> nanoparticle carrier. Nanoscale. 2013; 5:3406-11.
19. Jang B, Choi Y. Photosensitizer-Conjugated Gold Nanorods for Enzyme-Activatable Fluorescence Imaging and Photodynamic Therapy. Theranostics. 2012; 2:190.
20. Nikoobakht B, El-Sayed MA. Preparation and growth mechanism of gold nanorods (NRs) using seed-mediated growth method. Chem Mater. 2003; 15:1957-62.
21. Gou L, Murphy CJ. Chem Mater. 2005; 17: 3668.
22. Gorelikov I, Matsuura N. Single-Step Coating of Mesoporous Silica on Cetyltrimethyl Ammonium Bromide-Capped Nanoparticles. Nano Lett. 2008; 8:369.
23. Seo S-H, Kim B-M, Joe A, Han H-W, Chen X, Cheng Z. NIR-light-induced surface-enhanced Raman scattering for detection and photothermal/photodynamic therapy of cancer cells using methylene blue-embedded gold nanorod@SiO<sub>2</sub> nanocomposites. Biomaterials. 2014; 35:3309-18.
24. Aveline B, Hasan T, Redmond RW. Photochem Photobiol. 1994; 59:328.
25. Samkoe KS, Cramb DT. J Biomed Optics. 2003; 8:410-7.
26. Zhao T, Shen X, Lin L, Guan Z, Gao N, Yuan P, et al. Nanoscale. 2012; 4:7712.
27. Kuo W-S, Chang C-N, Chang Y-T, Yang M-H, Chien Y-H, Chen S-J, et al. Gold nanorods in photodynamic therapy, as hyperthermia agents, and in near-infrared optical imaging. Angew Chem Int Ed. 2010; 49(15):2711-5(15):2711-5.
28. Turcheniuk K, Hage C-H, Spadavecchia J, Yanguas Serrano A, Larroulet AP, I. , Zurutuza A, et al. Plasmonic photothermal destruction of uropathogenic *E. coli* with reduced graphene oxide and core/shell nanocomposites of gold nanorods/reduced graphene oxide. J Mater Chem B. 2015; 3:375-86.
29. Karotki A, Khurana M, Lepock JR, Wilson BC. Photochem Photobiol. 2006; 82:443.
30. Luo T, Wilson BC, Lu Q-B. J Photochem Photobiol B 2014; 132:102.

## CHAPTER V

### **Photothermal cancer therapy with gold nanorods/reduced graphene oxide core/shell nanocomposites**

#### **5.1. Introduction**

Although chemotherapy and surgery still remain the basic medicinal approaches for the therapy against many types of cancer, nanoparticles-based anticancer treatments have been largely developed during the recent years as an efficient therapy of cancers at advanced-stage (1, 2). One significant drawback by using therapies, which are based on drugs, particularly when they are taken intravenously or orally, is that the combination does not localize to a target place. This non-specific conveyance of chemotherapeutic matters brings regular side effects to healthy tissues and restrains efficiency in the tumor deactivation. Targeted cancer treatment, which is based on nanostructures, has been developed in order to get higher levels of accuracy by certain concentration of the medicinal nanostructure in the cancer tumor more than in the healthy tissue. Golden nanostructures are certainly the most appropriate among the all nanoparticles, which are considered for cancer now (3, 4). The localized surface plasmon golden nanoparticles resonance (5) (LSPR) gives them the capability to strongly consume light at a specific wavelengths, which is able to be managed and adjusted by synthetic tools. Photo-excitation of golden nanostructures at their LSPR band can effectively turn energy of photon into heat and may be used for the photothermal removing of cancer cells. In contrast to spherical nanoparticles, which consume light in the visible area (6, 7), golden nanorods (Au NRs) move the excitation wavelengths to the near-infrared are (NIR) (8). The flexibility of adjusting of the lengthwise plasmon band to the

NIR makes it attractive for biomedical identification *in vivo* and treatment, since light in the NIR area is able to deeply penetrate into matter without large absorption and warmth generation. Au NRs are there for great promising in photothermal treatment (PTT) of different cancers and other illnesses (7, 9, 10). From the view of cancer treatment, low laser energies are important ( $\leq 1 \text{ W cm}^{-2}$ ) in order to provide minimum side effects such as burning of skin. Many researchers reported that the laser intensiveness exceeded  $1 \text{ W cm}^{-2}$ , (11-13) and only in last years, more attention has been given to this characteristic (14-16). Photodynamic and bimodal PTT cancer therapies are only way in order to cope with this restriction. The development of new golden nanostructures and hybrids with a more effective light-to-heat transition is another variant (15, 16). The including and wrapping of golden nanostructures in graphene oxide (GO) and decreased graphene oxide (rGO) would be able to be a step towards this direction (17). Kohane with his co-workers proved that rGO covered golden nanoparticles deactivate cells faster under 808 nm irradiation with an intensity of laser of  $3 \text{ W cm}^{-2}$ , than uncovered particles do. The photothermal medicinal reaction of cancer cells to aptamer-modified golden nanoparticles, which were included in GO, has shown to ease targeted photothermal therapy in the NIR at  $2 \text{ W cm}^{-2}$ . Recently, there was demonstrated by us the interest of rGO wrapped Au NRs for the photothermal removing of microbes (18).

This thesis chapter reports that Au NRs, which is covered with pegylated rGO (Au NRs@rGO-PEG), are perfect multi-functional therapeutic nanostructures, which are able to exert effective photothermal deactivation of tumors in mice on NIR light excitation and are able to operate as fluorescent markers of cells. Because of the specific interrelation between Au NRs@rGO-PEG nanostructures, which are modified with Tat protein vectors towards the direction of cells of human glioblastoma astrocytoma (U87MG), targeting of the tumor is got. We think that these nanomaterials are able to reveal new perspectives in cancer therapies thanks to the highly local and nontoxic method.

## **5.2. Synthesis and physicochemical properties of AuNrs@rGO particles**

Synthesis of golden nanorods, which are covered with reduced pegylated graphene oxide (Au NRs@rGO-PEG), **Figure 5.1** schematically depicts the strategy of preparation, which is used for

wrapping of Au NRs with rGO-COOH, and the union of a NIR fluorescent marker with the tumor targeting Tat vector together. CTAB made Au NRs to be steady with lightwise surface plasmon centered approximately at ~800 nm were synthesized as has been shown in the previous research (18). Since the surface charge of CTAB-stabilized Au NRs is positive with a zeta potential of  $+40\pm 2$  mV, intensive electrostatic interrelation with negatively charged rGO-COOH ( $\zeta = -45\pm 2$  mV) happens (**Table 5.1**).

**Table 5.1:** Zeta-potential of different nanostructures investigated in this work

	Au NRs	rGO-COOH	Au NRs@rGO-COOH	Au NRs@rGO-PEG	Au NRs@rGO-PEG-Cy7	Au NRs@rGO-PEG-Tat/Cy7
$\zeta$ /mV	$+40 \pm 2$	$-45 \pm 2$	$-35 \pm 2$	$-16 \pm 2$	$-10 \pm 2$	$+15 \pm 2$

Well identified Au NRs-rGO-COOH were formed, in comparison with those, which were investigated by Kohane and his co-workers (17). A demonstrative SEM depiction indicates the successful forming of a rGO-COOH stratum around the Au NRs (**Figure 5.1B**).

The availability of rGO-COOH covering around the Au NRs was later proved with spectra of UV/Vis absorption (**Figure 5.1C**). In comparison with GO, which displays a maximum of optical absorption at 230 nm, the Au NRs@rGO-COOH nanostructures reveal a red shifted band at 269 nm that shows the restructuring of the state of electronic transition ( $\pi$ - $\pi^*$ ) in rGO-COOH. The growth of intensiveness of the NIR absorption tail is an additional indicator of the availability of rGO-COOH.

The approximate Au NRs aspect ratio (length/diameter) was  $3.8\pm 0.3$  (**Figure 5.1B**) that results in a lengthwise LSPR maximum at approximately 807 nm (**Figure 5.1C**). The availability of an additional cross vibration band at 511 nm proved the forming of prolonged Au NRs. In the variant of Au NRs@rGO-COOH the lengthwise band moved to 814 nm, at the same time the cross band remained at approximately 511 nm (**Figure 1C**).

The XPS examination spectrum of Au NRs@rGO-COOH shows bands in accordance to  $O_{1s}$  (30.9 at %),  $Au_{4f}$  (2.3 at %),  $C_{1s}$  (66.8 at %), according to its chemical structure (**Figure 5.2A**).

The  $C_{1s}$  XPS spectrum of high resolution (**Figure 5.2B**) displays four bands, at 284.5 eV ( $sp^2$  network), 287.9 eV (C=O), 286.5 eV (C-O) and 291.3 eV is explained by carbon species of higher states of oxidation, for example, carboxylic acid. The  $Au_{4f}$  XPS spectrum high resolution shows two maximal values thanks to  $4f_{5/2}$  and  $4f_{7/2}$  at 84.0, and 87.6 eV, respectively (**Figure 5.2C**). The restricting powers recorded are compatible with zerovalent Au (18). Analysis of Raman of Au NRs@rGO-COOH displays a band at  $\approx 1590\text{ cm}^{-1}$ , which is close to the pristine graphite band that assumes reduction of GO to rGO in this process (**Figure 5.2D**). The presence of a D band at  $\approx 1362\text{ cm}^{-1}$  shows the presence of flaws in the in-plane  $sp^2$  domain of the species.

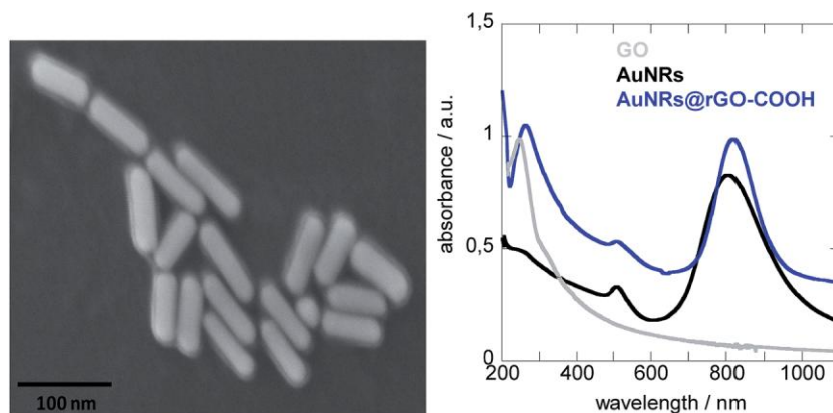
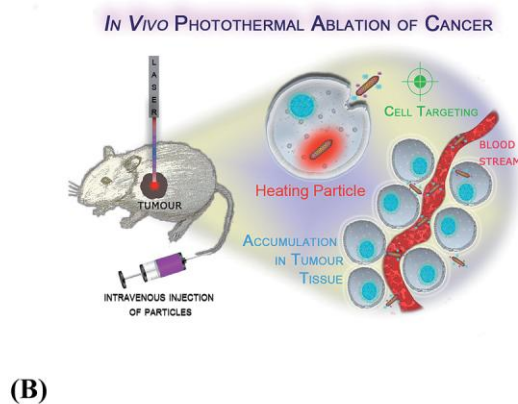
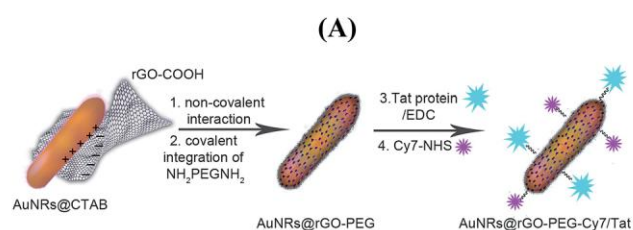


**Figure 5.1:** Synthesis of Au NRs@rGO-PEG-Tat/Cy7 for hyperthermic treatment of tumors. (A) Illustration of the preparation of pegylated fluorescently labeled, Tat-protein modified Au NRs@rGO-PEG-Tat/Cy7; (B) SEM image of Au NRs@rGO-COOH; (C) UV-Vis absorption spectra of GO (grey), Au NRs (black) and Au NRs@rGO-COOH (blue).

The ratio intensiveness ( $I_D/I_G$ ) of 0.69 proves the incomplete decreasing of GO to rGO (19). The 2D band, which is located at  $2694\text{ cm}^{-1}$  with an extra shoulder to a higher length of waves, assumes also ascendant multi-stratum structure. The colloidal firmness of particles of Au NRs@rGO-COOH in PBS (pH 7.4) was although probably restricted because of the rGO hydrophobicity(20) and the nanostructures, which was sediment during several days at temperature of room (**Figure 5.2E**).

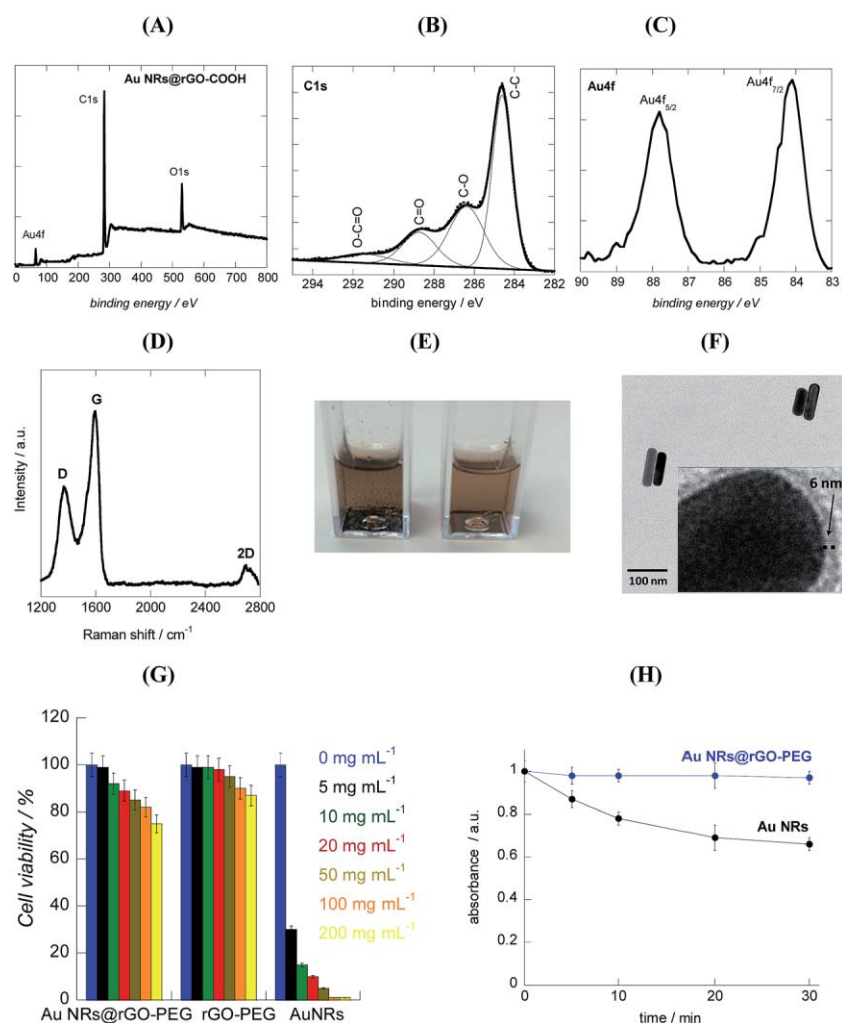


**Figure 5.2.** (A) XPS survey spectrum of Au NRs@rGO-COOH, (B) C<sub>1s</sub>, and (C) Au<sub>4f</sub> high resolution spectra of Au NRs@rGO-COOH; (D) Raman spectrum of Au NRs@rGO-COOH; (E) dispersibility in PBS of Au NRs@rGO-COOH (left) and Au NRs@rGO-PEG (right); (F) TEM image of Au NRs@rGO-PEG; (G) cell viability of U87MG glioblastoma cells upon incubation with different concentrations of Au NRs, rGO-PEG and Au NRs@rGO-PEG; (H) photostability of Au NRs (black) and Au NRs@rGO-PEG (blue) solution upon irradiation at 808 nm (CW, 1 W cm<sup>2</sup>).

In order to raise the Au NRs@rGO-COOH dispersibility, amino-free PEG (NH<sub>2</sub>-PEG-NH<sub>2</sub>) units were joint covalently to the carboxylic acid groups of rGO-COOH with the help amide bond

creation (18, 21, 22). Upon conjunction the obtained Au NRs@rGO-PEG displayed higher solvability and firmness in PBS (**Figure 5.2E**), which are crucial for biological applications. A watery Au NRs@rGO-PEG substance was stable for approximately 2 months at 4 °C without any visible aggregation. The TEM Au NRs@rGO-PEG depiction (**Figure 5.2F**) displays the availability of an approximately 6 nm covering about the particles.

For this thesis, we have chosen cells of human glioblastoma astrocytoma (U87MG) as the sample for the experiment. Experiments on vitality of cells were carried out through incubating of the cells of cancer with Au NRs@rGO-PEG in the dark environment for 48 h. As **Figure 5.2G** shows, the nanomaterial manifests good biocompatibility, which was assessed via MTS analyses up to a particle concentration of 100 mg mL<sup>-1</sup>.

One problem with using of Au NRs for PTT is their infirmness/dissolving under NIR that results in reduced absorbance after a particular time period of irradiation of a laser (23, 24). It has been revealed that in comparison to Au NRs, Au NRs@rGO-PEG turned out to be firm extremely under persistent 808 nm irradiation without any visible change in optical density (**Figure 5.2H**).

### **5.3 Photothermal features of Au NRs@rGO-PEG and photothermal eradication cells of U87MG *in vitro*.**

Because of the strong assimilation of Au NRs@rGO-PEG in the NIR area, the photothermal nanostructures effectiveness was researched and compared with rGO-PEG and Au NRsd. **Figure 5.3A** conducts a comparison of the scale of the water temperature growth in the availability of the various nanostructures. Upon irradiation, which uses a 808 nm NIR laser at a power density of approximately 0.5 W cm<sup>-2</sup>, the temperature of the substance rose to approximately 60 °C during 10 minutes in the availability of Au NRs@rGO-PEG (20 µg mL<sup>-1</sup>).

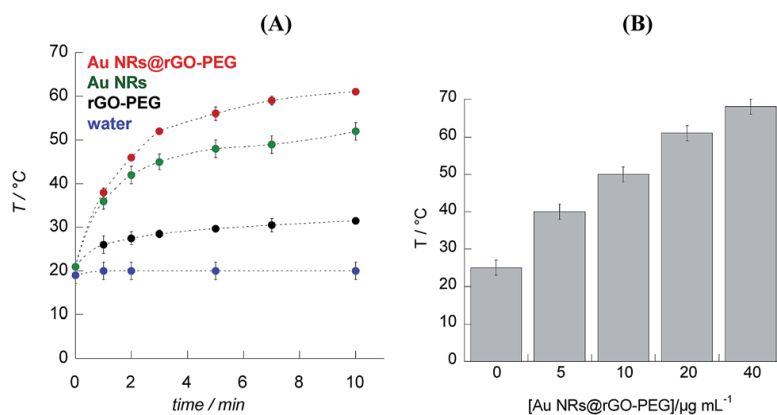


**Figure 5.3:** (A) Photothermal heating curves of different nanostructures dissolved in distilled water ( $20 \text{ mg mL}^{-1}$ ) under NIR illumination (800 nm) at  $0.5 \text{ W cm}^{-2}$  for 10 min using a CW laser: water (blue), rGO-PEG (black), Au NRs (green), Au NRs@rGO-PEG (red); (B) change in temperature as a function of Au NRs@rGO-PEG concentration during illumination at 808 nm for 10 min at  $0.5 \text{ W cm}^{-2}$ .

The temperature graphs of Au NRs and rGO-PEG at almost equal concentrations displayed the similar tendencies, but with less elevations of the temperature. Unlike direct water irradiation, which does not display any apparent growth upon laser irradiation. rGO conjunction with Au NRs leads to a synergistic effect and improve the general temperature growth, according to previous researches. As it was expected, the temperature growth of Au NRs@rGO-PEG substances depends on concentration and may be adjusted by using the relevant range of concentration (**Figure 5.3B**). At an concentration approximately  $5 \text{ } \mu\text{g mL}^{-1}$ , NIR irradiation made a temperature growth up to  $\approx 40 \text{ } ^\circ\text{C}$ , which is suggested to be quite high for photothermal removing of cancer cells (25).

In order to investigate further the Au NRs@rGO-PEG ability for cancer treatment, the photothermal removing of cells of human glioblastoma astrocytoma (U87MG) was carried out. For particular aiming, Tat peptides, which are known for their target ability towards cells of U87MG by final arginine that bears a positive charge, were joint to the nanomaterials in order to promote nanomaterial targeting towards the cell (26). Tat conjunction was obtained through

amide bond forming as was observed for other proteins (27, 28). The volume of Tat protein joint was defined by UV-Vis spectroscopy as 20  $\mu\text{g}$  per 100  $\mu\text{g mL}^{-1}$  of Au NRs@rGO-PEG. The change to a positive zeta potential (**Table 5.1**) from  $-10\pm 2$  to  $+15 \pm 2$  mV shows also the successful integration of Tat protein.

The U87MG photodestruction, which was made with Au NRs@rGO-PEG and Au NRs@rGO-PEG-Tat, was performed by using a persistent wave laser at 808 nm during 10 minutes at a laser energy of  $1 \text{ W cm}^{-2}$  (**Figure 5.4A**). The cells were incubated during 4 h, rinsed, exposed to irradiation, then incubated during 48 h. Thereafter, examinations of a colorimetric MTS metabolic activity were performed in order to define the general cell viability. In the lack of irradiation, the cells of U87MG, which were exposed to Au NRs@rGO-PEG-Tat, do not show any essential cytotoxicity, independently of the accumulation used. The incubation of Au NRs@rGO-PEG with following laser irradiation (808 nm,  $1 \text{ W cm}^{-2}$ , 10 min) displayed an accumulation dependent reduction of cell vitality with almost all cells ( $\approx 97\%$ ) eradicated after irradiation of NIR ( $\text{EC}_{50} = 32 \mu\text{g mL}^{-1}$ ). With using of Tat-functionalized Au NRs@rGO-PEG, a lower  $\text{EC}_{50}$  was obtained ( $11 \mu\text{g mL}^{-1}$ ), proving beneficial effect of joint Tat vectors. It is possible to compare these results with those reported by Ghaderi and Akhavan for the removing of human glioblastoma cells with using of graphene nanomesh substances of  $10 \mu\text{g mL}^{-1}$  with NIR power density of  $0.1 \text{ W cm}^{-2}$  during 7 min (10).

Au NRs@rGO-PEG-Tat internalization into U87MG cells with high effectiveness is very significant for photothermal treatment. In order to prove the nanostructures uptake, a fluorescent dye (FITC) was further combined to AuNRs@rGO-PEG-Tat (19). After the incubating of the cells with  $50 \mu\text{g mL}^{-1}$  Au NRs@rGO-PEG-Tat/FITC during 1, 4 and 24 hours, confocal microscopic pictures were obtained and displayed in the exactly same conditions in order to facilitate visual comparison of uptake of fluorescently labeled nanoparticles (**Figure 5.4C**). The fluorescence intensiveness is increased essentially from 1 to 4 hours with a small drop at 24 h. At 4 h the highest distribution of Au NRs@rGO-PEG-Tat/FITC was seen over the whole cytoplasm. Non-vectorized nanomaterial showed, at the same time, the signal, which was much weaker. These researches assumed that the physico-chemical characteristics of Au NRs@rGO-PEG-

Tat/FITC impact significantly the uptake of nanoparticles by the cells of U87MG. Thorough analysis displayed the highest fluorescence signal in the perinuclear area, possibly some Golgi complex cisternae that assumes an endosome-related path of consuming of nanoparticles with following endosome recycling in Golgi (~10000 a.u.) (Figure 5.4B). The membrane edges were impregnated with the nanomaterial (~ 4000 a.u.) as well, visualized by two fluorescent peaks on the borders of cell. The high concentration of the photothermal substance in tumor cells is essential and will enable effective selective photothermal warming.

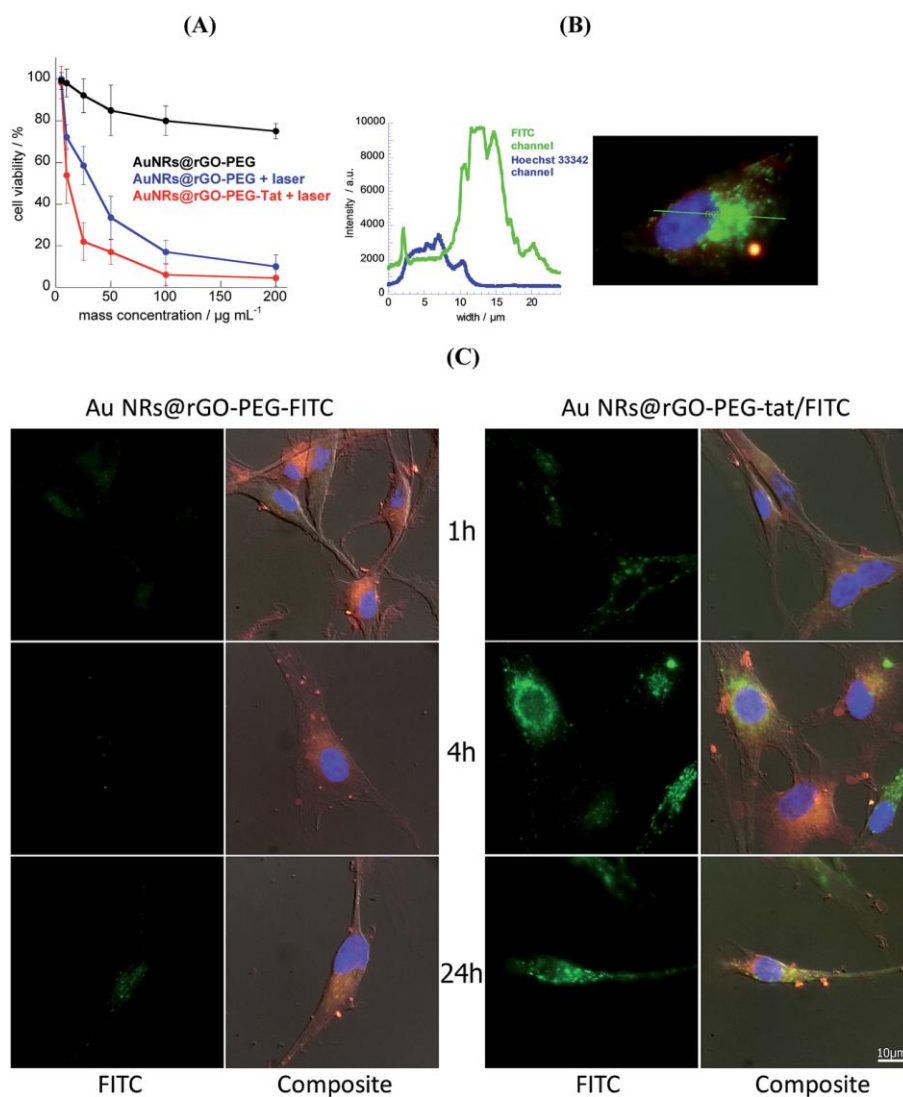


**Figure 5.4:** Cellular localization of functionalized Au NRs. (A) Photothermal U87MG cell

killing with Au NRs@rGO-PEG-Tat and Au NRs@rGO-PEG (detected by MTS assay, data are normalized to untreated cells) of U87MG cells as a function of nanomaterials concentration upon NIR illumination (CW, 808 nm) at  $1 \text{ W cm}^{-2}$  for 10 min; (B) fluorescence intensity profile from Au NRs@rGO-PEG-Tat/FITC along the indicated line across single U87MG cell. FITC fluorescence is present in the cell surface (small peaks corresponding to cell margins) and in the perinuclear region (center) but absent in the nucleus (counterstained by Hoechst 33342). (C) Fluorescence microscopy images of U87MG cells incubated with Au NRs@rGO-PEG/FITC and Au NRs@rGO-PEG-Tat/FITC for 1, 4 and 24 h. Merged images show Hoechst 33342 (blue), CellMask (red) and FITC (green). All images were acquired and represented in the exact same condition to ease visual comparison of fluorescently labeled nanoparticle's uptake.

#### 5.4. NIR fluorescence imaging and biodistribution

In order to enable tracking of the Au NRs@rGO-PEG-Tat nanohybrids *in vivo*, we performed labelling with Cy7-NHS, which is commercially available and is a generally used NIR dye (**Figure 5.1**). With analysis of the supernatant after this covalent coupling reaction with the help of absorption spectra ( $750 \text{ nm}$ ,  $199000 \text{ L Mol}^{-1} \text{ cm}^{-1}$ ), it was revealed that  $10 \mu\text{g mL}^{-1}$  of Cy7 was joined onto  $100 \mu\text{g mL}^{-1}$  Au NRs@ rGO-PEG-Tat.

As a proving research, we conducted experiments with mice *in vivo* in order to assess the efficiency of the nanostructures. In order to do this, Swiss nude mice with implanted cells of U87MG glioblastoma ( $5 \times 10^6$  cell/1 mouse) at the right side were treated by Au NRs@rGO-PEG-Tat/Cy7 at a dosage of  $150 \mu\text{L}$  of  $1 \text{ mg/mL}$  per 1 mouse ( $5 \text{ mg/kg}$ ) by intravenous injections into the tail veins (**Figure 5.5A**). The cells of the tumor were vaccinated in Matrigel<sup>TM</sup>, a polymer matrix, which becomes polymerized immediately after injection into the living organism that provides necessary matters in order to enable rapid growth of tumor (29). So, 18 days were necessary in order to obtain a tumor (of spheric shape) of approximately  $500 \text{ mm}^3$  in size (**Figure 5.6C**), evaluated to be most optimal for the therapy.

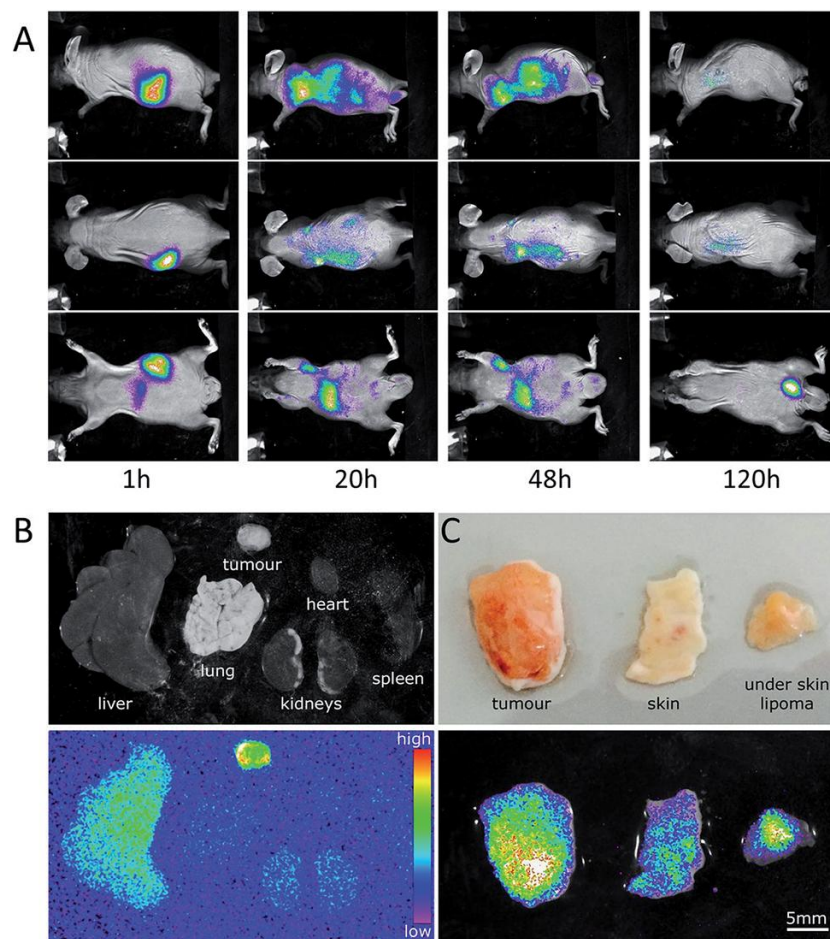


**Figure 5.5:** Biodistribution analysis of Au NRs@rGO-PEG-Tat/Cy7 nano- particles. (A) *In vivo* NIR fluorescence images (Cy7) demonstrating distribution in the body of intravenously injected Au NRs@rGO-PEG-Tat/Cy7 nanoparticles after 1, 20, 48 and 120 h of injection. (B) Accumulation of Au NRs@rGO-PEG-Tat/Cy7 in different organs 24 h after intravenous injection into the tail vein. (C) Distribution of Au NRs@rGO-PEG-Tat/Cy7 in solid tumor, surrounding lipoma tissue and skin, lipoma was located between skin and solid tumor. Fluorescence images taken 24 h post-injection.

Since the NIR fluorescence is able to penetrate deeply into the mouse tissue, the Au NRs@rGO-PEG-Tat/Cy7 fluorescence signal is able to be used in order to locate the particles and whether these nanostructures are vectorized to this tumor.

The NIR fluorescence pictures (Cy7 channel) *in vivo* from Au NRs@rGO- PEG-Tat/Cy7 were treating mice after 1, 20, 48 and 120 hours after injections (**Figure 5.5A**). It can be seen, that these nanostructures primarily concentrate in the right kidney, spleen and at the first 1 h, showing that some of the Au NRs@rGO-PEG-Tat/Cy7 structures are quickly identified by the reticuloendothelial system (RES) and the phagocytic cells. With the time progressing (20 hours after the injection), the signal in the spleen and liver reduces essentially, becoming hardly identified. On the contrary, the fluorescent signal of the nanostructures in the tumor area got much stronger, achieving its maximal value in 20 h after the injection. Then, the signal intensiveness decays as well over time with less intensiveness in 48 h after the injection. At 24 h after the injection, mice were euthanatized and their main organs were examined for the presence of ex vivo fluorescence (**Figure 5.5B**). Acquired data proved the highest fluorescence signal localization in the tumor area in comparison to other organs, namely kidneys and liver. The part of skin and lipoma tissue, which were between tumor and skin, were examined as well that has demonstrated the highest signal in tumor tissue, proving the aiming the nanomaterial localization (**Figure 5.5C**). It is obvious that the highest NIR fluorescence signal goes from the tumor tissues thanks to the long time of blood circulation and improved permeability and conservation effect (30). Analysis of mice excrements displayed signal that indicates that nanomaterial was removed from the body through intestine and bladder.

### **5.5. *In vivo* photothermal therapy of mice with implanted cells of U87MG tumors**

In order to evaluate the medicinal effect of Au NRs@rGO-PEG-Tat/Cy7 on the photothermal therapy of cancer tumors, an antitumor research *in vivo* was conducted with using the mice, which bear U87MG tumor, as animal model. After intravenous injections of 150  $\mu\text{g}$  of Au NRs@rGO-PEG-Tat/Cy7 per 1 mouse into tail veins and the concentration during 20 h of the nanostructures in the tumor, all mice were exposed to the irradiation of NIR laser, according to all the safety and ethical rules, which are necessary in using of a CW laser with 808 nm excitation, in which the optical fiber was located 6 cm above the tumor. Different intensiveness of laser power was tested in order to make the therapy optimal. Since  $2 \text{ W cm}^{-2}$  caused serious

burn of skin, the experience

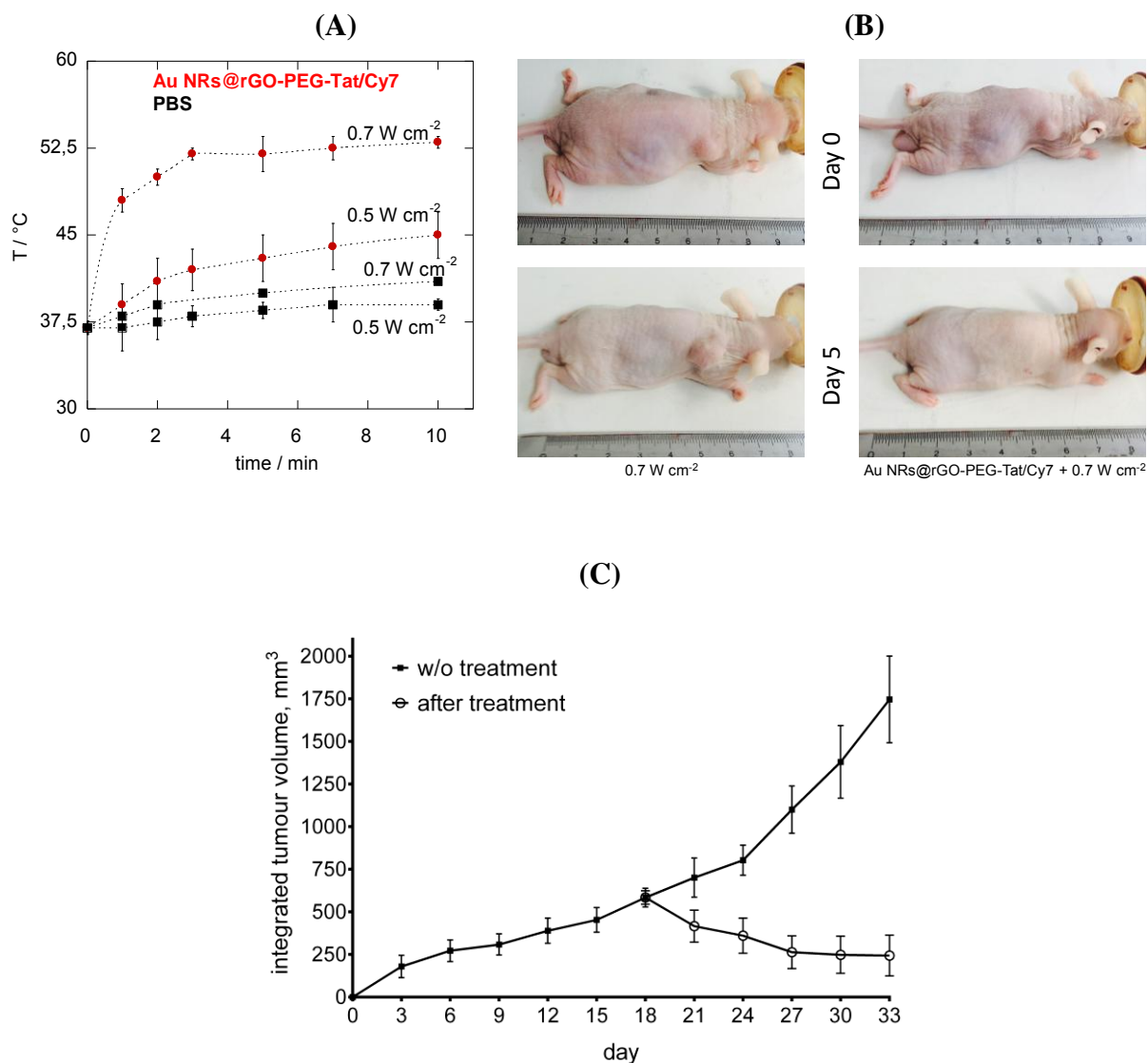


**Figure 5.6:** *In vivo* photothermal effect of Au NRs@rGO-PEG-Tat/Cy7 in mice. (A) Temperature profiles of the tumor region when exposed to different laser powers (0.5 and 0.7 W cm<sup>-2</sup>); (B) representative images of mice showing the size of the tumor as indicated by dashed circles at day 0 and 5 after photothermal treatment with and without injected Au NRs@rGOPEG-Tat-Cy7; (C) tumor growth curve in 2 mice groups – with and without photothermal treatment; integrated tumor volume of photothermally treated group significantly decreases 5 days post

treatment, while in the untreated group tumor volume dramatically increases with time.

was conducted using a laser power of  $0.7 \text{ W cm}^{-2}$  in order to maintain the temperature in the tumor at  $50\text{-}52^\circ\text{C}$  (**Figures 5.6A, B**) that was seemed to be not causing burns of skin (**Figure 5.6C**). On the contrary, mice without injected nanostructures displayed a rise of temperature of only approximately  $3^\circ\text{C}$  on the tumor area.

The tumor volume was measured at the first day after treatment and then every 3 days. An essential decrease in volume was already seen at the 3<sup>rd</sup> day after the treatment (**Figure 5.6C**) and a tumor volume of less than  $\sim 100 \text{ mm}^3$  was obtained at the 5 day after the therapy.

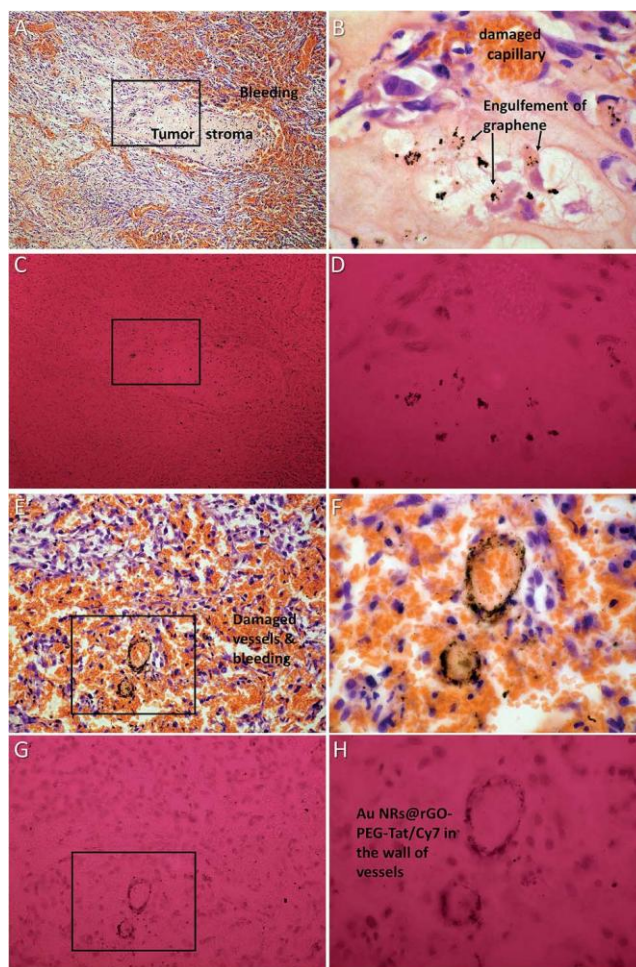


**Figure 5.7:** Histological analysis of tumor tissue obtained 3 h after photo- thermal treatment. (A–D) – region of tumor revealing tumor stroma. (B) – is enlarged (100 objective) area of A (10 objective), indicated by rectangle. (E–H) Region of tumor demonstrating accumulation of Au NRs@rGO-PEG-Tat/Cy7 in the walls of blood vessels. Please note the massive bleeding resulting from massive vessel damage. (F) is enlarged (40 objective) area of E (10 objective), indicated by rectangle. (C & D), (G & H) corresponds to images (A & B), (E & F), obtained under red (620–650 nm) illumination with the aim to visualize Au NRs.

As opposed to this, in the control group, tumors were persistently increasing until achieving of 10 percent of original body weight when the mice have been used in accordance with ethical rules. Histological analysis of tumor material, which was taken from Au NRs@rGO-PEG-Tat treated mice in 3 hours after irradiation, displayed concentration of Au NRs particles in tumor tissue (**Figure 5.7 A-D**) and walls of the vessels (**Figure 5.7 E-H**). Histology showed active uptake of particles of Au NRs@rGO-PEG-Tat by tumor tissue cells in some of the tumor zones (**Figure 5.7B**). The Au NRs@rGO-PEG-Tat particles were seen as black particles by H&E coloring and as severely absorbing material with using of illumination with 620-650 nm of red light. The tumor tissue was filled with blood, which was released from capillaries and some smaller vessels. The capillaries walls were not identified, but those few medium vessels, which were conserved (**Figure 5.7H**) showed intensive concentration of Au NRs@rGO-PEG-Tat in their walls. Anti-angiogenic effect of created Au NRs@rGO-PEG-Tat and selective injuries of vessels make them a very perspective and very effective anti-tumor materials.

## 5.6. Conclusions

It can be concluded that we have displayed the interest of golden nanorods, which covered with PEGylated reduced graphene oxide and then changed with tumor vectors and fluorescent coloring, for photothermal warming using. This multioperational theranostic nanostructures ran effective photothermal elimination of tumors in mice by low dosage of NIR light excitation. Because of the specific interrelation between human glioblastoma astrocytome (U87MG) cells and tat proteins, selective aiming of the tumor was obtained. It is also able to operate as

fluorescent cellular markers, which integrate with the rGO shell thanks to the availability of NIR fluorescent dyes. High Au NRs@rGO-PEG-Tat concentration in the tumor was detected that is essential for selective and effective photothermal therapy. An endosomal-related consuming with following endosomal recycling in the Golgi complex is assumed. The medicinal effect of the new photothermal agents was evaluating by researches *in vivo*, which were conducted on tumor containing mice. It is possible to display that a considerable decrease in tumor volume was seen after 5 days, when irradiation of the tumor area was at  $0.7 \text{ W cm}^{-2}$  for 10 min. Histological examination of tumor matter was reported with parallel active consuming of the nanoparticles by the tumor cells and partial injuring of vessels of the tumor. This selective injuring and anti-angiogenic effect makes us to consider Au NRs@rGO-PEG-Tat as a very perspective anti-tumor medication.

## 5.7. References

1. Koo Y-EL, Reddy GR, Bhojani M, Schneider R, Philbert MA, Rehemtulla A, et al. Brain cancer diagnosis and therapy with nanoplatforms. *Advanced drug delivery reviews*. 2006; 58(14):1556-77.
2. Jin S-E, Jin H-E, Hong S-S. Targeted delivery system of nanobiomaterials in anticancer therapy: from cells to clinics. *BioMed research international*. 2014; 2014.
3. Baffou G, Quidant R. Thermo-plasmonics: using metallic nanostructures as nano-sources of heat. *Laser & Photonics Reviews*. 2013; 7(2):171-87.
4. Zhu X-M, Fang C, Jia H, Huang Y, Cheng CH, Ko C-H, et al. Cellular uptake behaviour, photothermal therapy performance, and cytotoxicity of gold nanorods with various coatings. *Nanoscale*. 2014;6(19):11462-72.
5. Szunerits S, Boukherroub R. Sensing using localised surface plasmon resonance sensors. *Chemical Communications*. 2012;48(72):8999-9010.
6. Zharov VP, Mercer KE, Galitovskaya EN, Smeltzer MS. Photothermal nanotherapeutics and nanodiagnostics for selective killing of bacteria targeted with gold nanoparticles. *Biophysical journal*. 2006; 90(2):619-27.

7. Norman RS, Stone JW, Gole A, Murphy CJ, Sabo-Attwood TL. Targeted photothermal lysis of the pathogenic bacteria, *Pseudomonas aeruginosa*, with gold nanorods. *Nano letters*. 2008; 8(1):302-6.
8. Chen H, Shao L, Li Q, Wang J. Gold nanorods and their plasmonic properties. *Chemical Society Reviews*. 2013; 42(7):2679-724.
9. Mackey MA, Ali MR, Austin LA, Near RD, El-Sayed MA. The most effective gold nanorod size for plasmonic photothermal therapy: theory and *in vitro* experiments. *The Journal of Physical Chemistry B*. 2014; 118(5):1319-26.
10. Akhavan O, Ghaderi E. Graphene nanomesh promises extremely efficient *in vivo* photothermal therapy. *Small*. 2013; 9(21):3593-601.
11. Kuo WS, Chang CN, Chang YT, Yang MH, Chien YH, Chen SJ, et al. Gold nanorods in photodynamic therapy, as hyperthermia agents, and in near-infrared optical imaging. *Angewandte Chemie*. 2010; 122(15):2771-5.
12. Ma Y, Liang X, Tong S, Bao G, Ren Q, Dai Z. Gold Nanoshell Nanomicelles for Potential Magnetic Resonance Imaging, Light-Triggered Drug Release, and Photothermal Therapy. *Advanced functional materials*. 2013; 23(7):815-22.
13. Chen J, Wang D, Xi J, Au L, Siekkinen A, Warsen A, et al. Immuno gold nanocages with tailored optical properties for targeted photothermal destruction of cancer cells. *Nano letters*. 2007; 7(5):1318-22.
14. Vankayala R, Lin C-C, Kalluru P, Chiang C-S, Hwang KC. Gold nanoshells-mediated bimodal photodynamic and photothermal cancer treatment using ultra-low doses of near infra-red light. *Biomaterials*. 2014; 35(21):5527-38.
15. Wang Y, Black KC, Luehmann H, Li W, Zhang Y, Cai X, et al. Comparison study of gold nanohexapods, nanorods, and nanocages for photothermal cancer treatment. *ACS nano*. 2013; 7(3):2068-77.
16. Seo S-H, Kim B-M, Joe A, Han H-W, Chen X, Cheng Z, et al. NIR-light-induced surface-enhanced Raman scattering for detection and photothermal/photodynamic therapy of cancer cells using methylene blue-embedded gold nanorod@ SiO<sub>2</sub> nanocomposites. *Biomaterials*. 2014; 35(10):3309-18.

17. Lim D-K, Barhoumi A, Wylie RG, Reznor G, Langer RS, Kohane DS. Enhanced photothermal effect of plasmonic nanoparticles coated with reduced graphene oxide. *Nano letters*. 2013; 13(9):4075-9.
18. Turcheniuk K, Boukherroub R, Szunerits S. Gold–graphene nanocomposites for sensing and biomedical applications. *Journal of Materials Chemistry B*. 2015; 3(21):4301-24.
19. Chen J, Liu H, Zhao C, Qin G, Xi G, Li T, et al. One-step reduction and PEGylation of graphene oxide for photothermally controlled drug delivery. *Biomaterials*. 2014; 35(18):4986-95.
20. Moon HK, Lee SH, Choi HC. *In vivo* near-infrared mediated tumor destruction by photothermal effect of carbon nanotubes. *ACS nano*. 2009; 3(11):3707-13.
21. Wen H, Dong C, Dong H, Shen A, Xia W, Cai X, et al. Engineered Redox-Responsive PEG Detachment Mechanism in PEGylated Nano-Graphene Oxide for Intracellular Drug Delivery. *Small*. 2012; 8(5):760-9.
22. Zhao M, Kircher MF, Josephson L, Weissleder R. Differential conjugation of tat peptide to superparamagnetic nanoparticles and its effect on cellular uptake. *Bioconjugate chemistry*. 2002; 13(4):840-4.
23. Zhang W, Guo Z, Huang D, Liu Z, Guo X, Zhong H. Synergistic effect of chemophotothermal therapy using PEGylated graphene oxide. *Biomaterials*. 2011; 32(33):8555-61.
24. Robinson JT, Tabakman SM, Liang Y, Wang H, Sanchez Casalongue H, Vinh D, et al. Ultrasmall reduced graphene oxide with high near-infrared absorbance for photothermal therapy. *Journal of the American Chemical Society*. 2011; 133(17):6825-31.
25. Jung HS, Kong WH, Sung DK, Lee M-Y, Beack SE, Keum DH, et al. Nanographene oxide–hyaluronic acid conjugate for photothermal ablation therapy of skin cancer. *ACS nano*. 2014; 8(1):260-8.
26. Lim SP, Garzino-Demo A. The human immunodeficiency virus type 1 Tat protein up-regulates the promoter activity of the beta-chemokine monocyte chemoattractant protein 1 in the human astrocytoma cell line U-87 MG: role of SP-1, AP-1, and NF- $\kappa$ B consensus sites. *Journal of virology*. 2000; 74(4):1632-40.

27. Subramanian P, Lesniewski A, Kaminska I, Vlandas A, Vasilescu A, Niedziolka-Jonsson J, et al. Lysozyme detection on aptamer functionalized graphene-coated SPR interfaces. *Biosensors and Bioelectronics*. 2013; 50:239-43.
28. Teodorescu F, Rolland L, Ramarao V, Abderrahmani A, Mandler D, Boukherroub R, et al. Electrochemically triggered release of human insulin from an insulin-impregnated reduced graphene oxide modified electrode. *Chemical Communications*. 2015; 51(75):14167-70.
29. Wei X-Q, Hao L-Y, Shao X-R, Zhang Q, Jia X-Q, Zhang Z-R, et al. Insight into the Interaction of Graphene Oxide with Serum Proteins and the Impact of the Degree of Reduction and Concentration. *ACS applied materials & interfaces*. 2015; 7(24):13367-74.
30. Chen R, Wang X, Yao X, Zheng X, Wang J, Jiang X. Near-IR-triggered photothermal/photodynamic dual-modality therapy system via chitosan hybrid nanospheres. *Biomaterials*. 2013; 34(33):8314-22.

## CHAPTER VI

### **Reduced graphene oxide nanosheets decorated with AuPd bimetallic nanoparticles for the photothermal treatment of cancer cells**

#### **6.1. Introduction**

The main medicinal method for the therapy of many types of cancer is still chemotherapy. However, the non-specific conveyance of chemotherapeutic materials brings regular side effects for healthy tissues and restricted efficacy in treatment of tumors. A primary flaw of many treatments, which are based on drugs, particularly when they are delivered intravenously or orally, is that the medication does not aimed to the target place. The purpose of cancer treatments, which are based on nanostructures, is to develop the feature of the particles to concentrate themselves in the tumor by active or passive aiming on the tumor (1). One tool for the selective removing of carcinoma cells is by subjecting of the tumor/particle union to laser light in order to obtain localized hyperthermia. After the first research by Halas and his co-workers in 2003, who showed that near-infrared (NIR) irradiation of gold-on-silica nano-coverings brought to increase of the temperature of the targeted area to 40 - 50 °C that enabled the selective killing of breast carcinoma cells (2), many various photothermal nanostructures have investigated for NIR photothermal treatment (PTT) of tumor. Using of NIR light has much more merits, since melanin, hemoglobin and water have consuming minimum about 700-900 nm, and light at this wavelengths is most appropriate in order to pass directly through tissues without essential consuming and warmth generation. (3) Golden nanoparticles (of Au NPs) mediated hyperthermia is the most researched PTT system to this day (4-9). Recently, many efforts have sought to improve the efficacy of the photothermal transformation of NIR PTT nanostructures by optimization of the Au NPs shape, (10) by covering of golden nanorods (Au NRs) with matrixes similar to mesoporous silica, (11) metallic covers like Pt nanodots, (12) or graphene oxide

derivatives (13, 14). The severe NIR optical consuming capability of poly(ethylene glycol)-covered decreased graphene oxide PEG-rGO with its rapid light-to-heat transformation, good ability to be insignificant in biological environments and low cytotoxicity have made nanomaterials, which are based on rGO, perfect photothermal materials (13, 15-20). The synergetic effect of a compound of Au NRs with PEG-rGO nanomaterials on the photothermal features has been demonstrated lately by covering of Au NRS with PEG-rGO (13, 21).

In this chapter, motivated by such results, we study the photothermal features of bimetallic AuPd NPs, which are included in PEG-rGO. As we know, palladium nanosheets were used as photothermal material in order to deactivate cancer cells (22, 23). It is strange, but bimetallic Au-Pd system, which has been investigated very well, have still not been considered as photothermal material. However, to construct bimetallic nanostructures is an interesting method in order to create nanomaterials, which possess various chemical and physical features,(24) and AuPd alloy is one of the most significant compounds, which is researched widely as a catalyst for different reactions, including the electro-oxidation of formic acid and methanol, and is going to be a perspective candidate for agents of hydrogen storage (25-29). In thesis, we want to show that the synergistic effects of these three compounds improves significantly the photothermal features of the complex substance, thereby enabling them to function as an excellent photothermal material against cancer cells, compared with their monometallic counter parts.

## **6.2. Synthesis and characteristics of AuPd NPs-rGO-PEG nanocomposites**

The modified procedure of Hummer was used in order to prepare graphene oxide (GO) by using of natural graphite as initial substance (30). The finest and well scattered AuPd-NPs is able to be produced on GO with the help of mixing of the metallic precursors, with GO in watery substance at room temperature (**Figure 6.1**). AuPd NPs is able to grow immediately on GO thanks to a self-acting redox reaction between  $\text{HAuCl}_4$ ,  $\text{PdCl}_2$  and GO at room temperature in short period of time (28, 31). Ascorbic acid addition leads to the synchronous reduction of GO to reduced graphene oxide (rGO). In order to render the created AuPd NPs-rGO dispersible both in aqueous solutions and in biological environments, linear poly(ethyleneglycol) bis(3-aminopropyl) ( $\text{NH}_2\text{PEGNH}_2$ ) was grafted through an EDC activation reaction to the To the remaining

carboxylic acid functions of rGO, which suppress to this moment. The successful synthesis of AuPd NPs-rGO-PEG was proved by X-ray photoelectron spectroscopy (XPS), Raman analysis and transmission electron microscopy (TEM).

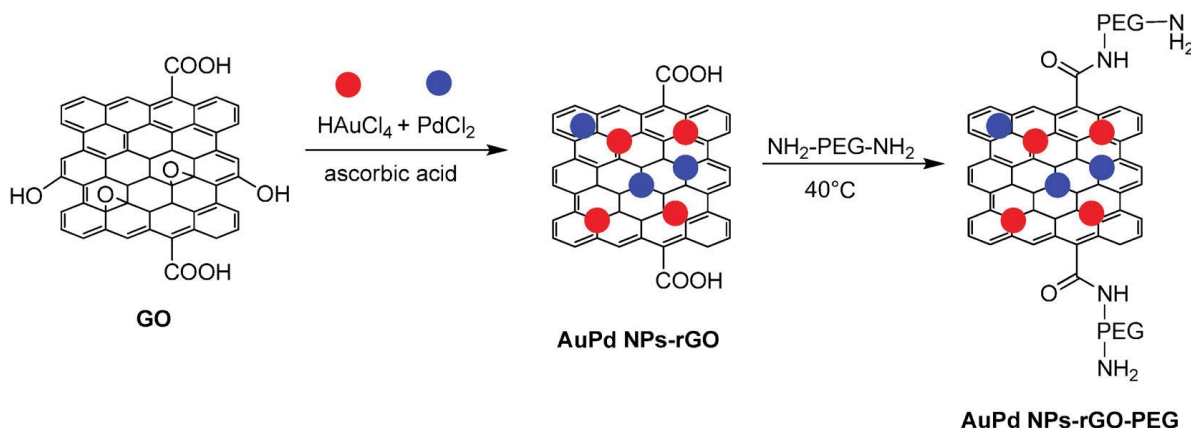


**Figure 6.1:** Schematic representation of the synthesis of the AuPd NPs–rGO–PEG nanocomposites photothermal agent.

The TEM was used in order to assess the morphology of the created pegylated functionalized Au Pd NPs-rGO-PEG nanocomposite, **Figure 6.2a** shows TEM pictures of the bimetallic NPs nanocomposite under different magnifications. The TEM pictures of low magnification (**Figures 6.2 a,b**) display that the Au Pd NPs-rGO-PEG product includes many particles, which are distributed non-uniformly throughout rGO nanosheets with volume distribution of 40-60 nm and approximate diameter of 47 nm as seen from volume distribution graph (**Figure 6.2c**).

The TEM pictures of high resolution of Au Pd NPs (**Figures 6.1 d,e**) prove the alloy origin of the nanocomposites, with clear borders of Au and Pd NPs being seen with interplanar spaces of 0.230 nm and 0.19 nm, which respectively correspond to (111) and (200) planes of fcc Au and Pd NPs. The selected zone electron diffraction (SAED) model (**Figure 6.2f**) reflects the highly polycrystalline origin of the nanocomposites, where beaming places are corresponding to fcc planes of Au and Pd NPs. The appropriate TEM pictures of the controls Pd NPs-rGO-PEG and Au NPs-rGP-PEG are showed

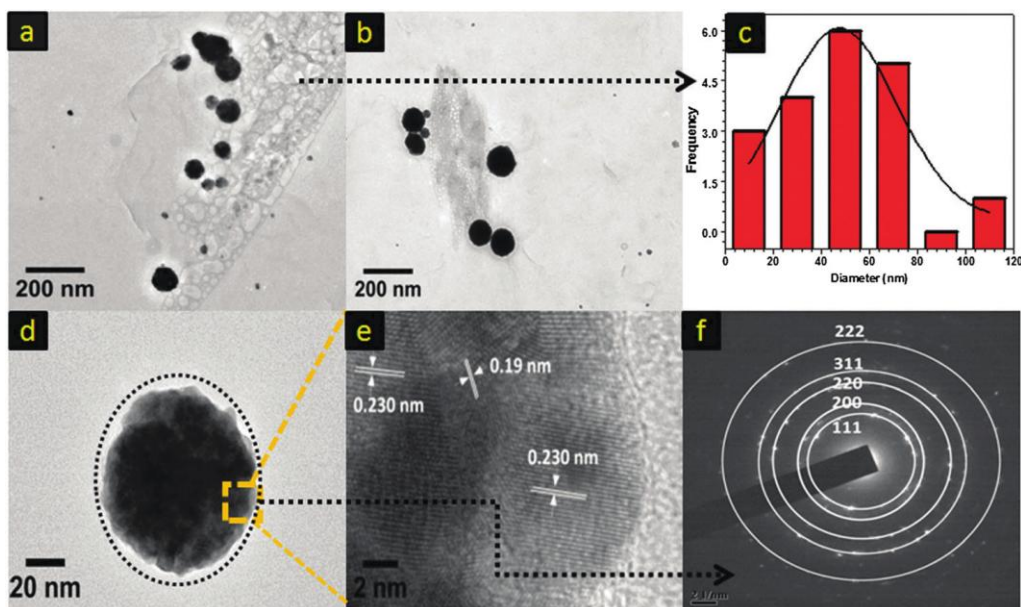


**Figure 6.2:** (a and b) Low-magnified TEM images of AuPd NPs-rGO-PEG nanocomposites, (c) particle size distribution, (d) HRTEM image of one bimetallic AuPd NP, (e) AuPd bimetallic NPs with fringes of both Au and Pd NPs along with interplanar spacings, and (f) SAED pattern.

In accordance with XPS analysis bands due to O1s (27.3 at %), C1s (68.8 at %), N1s (2.3 at %), Au4f (0.4 at %) as well as Pd3p (1.2 at %) are seen according to the chemical compound of AuPd-rGO-PEG (**Figure 6.3A**). The C1s spectrum of high resolution displays two strong bands at 285.7 eV (C-O, C-N) and 283.8 eV ( $sp^2$  network), with more little contribution at 286.2 (C-O-C). The reducing of the band at 285.7 eV for AuPd NPs-rGO-PEG in comparison with GO shows the transformation of carbonyl and carboxyl groups into hydroxyl groups (C-OH) as ascorbic acid is a light decreasing agent. The Au 4f spectre (**Figure 6.3A**) showed two maximum values of  $4f_{5/2}$  and  $4f_{7/2}$  at 87.6 eV and 84 eV, respectively. The restrictions powers recorded are compatible with zerovalent Au. The high resolution XPS in the Pd area opens four maximum values (two pairs) (**Figure 6.3D**), one pair at 340.9 eV and 335.6 and showing Pd  $3d_{3/2}$  and Pd  $3d_{5/2}$ , respectively, which is in good relevance with the literature values (341.1 eV and 335.5) of bulk Pd(0). Another pair of maximum values at 343.6 eV and 338.3 are extremely near to the displayed values of Pd(II) which showed that the Pd surface is partly oxidized. For contrast, the appropriate XPS in forming for Pd NPs-rGO-PEG and Au NPs-rGO-PEG are depicted in **Figure**

**6.3.** In the event of Au NPs-rGO-PEG, the amount of Au is in presence for 0.3 at %, at the same time 0.6 at % of Pd is available in Pd NPs-rGO-PEG.

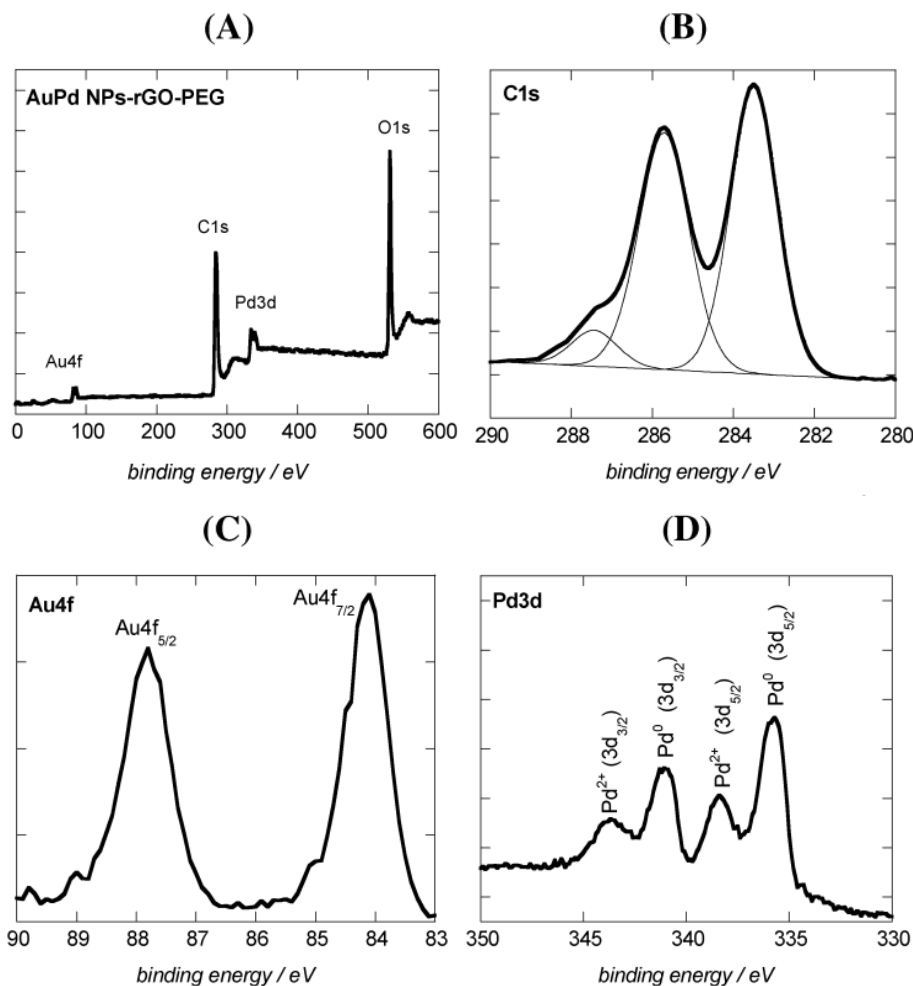


**Figure 6.3.** XPS analysis of AuPd NPs-rGO-PEG nanocomposites (A), XPS survey spectrum, the high resolution XPS spectra of C<sub>1s</sub> (B), Au<sub>4f</sub> (C) and Pd<sub>3d</sub> (D).

The Raman picture of AuPd NPs-rGO-PEG (**Figure 6.4A**) displays G ( $\approx 1580 \text{ cm}^{-1}$ ) and tD ( $\approx 1350 \text{ cm}^{-1}$ ) bands, which are appointed to the local flaws/disorder and the  $\text{sp}^2$  graphitized structure of rGO-PEG and GO-PEG respectively (32). The  $I_D/I_G$  intensiveness ratio was 0.80, more little than then original 1.19 for GO (**Figure 6.4**), proving the enhancing in the  $\text{sp}^2$  graphitized structure of rGO-PEG of the sheets during the period of the decreasing process with

ascorbic acid. The 2D band is placed at  $2698\text{ cm}^{-1}$  with an extra shoulder, which is directed to higher wavelengths, showing an ascendant monolayer to bilayer structure (33, 34).

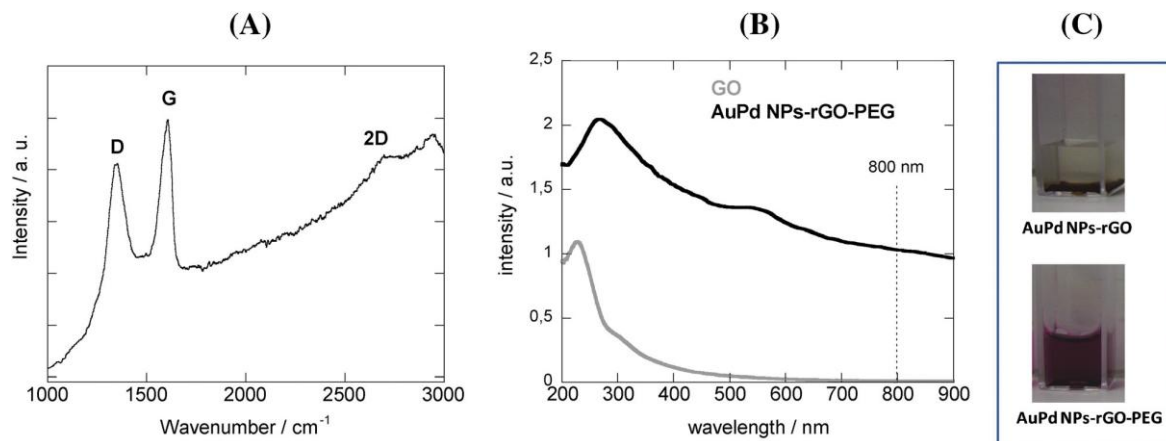


**Figure 6.4.** (A) Raman spectrum of AuPd NPs-rGO-PEG nanocomposites and (B) UV/Vis absorption spectra of GO (grey) and AuPd NPs-rGO-PEG nanocomposites ( $75\text{ mg mL}^{-1}$ , black); (C) dispersion of the AuPd NPs-rGO and AuPd NPs-rGO-PEG nanocomposites ( $50\text{ mg mL}^{-1}$ ) in DMEM.

The physiological firmness of AuPd NPs-rGO-PEG in biological environment was researched. The research showed that AuPd NPs-rGO assembled and hastened almost at once, at the same time AuPd NPs-rGO-PEG suppressed quite in the DMEM without assembling for several months that reflects the physiological firmness for later applications *in vivo* (Figure 6.4C).

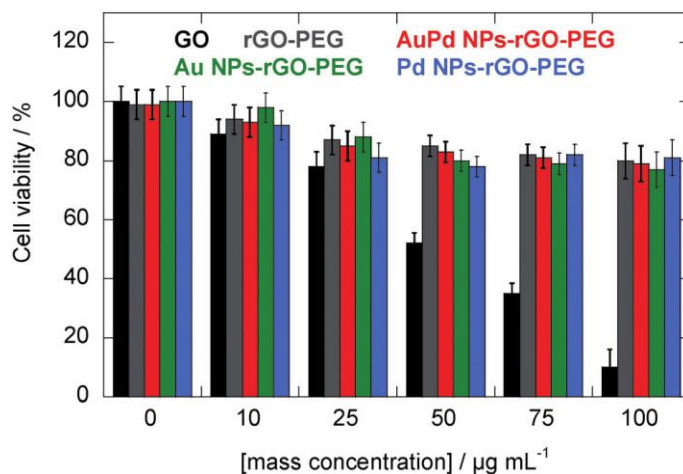


**Figure 6.5:** Relative cell viabilities of HeLa cells after incubation with AuPd NPs-rGO-PEG

(red), GO (black), rGO-PEG (grey), Au NPs-rGO-PEG (green) and Pd NPs-rGO-PEG (blue) for 72 h. Error bars were based on triplet samples.

In order to ensure whether AuPd NPs-rGO-PEG nanocarriers are non-toxic to cells of HeLa cancer, MTS assay were used in order to define the cytotoxicity effects on HeLa cancer cells. As seen in **Figure 6.5**, high viability of the cell (>85 %) were detected for various concentration of AuPd NPs-rGO-PEG after incubating it for 72h, even at concentration up to  $100 \mu\text{g mL}^{-1}$ , showed a great biocompatibility, particularly in comparison with GO. In order to compare, the cytotoxicity of Pd NPs-rGO-PEG and Au NPs -rGO-PEG nanocomposites was defined, at the same time being comparable with that of AuPd NPs -rGO-PEG. Really, the PEGylated nanostructures manifest cytotoxicity as rGO-PEG which have been reported before (16), implicating the fact that the availability of PEG units is liable for the non-toxic property of the nanostructures, depending on the availability of metallic nanoparticles.

### **6.3. Photothermal efficacy and photothermal removing of cancer cells**

The light-to-heat transformation efficiency of AuPd NPs- rGO-PEG was next examined. To this aim, temperature increase of AuPd NPs-rGO- PEG solution at different concentrations upon irradiation with persistent NIR laser wave (800 nm) at  $1 \text{ W.cm}^{-1}$  were recorded for 10 min. (**Figure 6.6A**). At an concentration above  $6 \mu\text{g mL}^{-1}$ , NIR irradiation increase the temperature about  $40 \text{ }^\circ\text{C}$ , which is believed to be quite high for photothermal cancer removing. (35) Using 12.5 times bigger AuPd NPs-rGO-PEG with concentration ( $75 \mu\text{g mL}^{-1}$ ) enables to increment the temperature of the solution further to nearly  $80 \text{ }^\circ\text{C}$ , which is high enough for the killing of pathogenic organisms (16). Incrementing the laser energy to  $2 \text{ W cm}^{-1}$  has a little influence on the final temperature of the substance (**Figure 6.6B**); Temperatures, which are necessary for the removing of cancer tumors are able to be achieved at this AuPd NPs-rGO-PEG concentration ( $75 \mu\text{g mL}^{-1}$ ) with a laser energy of  $0.5 \text{ W cm}^{-1}$  only. Output powers, which are greater than  $2 \text{ W cm}^{-1}$ , injure substantially the surface of neighboring tissue, at the same time PTT at  $0.5 \text{ W cm}^{-1}$  is in the normal safe zone and is appropriate for clinical cancer therapy (19). Compared to substance temperatures, which are achieved with using of the same parameters ( $75 \mu\text{g mL}^{-1}$ ,  $0.5 \text{ W cm}^{-1}$ ), the required  $40 \text{ }^\circ\text{C}$  is not achieved in the case of rGO-PEG and just in the case of Au NPS-rGO-

PEG and Pd NPs-rGO-PEG, proving the better functioning of AuPd NPs-rGO-PEG nanostructures because of a synergetic impact of all three components involved.

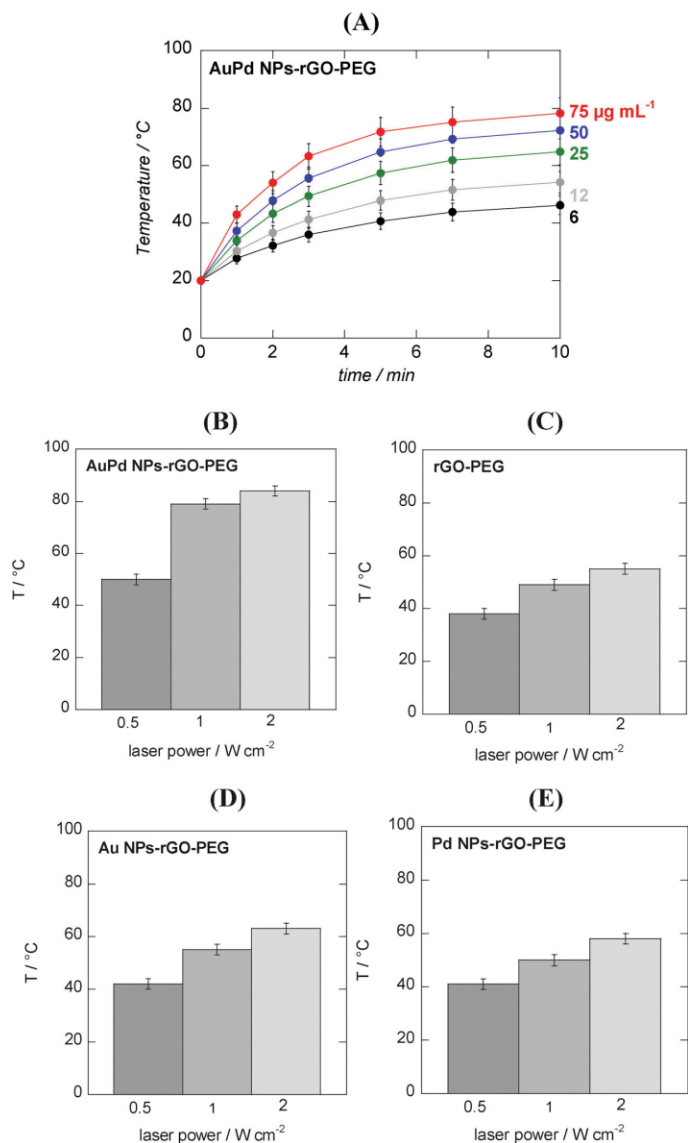


**Figure 6.6:** (A) Influence of AuPd NPs-rGO-PEG nanocomposites concentration on solution temperature upon irradiation for 10 min at 800 nm using a laser power of  $1 \text{ W cm}^{-2}$ ; (B-E) photothermal effect of different rGO-PEG nanocomposites ( $75 \text{ mg mL}^{-1}$ ) based nanostructures: (B) AuPd NPs-rGO-PEG nanocomposites, (C) rGO-PEG, (D) Au NPs-rGO-PEG nanocomposites, (E) Pd NPs-rGO-PEG nanocomposites upon irradiation for 10 min at 800 nm

using laser powers of 0.5, 1 and 2 W cm<sup>-2</sup>.

The efficient photothermal warming features of AuPd NPs-rGO-PEG were then used in order to assess the cytotoxicity *in vitro* under irradiation by NIR light with incubating HeLa cancer cells with growing accumulations of AuPd NPs-rGO-PEG and irradiating the cell culture environment for 10 minutes at 800 nm at 0.5 and 1 W cm<sup>-2</sup>. AuPd NPs-rGO-PEG without light irradiation was used as the mean of control and indicated a very slight reduction of cell viability (**Figure 6.7**).

**Figure 6.7** displays MTS cell viability of HeLa cancer cells after incubation with AuPd NPs-rGO-PEG at 75 μg mL<sup>-1</sup> under NIR irradiation too.

Almost all the cells (approximately 97 %) were eliminated after NIR irradiation during 10 min. In the case of a laser energy of 1 W cm<sup>-2</sup>, a AuPd NPs-rGO-PEG accumulation of 20 μg mL<sup>-1</sup> is enough for the total photo-removing of the cancer cells, with a cell elimination of 50 % (LC<sub>50</sub>) at a AuPd NPs-rGO-PEG accumulation of 7 μg mL<sup>-1</sup>.

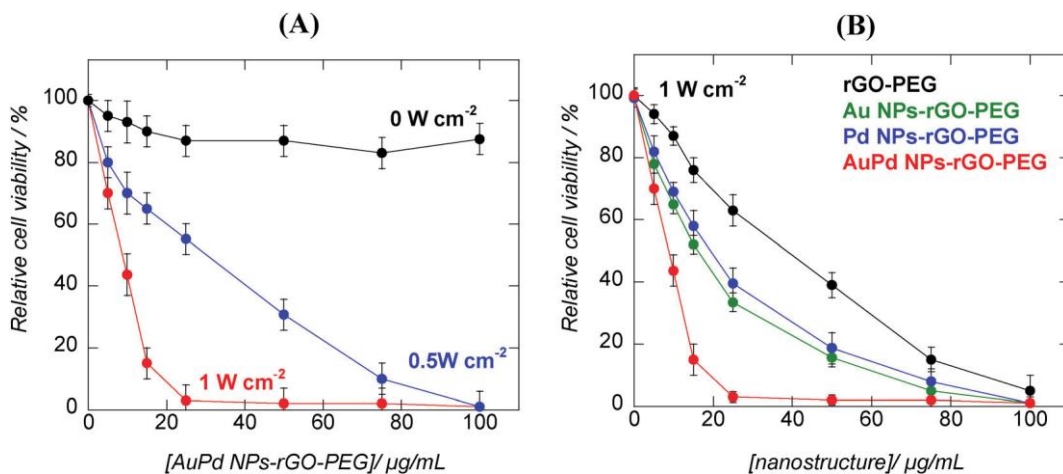


**Figure 6.7:** Relative cell viabilities of HeLa cells after irradiation (808 nm, 10 min) in the presence of 75 mg mL<sup>-1</sup> of (A) AuPd NPs-rGO-PEG nanocomposites at 0.5 W cm<sup>-2</sup> (blue), 1 W cm<sup>-2</sup> (red) and 0 W cm<sup>-2</sup> (black) and for (B) AuPd NPs-rGO-PEG nanocomposites (red) Au NPs-rGO-PEG nanocomposites (green), Pd NPs-rGO-PEG nanocomposites (blue) and rGO-PEG (black) at 1 W cm<sup>-2</sup>: error bars were based on quartet samples.

These states are comparable to that, which was reported by Ghaderi and Akhavan (19) for the removing of human glioblastoma cells with using of graphene nanomesh substances of  $10 \mu\text{g mL}^{-1}$  with NIR power thickness of  $0.1 \text{ W cm}^{-2}$  for 7 min. Laser energies of  $0.5 \text{ W cm}^{-2}$  display a planned incremented  $\text{LC}_{50}$  numbers to  $40 \mu\text{g mL}^{-1}$  AuPd NPs-rGO-PEG.

## 6.4. Conclusions

We have showed a green and elementary synthetic method for the creation of bimetallic AuPd NPs on rGO nanosheets with the help of an environment-friendly reduction material. The rGO, which includes AuPd NPs, displays the approximate size of 32 nm. Covalent fastening of PEG units to the carboxylic acid groups of AuPd NPs-rGO enhanced significantly the solvability and firmness of the nanostructure in bio-environment and provided the bio-convenient feature towards cancer cells such as HeLa. The AuPd NPs-rGO-PEG nanostructures is able to be used successfully in the future for the photothermal removing *in vitro* of HeLA cells. The use of AuPd NPs-rGO-PEG accumulations of  $6 \mu\text{g mL}^{-1}$  and a laser energy of  $1 \text{ W cm}^{-2}$ , which is resulted in substance temperatures of approximately  $58 \text{ }^\circ\text{C}$ , is enough for the removing of cancer tissue. Increasing the concentration to  $75 \mu\text{g mL}^{-1}$  generated substance temperatures to  $80 \text{ }^\circ\text{C}$ . This high efficacy was appointed mainly to the synergetic impact of rGO, Pd NPs and Au NPs. This research may reveal new opportunities of development of improved materials for using as potential photothermal variants for therapy of various unregulated cells.

## 6.5. References

1. Xiao Z, Ji C, Shi J, Pridgen EM, Frieder J, Wu J, et al. DNA Self-Assembly of Targeted Near-Infrared-Responsive Gold Nanoparticles for Cancer Thermo-Chemotherapy. *Angewandte Chemie*. 2012; 124(47):12023-7.
2. Loo C, Lowery A, Halas N, West J, Drezek R. *Nano Lett*. 2005; 5:709.
3. Weissleder RA. A clearer vision for *in vivo* imaging. *Nat Biotechnol*. 2001;19(4):316.
4. Qiu Y, Liu Y, Wang L, Xu L, Bai R, Ji Y, et al. *Biomaterials*. 2014; 31:7606-19.
5. Cogley CM, Chen J, Cho EC, Wang LV, Xia Y. Gold nanostructures: a class of multifunctional materials for biomedical applications. *Chem Soc Rev*. 2011; 40:44-56.

6. Dreaden ED, Alkilany AM, Huang X, Murphy CJ, El-Sayed MA. The golden age: gold nanoparticles for biomedicine. *Chem Soc Rev* 2012; 41:2740-79.
7. Jain PK, Huang J, El-Sayed IH, El-Sayed MA. *Acc Chem Res.* 2008; 41:1578.
8. Liang S, Zhao Y, Xu S, Wu X, Chen J, Wu M, et al. A Silica–Gold–Silica Nanocomposite for Photothermal Therapy in the Near-Infrared Region. *ACS Appl Mater Interfaces.* 2015; 7:85-93.
9. Mout R, Moyano DF, Rana S, Rotello VM. Surface functionalization of nanoparticles for nanomedicine. *Chem Soc Rev.* 2012; 41:2539-44.
10. Wang Y, Black KC, Luehmann H, Li W, Zhang Y, Cai X, et al. *ACS Nano.* 2013;7:2068-77.
11. Zhang Z, Wang L, Wang J, Jiang X, Li X, Hu Z, et al. *Adv Mater.* 2012;24:1418-23.
12. Tang J, Jiang X, Wang L, Zhang H, Hu Z, Liu Y, et al. Au@Pt nanostructures: a novel photothermal conversion agent for cancer therapy. *Nanoscale.* 2014; 6:3670.
13. Turcheniuk K, Hage C-H, Spadavecchia J, Serrano AY, Larroulet I, Pesquera A, et al. Plasmonic photothermal destruction of uropathogenic *E. coli* with reduced graphene oxide and core/shell nanocomposites of gold nanorods/reduced graphene oxide. *J Mater Chem B.* 2015; 3(3):375-86.
14. Lim D-K, Barhoumi A, Wylie RG, Reznor G, Langer RS, Kohane DS. Enhanced photothermal effect of plasmonic nanoparticles coated with reduced graphene oxide. *Nano Lett.* 2013; 13(9):4075-9.
15. Chen J, Liu H, Zhao C, Qin G, Xi G, Li T, et al. *Biomaterials.* 2014; 35:4986.
16. Turcheniuk K, Hage C-H, Heliot L, Railyan S, Zaitsev V, Spadavecchia J, et al. *Nano Life* 2014.
17. Kim H, Kim WJ. *Small.* 2013; 10:117-26.
18. Akhavan O, Ghaderi E, Emamy H. *J Mater Chem* 2012; 22:20626.
19. Akhavan E, Ghaderi E. Graphene nanomesh promises extremely efficient *in vivo* photothermal therapy. *Small.* 2013; 9(21):3593-601.

20. Robinson JT, Tabakman SM, Liang Y, Wang H, Casalongue HS, Vinh D, et al. Ultrasmall Reduced Graphene Oxide with High Near-Infrared Absorbance for Photothermal Therapy. *J Am Chem Soc.* 2011; 133(17):6825-31.
21. Turchniuk K, Boukherroub R, Szunerits S. Gold-graphene nanocomposites for sensing and biomedical applications. *J Mater Chem; B.* 2015.
22. Huang X, Tang S, Mu X, Dai Y, Chen G, Zhou Z, et al. Freestanding palladium nanosheets with plasmonic and catalytic properties. *Nat Nanotechnol.* 6:28-32.
23. Tang S, Huang X, Zheng N. Silica coating improves the efficacy of Pd nanosheets for photothermal therapy of cancer cells using near infrared laser. *Chem Commun.* 2011;47:3948–50.
24. Alloeyau D, Ricolleau C, Mottet C, Oikawa T, Langlois C, Le Bouar Y, et al. *Nat Mater.* 2009; 8:940–94.
25. Horinouchi S, Yamanoi Y, Yonezawa T, Mouri T, Nishihara H. *Langmuir.* 2006; 22: 1880–4.
26. Menegazzo F, Canton P, Pinna F, Pernicone N. *Catal Commun.* 20085; 9:2353–6.
27. Harpeness R, Gedanken A. Microwave Synthesis of Core-Shell Gold/Palladium Bimetallic Nanoparticles. *Langmuir.* 2004; 20:3431-4.
28. Chen X, Cai Z, Chen X, Oyama M. AuPd bimetallic nanoparticles decorated on graphene nanosheets: their green synthesis, growth mechanism and high catalytic ability in 4-nitrophenol reduction. *J Mater Chem A.* 2014; 2:5668-74.
29. Chai J, Li F, Hu Y, Zhang Q, Hana D, Niu L. Hollow flower-like AuPd alloy nanoparticles: One step synthesis, self-assembly on ionic liquid-functionalized graphene, and electrooxidation of formic acid. *J Mater Chem A.* 2011; 21: 17922–9.
30. Das MR, Sarma RK, Saikia R, Kale VS, Shelke MV, Sengupta P. Synthesis of silver nanoparticles in an aqueous suspension of graphene oxide sheets and its antimicrobial activity. *Colloids and Surfaces B: Biointerfaces.* 2011; 83:16–22.
31. Chen XM, Wu GH, Chen JM, Chen X, Xie ZX, Wang XR. *J Am Chem Soc.* 2011; 133:3693-965.

32. Graf D, Molitor F, Ensslin K, Stampfer C, Jungen A, Hierold C, et al. *Nano Lett.* 2007; 7:238.
33. Akhavan E, Ghaderi E. *J Phys Chem B.* 2011; 115:9279.
34. Kim KS, Zhao Y, Jang H, Lee SY, Kim JM, Kim KS, et al. *Nature.* 2009; 457:706.
35. Jung HS, Kong WH, Sung DK, Lee M-Y, Beack SE, Keum DH, et al. Nanographene Oxide–Hyaluronic Acid Conjugate for Photothermal Ablation Therapy of Skin Cancer. *ACS Nano.* 2014; 8:260-68

## CHAPTER VII

### Conclusion and Perspectives

The past decade has observed significant advancement in the field of nanobiotechnology. Large number of nanoparticles (NP)-based products have been enormously approved and used for both diagnostic and therapeutic purposes, and more are recently under clinical trials. Among the large numbers of NPs, functionalized NPs are gaining recognition due to the facts that they can be well fitted for the development of targeted and personalized nanomedicines.

For the surface functionalization of NPs, different strategies have been reported making such functionalized nanostructures suitable for grafting therapeutics or diagnostics. In this thesis, we have developed surface modification pathways that can be adopted for varies of nanostructures like nanodiamonds (NDs), gold nanorods (Au-NRs) and Au-Pd bimetallic nanocomposites. Surface modification of nanostructures has also been exploited. As an application, we have grafted menthol derivative on surface of NDs and made coupling with glycans through azido group on nanodiamond surface. These particles were shown their ability to inhibit Gram-positive (*Staphylococcus aureus*) and Gram-negative (*Escherichia coli*) bacteria. From another site Au-NRs were investigate for their ability in photodynamic and photothermal therapy.

First, we described the development of novel nanostructures for photodynamic therapy comprising silica-encased gold nanorods modified with verteporfin as photosensitizer. The structure of the Au NRs was tuned to be in resonance with the absorption maximum of verteporfin. We demonstrated that the Au NRs@SiO<sub>2</sub>-VP were photothermally stable and able to generate a significant amount of reactive oxygen species when illuminated at 710 nm at 500 mW cm<sup>-1</sup> using a continuous or a pulsed laser source. The efficiency of the nanostructures for killing of pathogens depends on time and the laser wavelength used. The approach could be an alternative strategy to destroy wound-infected antibiotic resistant microorganisms due to the efficient bactericidal character, the strong local character of the NIR-based treatment. The deleterious side-effects present upon visible light excitation would be minimized using this approach.

Second, we have shown the interest of gold nanorods coated with PEGylated reduced graphene oxide and further modified with tumor vectors and fluorescent dyes for photo-thermal heating applications. This multifunctional theranostic nanostructures exerted efficient photothermal destruction of tumors in mice upon low dose of NIR light excitation. Due to the specific interaction between tat proteins with human glioblastoma astrocytome (U87MG) cells, selective targeting of the tumor was achieved. So, selective damages of vessels and anti-angiogenic effect of created Au NRs@rGO-PEG-Tat makes them a very promising effective anti-tumor agent.

Third, we showed a simple and green solution phase synthetic approach for the formation of bimetallic AuPd NPs on rGO nanosheets using an eco-friendly reducing agent. The rGO nanosheets embedded AuPd NPs functionalized with PEG chains have an average size of 47 nm. Covalent attachment of PEG units to the remaining carboxylic acid groups of AuPd NPs-rGO nanocomposites greatly improved the solubility and stability of the nanocomposites in biological medium and ensured its biocompatibility towards cancer cells such as HeLa. The AuPd NPs-rGO-PEG nanocomposite was successfully applied for the *in vitro* photo-thermal ablation of HeLa cells. Using AuPd NPs-rGO-PEG concentrations of  $6 \text{ mg mL}^{-1}$  and a laser power of  $1 \text{ W cm}^{-2}$  resulted in solution temperature  $\approx 58 \text{ }^\circ\text{C}$ , which is sufficient for the ablation of cancerous cells. Increasing the concentrations to  $75 \text{ mg mL}^{-1}$  generated solution temperatures up to  $80 \text{ }^\circ\text{C}$ . We demonstrated that using a laser power of  $1 \text{ W cm}^{-2}$  and AuPd NPs-rGO-PEG nanocomposites concentrations of  $\approx 20 \text{ mg mL}^{-1}$  the near total ( $\approx 97\%$ ) photoablation of HeLa cells was achieved, with a  $\text{LC}_{50}$  determined as  $7 \text{ } \mu\text{g mL}^{-1}$ . Such high efficiency was principally assigned to the synergetic effect of rGO, AuPd NPs and PEG molecules. The present investigation might open up new possibilities towards the development of advanced materials for use as potential photothermal candidates for the treatment of different unregulated cells. However, their real potential *in vivo* settings has still to be determined

In this thesis, we have given special attention to nanodiamonds which are considered as a promising candidate for various biological applications because of its superior biocompatibility nature and an excellent surface chemistry and non-toxicity. We have mainly focused on the surface modifications strategies and improvement of NDs stability since they tend to aggregate

and form bigger particles which limit its applications. The perspectives of such nanostructures are wide. Applications to inhibit biofilm formation and to study sugar/lectin binding events are and will be under considerations. The future of the interdisciplinary research that brings organic chemistry, nanotechnology and biology together is thus bright.

# APPENDIX

## Experimental part

### 7.1. Materials

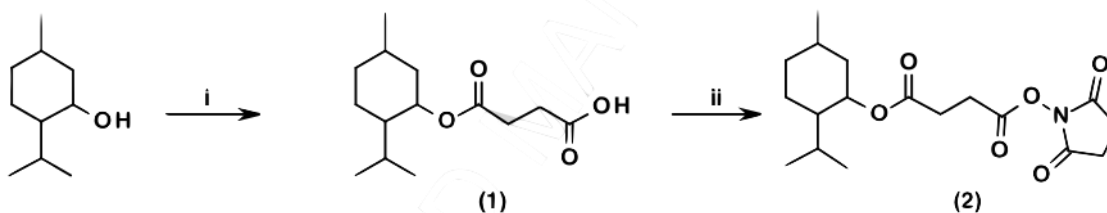
Hydroxyl-terminated nanodiamond (ND-OH) particles were purchased from International Technology Center (Raleigh, NC, USA) and exhibit a primary average particle size of 4.0 nm. (1R,2S,5R)-(-)-Menthol, 4-dimethylaminopyridine (4-DMAP), succinic anhydride, hexane (Hex), dichloromethane (CH<sub>2</sub>Cl<sub>2</sub>), chloroform (CHCl<sub>3</sub>), ethyl acetate (EtOAc), *N,N'*-dicyclohexylcarbodiimide (DCC) and *N*-hydroxysuccinimide (NHS), Methyl pentafluorobenzoate, sodium azide (NaN<sub>3</sub>), dimethylformamide (DMF), diethyl ether, magnesium sulfate (MgSO<sub>4</sub>), acetone, methanol (MeOH), dichloromethane (DCM), sodium hydroxide (NaOH), hydrochloric acid (HCl), *N,N'*-dicyclohexylcarbodiimide (DCC), 4-dimethylaminopyridine (DMAP), copper(II) sulfate pentahydrate (CuSO<sub>4</sub>·5H<sub>2</sub>O), l-ascorbic acid, ethylenediaminetetraacetic acid (EDTA), mannose, glucose, galactose, lactose, sucrose, maltose, mannan (from *Saccharomyces cerevisia*), FITC-labeled *Concanavalin A* (from *Canavalia ensiformis*), FITC-labeled *Lens culinaris* (LENS) and FITC-labeled *Arachis hypogaea* (PNA) Cetyl trimethylammonium bromide (CTAB), silver nitrate (AgNO<sub>3</sub>), hydrogen tetrachloroaurate(III) trihydrate (HAuCl<sub>4</sub>×3H<sub>2</sub>O), tetraethylorthosilicate (TEOS), verteporfin, 9,10-anthracenediylbis (methylene)dimalonic acid (ABDA), sodium borohydride (NaBH<sub>4</sub>), Graphite, chloroacetic acid, sodium hydroxide, poly(ethyleneglycol)-bis(3-aminopropyl) (NH<sub>2</sub>PEGNH<sub>2</sub>, M<sub>w</sub> 1/4 1.5 kDa), *N*-(3-dimethylaminopropyl)-*N'*-ethylcarbodiimide (98%, EDC), cetyltrimethylammonium bromide (CTAB), tetra- chloroauric acid trihydrate (HAuCl<sub>4</sub>\*3H<sub>2</sub>O), silver nitrate (AgNO<sub>3</sub>), ascorbic acid, sodium borohydride (NaBH<sub>4</sub>), para- formaldehyde, hydrochloric acid, fluorescein-isothiocyanate (FITC), Fluoroshield™ with 1,4-diazobicyclo[2.2.2]octane and HIV-1 Tat protein were purchased from Sigma-Aldrich. Azido benzoic acid was purchased from TCI Europe (Belgium). Graphite powder (<20 μm, Sigma-Aldrich), sulfuric acid (AR grade, Qualigens, India), hydrochloric acid (AR grade, Qualigens, India), H<sub>2</sub>O<sub>2</sub> (30%, Qualigens, India), potassium permanganate (499%, Merck, India), gold(III)

chloride trihydrate (Sigma Aldrich), palladium(II) chloride (99.9%, Alfa Aesar), L-ascorbic acid (Sigma Aldrich), poly(ethylene glycol)bis(3-aminopropyl) ( $M_w = 1.5$  kDa, Sigma Aldrich) and *N*-(3-dimethylaminopropyl)-*N'*-ethylcarbodiimide (98%, EDC, Sigma Aldrich) were used as received. Ultrapure water (Milli-Q, 18 MWcm) was used for the preparation of the solutions and for all rinsing steps. Dulbecco's modified Eagle medium (DMEM) was obtained from Gibco by Life Technologies. U-87MG human glioblastoma astrocytoma was acquired from Sigma-Aldrich. Cy7-NHS ester was obtained from Lumiprobe. Sterile PBS solution, Fetal Bovine Serum (FBS) and antibiotics (penicillin/streptomycin) were obtained from Gibco by Life Technologies. CellMask™ Deep Red plasma membrane stain (C10046) was acquired from Life technologies. Hoechst 33342 trihydrochloride trihydrate was obtained from Invitrogen. Matrigel™ Matrix Growth Factor Complete medium from BD Biosciences (USA), MTS tetrazolium dye was acquired from Promega (France).

All microbiological media, equipment and the ampicillin were purchased from Fisher Scientific (UK).

## 7.2. Synthesis of organic compounds

### 7.2.1. Synthesis of menthol derivative (2)



Succinic acid mono-(2-isopropyl-5-methyl-cyclohexyl) ester (1) To a solution of menthol (0.8 g, 5 mmol) in chloroform, 4-DMAP (0.31 g, 2.5 mmol) and succinic anhydride (1.02 g, 10 mmol) were added. This mixture was stirred overnight under reflux. After solvent evaporation, the crude product was purified by flash column chromatography using Hex:EtOAc as eluent to give white crystals 1.1 g (84 %).  $^1\text{H NMR}$  (300 MHz,  $\text{CDCl}_3$ )  $\delta$  12.2-11.1 (broad, 1H) 4.77-4.68 (m, 1H),

2.67-2.55 (m, 4H), 2.05-1.95 (m, 1H), 1.91-1.79 (m, 1H), 1.74-1.62 (m, 2H), 1.55-1.33 (m, 2H), 1.1-0.8 (m, 10H), 0.78-0.7 (d, 3H).

Succinic acid 2,5-dioxo-pyrrolidin-1-yl ester 2-isopropyl-4-methyl-cyclohexyl ester (2) To the solution of acid (1) (0.5 g, 1.9 mmol) in dichloromethane, were added *N,N'*-dicyclohexylcarbodiimide (0.4 g, 1.9 mmol) and *N*-hydroxysuccinimide (0.22 g, 1.9 mmol) and the mixture stirred overnight at room temperature. After filtration and solvent evaporation a white powder was obtained, yield: 95%. <sup>1</sup>H NMR (300 MHz, CDCl<sub>3</sub>) δ 4.77-4.68 (m, 1H), 2.85-2.81 (s, 4H), 2.54-2.46 (m, 4H), 2.01-1.94 (m, 1H), 1.88-1.76 (m, 1H), 1.73-1.62 (m, 2H), 1.55-1.33 (m, 2H), 1.22-0.82 (m, 10H), 0.75-0.7 (d, 3H).

## 7.2.2. Synthesis of 4-azido-*N*-(3,4-dihydroxyphenethyl)-2,3,5,6-tetrafluorobenzamide

### 7.2.2.1. 4-Azidotetrafluorobenzoic acid

Pentafluorobenzoic acid methyl ester (300 mg, 1.3 mmol), NaN<sub>3</sub> (129 mg, 2 mmol) were mixed in acetone/water in 2/1 ratio. The mixture was refluxed for 3 h. Afterwards, it was evaporated under reduced pressure and water was added. The precipitate was washed with water several times and dried. Then it was dissolved in 10 % NaOH water/methanol solution and stirred for 4 h. acidified to pH 5 and extracted using CH<sub>2</sub>Cl<sub>2</sub>. The organic layer was washed with water and evaporated to obtained title compound as white precipitate. <sup>1</sup>H NMR (300 MHz, DMSO-*d*<sub>6</sub>): s = 11.3 ppm (1 H). MS (ESI): *m/z* (%) = 258 [M+Na]<sup>+</sup>

### 7.2.2.2. *N*-Succinimidyl 4-azidotetrafluorobenzoate

A solution of 4-azidotetrafluorobenzoic acid (234 mg, 1 mmol), *N*-hydroxysuccinimide (115 mg, 1.00 mmol), and dicyclohexylcarbodiimide (211 mg, 1.02 mmol) in DCM (6.5 mL) was stirred at room temperature overnight. The mixture was filtered. The filtrate was evaporated and the product was purified by flash-column chromatography to give 317.6 mg (95 % yield) as a colorless solid. <sup>1</sup>H NMR (300 MHz, DMSO): d = 2.91 ppm (4 H, s). MS (ESI): *m/z* (%) = 355 [M+Na]<sup>+</sup>.

### 7.2.2.3. 4-azido-*N*-(3,4-dihydroxyphenethyl)-2,3,5,6-tetrafluorobenzamide

To a solution of dopamine hydrochloride (113.4 mg, 0.6 mmol) in DMF (4 mL) were added TEA (108.4 mL, 0.77 mmol) and *N*-succinimidyl 4-azidotetrafluorobenzoate (200 mg, 0.6 mmol). The mixture was stirred overnight at room temperature under argon. Then water was added, and the resulting precipitate was filtered and washed with water several times and then dried to give 203 mg (91.4 % yield) of white powder. <sup>1</sup>H NMR (300 MHz, DMSO-d<sub>6</sub>): δ = 8.96–8.92 (t, 1 H, amide), 8.80 (s, 1 H, OH), 8.74 (s, 1 H, OH), 6.65–6.13 (m, 2 H, arom) 6.49–6.46 (d, 1 H, arom), 3.42–3.36 (q, 2H CH<sub>2</sub>NHCO), 2.65–2.60 ppm (t, 2 H, CH<sub>2</sub>).

## 7.3. Synthesis of nanoparticles

### 7.3.1. Nanodiamonds (NPs)

#### 7.3.1.1. Formation of ND-PFPA

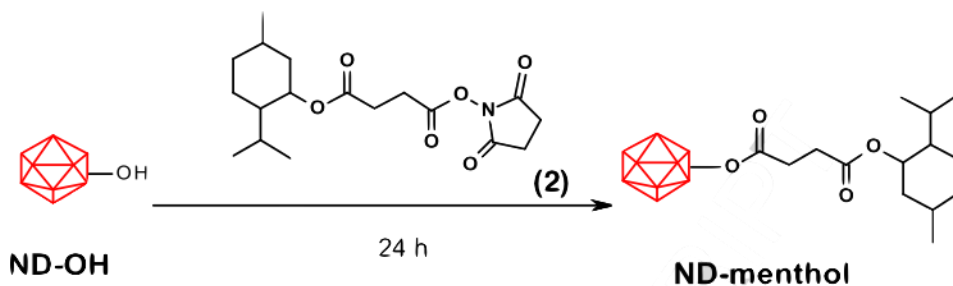
A suspension of ND-OH particles in anhydrous acetonitrile (10 mg in 5 mL) was added to a solution of ligand 4-azido-*N*-(3,4-dihydroxyphenethyl)-2,3,5,6-tetrafluorobenzamide in acetonitrile (10 mg) and stirred at room temperature for 24 h. The formed ND-PFPA particles were isolated by centrifugation at 10 000 rpm, purified through four consecutive wash/centrifugation cycles at 10 000 rpm with acetonitrile and ethanol, and finally oven dried at 50 °C for 24 h.

#### 7.3.1.2. Photochemical linkage of glycans to ND-PFPA

ND-PFPA (in anhydrous acetonitrile (1 mg mL<sup>-1</sup> in 200 μL) was mixed with an aqueous solution of the respective glycans (Figure 1) (1 mg mL<sup>-1</sup> in 400 μL) in a quartz cuvette. The mixture was irradiated with a UV lamp (Hamamatsu, 2 mW cm<sup>-2</sup>) for 30 s under vigorous stirring. The resulting glycan-NDs were isolated by centrifugation at 10 000 rpm for 15 min. In order to remove excess mannose, three additional washing/centrifugation cycles at 10 000 rpm with water were performed.

### 7.3.1.3. Preparation of menthol-modified NDs (ND-menthol)

Menthol derivative (2) (10 mM), was dissolved in 5 mL water and added to a suspension of ND-OH particles in water (10 mg in 5 mL). The solution was stirred at room temperature for 24 h under nitrogen. The resulting ND-menthol particles were isolated by centrifugation at 10.000 rpm, purified through four consecutive wash/centrifugation cycles at 10.000 rpm with ethanol, and water and finally oven dried at 50 °C for 24 h.



## 7.3.2. Gold nanoparticles (Au NPs)

### 7.3.2.1. Synthesis of gold nanorods (Au NRs)

Au NRs were synthesized according to a seed-mediated, surfactant-assisted procedure adapted from the works of El-Sayed<sup>1</sup> and Murphy<sup>2</sup> and co-workers. Seed solution was prepared by mixing HAuCl<sub>4</sub> (10 mM, 125 μL) with an aqueous solution of CTAB (0.2 M, 5 mL). To this solution was added ice-cold NaBH<sub>4</sub> (0.01 M in water) and the solution was stirred for 5 min. The resulting seed solution became brownish yellow, and aged for 5 min at room temperature before use. For the growth solution, 75 μL, 85 μL or 95 μL of seed solution in order to synthesize Au NRs with longitudinal plasmons at 700, 800 and 900 nm, respectively, were added to of 10 mM AgNO<sub>3</sub> and 500 μL of HAuCl<sub>4</sub> (10mM) and mixed with 5mL of water and 5mL of CTAB (0.2 mM) solution. The solution was acidified to pH 3-4 with 200 μL of 1% HCl, then 60 μL of 0.1 M ascorbic acid solution was added. Finally 48 μL of seeds was injected into the growth solution. Reaction was performed at 25 °C without stirring. The excess of CTAB surfactant was discarded from the final product by centrifugation at 10000 rpm for 30 min and then the precipitate was re-dispersed in 10

mL of DI water to yield Au NRs in a concentration of 10 nM. The concentration was derived spectrophotometrically from the extinction coefficient determined at 700, 800 and 900 nm longitudinal plasmons to be  $3.5 \times 10^9$ ,  $4.8 \times 10^9$  and  $6.2 \times 10^9 \text{ M}^{-1} \text{ cm}^{-1}$ .

### 7.3.2.2. Preparation of Au NRs@SiO<sub>2</sub> particles

To a solution of as-prepared 10 nM Au NRs (1 mL in DI water), 187  $\mu\text{L}$  of 20 mM tetraethoxysilane (TEOS) solution in ethanol was added. The reaction was run in a 2 mL plastic eppendorf due to a strong interaction of glassware with TEOS. The pH of the solution was adjusted to 10 by means of 10 mM NaOH. Next, vigorous stirring of horizontally placed eppendorf (belly dancer, 300 rpm) for 24 h at 23 °C was performed to properly grow the silica layer over CTAB coated AuNRs. Importantly, the concentration of CTAB prior to silica coating was carefully controlled to be precisely 1 mM. The excess of the reagents as well as simultaneously formed empty silica particles has been separated from AuNRs@SiO<sub>2</sub> by means of centrifugation (8000 rpm, 30 min). Supernatant was carefully removed and a pellet was re-dispersed in 1 mL of DI water to give 5 nM AuNRs@SiO<sub>2</sub> with a silica shell of  $20 \pm 3$  nm in thickness.

### 7.3.2.3. Loading of Au NRs@SiO<sub>2</sub> particles with verteporfin (VP)

To a solution of 5 nM AuNRs@SiO<sub>2</sub> (1 mL in DI water) were added 20  $\mu\text{L}$  of verteporfin (1 mM in DMSO). The reaction mixture was stirred for 20 h at room temperature. The formed AuNRs@SiO<sub>2</sub>-VP nanocomposite was purified by means of centrifugation (8000 rcf, 15 min) and re-dispersed in distilled water. The supernatant was used to determine the residual verteporfin concentration spectrophotometrically ( $\lambda = 692 \text{ nm}$ ,  $\epsilon = 13500 \text{ M}^{-1} \text{ cm}^{-1}$ , in PBS). 4  $\mu\text{M}$  Verteporfin were adsorbed on 5 nM AuNRs@SiO<sub>2</sub>, corresponding to  $\approx 800$  molecules per nanorod.

Estimation of Au NRs in 1 mL:

$$N_{AuNRs} = 5 * 10^{-9} \times 6.02 * 10^{23} \times 10^{-3} = 3 * 10^{12} \text{ particles per 1 mL}$$

Estimation of VP molecules per Au NRs in 1 mL:

$$N_{VP} = 4 * 10^{-6} \times 6.02 * 10^{23} \times 10^{-3} = 2.4 * 10^{15} \text{ molecules per 1 mL}$$

$$N = \frac{N_{VP}}{N_{AuNRs}} = \frac{2,4 * 10^{15}}{3 * 10^{12}} = 800 \text{ molecules}$$

#### 7.3.2.4. Synthesis of pegylated rGO-wrapped gold nanorods (Au NRs@rGO-PEG)

Carboxylated rGO (rGO-COOH) was obtained from GO as described in (ref. 33 and 34). Sodium hydroxide (NaOH, 1.4 g) and chloroacetic acid (Cl-CH<sub>2</sub>-COOH, 1 g) were added to 50 mL of GO (20 mg) aqueous solution and sonicated at 35 kHz for 2 h at 80 C to convert hydroxyl groups present on GO to COOH via conjugation of acetic acid moieties and to partially reduce GO into rGO. The resulting rGO-COOH solution was quenched with HCl (20%), washed (four times) with distilled water until neutral pH and purified by repeated rinsing/centrifugation (4000 rpm, 20 min) cycles.

Au NRs were synthesized through a seed-mediated, surfactant-assisted procedure. Seed solutions were prepared by mixing HAuCl<sub>4</sub> (10 mM, 125 mL) with an aqueous solution of CTAB (0.1 M, 10 mL). To this was added ice-cold NaBH<sub>4</sub> (0.01 M) and the solution stirred for 5 min. The resulting seed solution became brownish yellow, and aged for 5 min at room temperature before use. For the growth solution, a total 85 mL of AgNO<sub>3</sub> (10 mM) and 500 mL of HAuCl<sub>4</sub> (10 mM) were mixed with 5 mL of water and 5 mL of CTAB (0.2 mM) solution and acidified to pH 3–4 with HCl (1%). Ascorbic acid (0.1 M, 60 mL) and 48 mL of seed solution were added and the mixture left at 25 C without stirring overnight. Excess of CTAB was discarded from the final product by centrifugation at 10 000 rpm for 30 min. The precipitate was re-dispersed in 10 mL of Milli-Q water giving rise to Au NRs of a concentration of 40 mg mL<sup>-1</sup>, as determined by ICP-MS.

rGO-COOH (500 mg) was added to 20 mL of Au NRs in Milli-Q water (40 mg mL<sup>-1</sup>) and mildly stirred for 96 h at 25 °C to enable electrostatic interaction of the positively charged Au NRs with

the negatively charged rGO-COOH matrix to give Au NRs@rGO- COOH. This nanostructure was covalently modified with 10 mg of NH<sub>2</sub>PEGNH<sub>2</sub> (M<sub>w</sub> 1/4 1.5 kDa) by means of EDC (100 mL, 1 mg mL<sup>-1</sup>) chemistry under sonication (2 h, 35 kHz, 40 C) followed by dialysis (3\*2000 mL Milli-Q water), filtration through 0.2 mm filter with hydrophilic membrane and ultrafiltration (50 kDa cut-off ultracentrifuge Amicon™ filter membrane).

#### **7.3.2.5. Conjugation of Au NRs@rGO-PEG with Cy7 or FITC and Tat protein vector**

To a solution of Au NRs@rGO-PEG (1 mL, 100 mg mL<sup>-1</sup>) in Milli- Q water Cy7-NHS (10 mg mL<sup>-1</sup>) or FITC (10 mg mL<sup>-1</sup>) in DMSO was added and the solution stirred at room temperature for 48 h. The nanostructures were filtered using a 35 kDa cut-off ultracentrifuge Amicon™ filter membrane and re-dispersed in sterile PBS. To a solution of Cy7 or FITC loaded Au NRs@rGO-PEG (1 mL, 100 mg mL<sup>-1</sup>) was added HIV-1 Tat protein (30 mL, 1 mg mL<sup>-1</sup>) and the mixture left stirring at room temperature for 24 h in the presence of EDC (20 mL, 1 mg mL<sup>-1</sup>). The formed nanostructures were filtered using 35 kDa cut-off ultracentrifuge Amicon™ filter membrane and redispersed in sterile PBS.

#### **7.3.2.6. Synthesis of AuPd NPs–rGO nanocomposite materials**

Graphite was oxidized to graphite oxide by adopting Hummers and Offemann's procedure using KMnO<sub>4</sub> and H<sub>2</sub>SO<sub>4</sub> as oxidizing agents. Graphite oxide (1 g) was exfoliated in 100 mL of double distilled water using a high power ultrasonicator for 3 h to obtain a reddish brown suspension of GO nanosheets at a concentration of 10 mg mL<sup>-1</sup>. In a typical synthesis of AuPd NPs–rGO, a GO suspension (2 mL) was mixed with an aqueous solution of HAuCl<sub>4</sub> and PdCl<sub>2</sub> and kept stirring for 20 min followed by addition of ascorbic acid (4 mL, 1 M) as a reducing agent. The concentrations of HAuCl<sub>4</sub> and PdCl<sub>2</sub> were kept at 1 and 3 mM, respectively, in the entire reaction mixture. The total volume of the reaction mixture was maintained at 40 mL. The resulting mixture was stirred at 25 °C for 48 h to obtain rGO nanosheets decorated with bimetallic AuPd NPs (AuPd NPs–rGO) nanocomposite materials.

For controls, rGO nanosheets decorated with monometallic Au NPs or Pd NPs were prepared

adopting a similar procedure by mixing GO suspension (2 mL) with either aqueous  $\text{HAuCl}_4$  or  $\text{PdCl}_2$  solution. The concentrations of the monometallic precursors and the reducing agent were kept the same as in bimetallic AuPd NPs-rGO synthesis.

#### **7.3.2.7. Functionalization of AuPd NPs-rGO with polyethylene glycol (PEG)**

AuPd NPs-rGO (5 mg) and poly(ethylene glycol)bis(3-aminopropyl) ( $\text{NH}_2$ -PEG- $\text{NH}_2$ , 5 mg) were dispersed in 5 mL of deionized water and sonicated in an ultrasonic bath for 10 min at room temperature. N-(3-Dimethylaminopropyl)-N'-ethylcarbodiimide (EDC) (1 mg) was added and the mixture further sonicated for 2 h at 40 °C. Then the solution was centrifugated at 1000 rcf to remove any aggregates and purified using dialysis to remove the excess of PEG and impurities.

### **7.4. Determination of carbohydrate loading on the NDs**

A calibration curve for carbohydrate concentrations in solution was established. For this, a phenolic aqueous solution (5 wt %, 60 mL) and concentrated  $\text{H}_2\text{SO}_4$  (900 mL) was added to an aqueous carbohydrate solution (60 mL), stirred for 10 min and then an absorption spectrum of the mixture was recorded (PerkinElmer Lambda 950 dual beam) against a blank sample (without carbohydrate). The absorbance of the solution was measured at two wavelengths:  $\lambda_1 = 495$  and  $\lambda_2 = 570$  nm and the absorbance difference ( $A_{495} - A_{570}$ ) was plotted against the concentration of the corresponding carbohydrate. The quantity of surface-linked carbohydrate was determined with 60 mL of the corresponding ND particles solution in water ( $0.8 \text{ mg mL}^{-1}$ ), which was treated with phenol/ $\text{H}_2\text{SO}_4$  following the same protocol described above. ND-OH particles were treated in the same manner and used as a blank sample.

### **7.5. Lectin binding assay**

The binding affinity of the different glycol-NDs was evaluated using FITC-labeled Concanavalin A (Con A), FITC-labeled Arachis hypogaea (PNA) and FITC-labeled Lens culinaris (LENS). The glyco-NDs ( $1 \text{ mg mL}^{-1}$ , 100 mL) suspended in Tris buffer solution (pH 7.4 containing  $\text{Mg}^{2+}$ ,  $\text{Ca}^{2+}$ , NaCl) were mixed with 300 mL solutions of the different lectins ( $1 \text{ mg mL}^{-1}$ ) in Tris buffer

solution and the reaction mixture left under gentle shaking for 1 h. In order to remove non-reacted lectins, three additional washing/centrifugation cycles at 10 000 rpm with Tris buffer were carried out. Fluorescent measurements were performed using an excitation wavelength of 485 nm and an emission wavelength of 520 nm (GFP filter).

## **7.6. Fluorescence-based agglutination assay**

To 0.7 mL of *E. coli* UTI89 bacteria ( $1 \times 10^8$  cfu ml<sup>-1</sup>) TurboFP635 protein (Katushka) were added 0.3 mL of ND-mannan or ND-mannose particles solution (1 mg mL<sup>-1</sup>) and kept for 4 h at 48°C. Thereafter the solutions were dropped onto microscopic slides, covered with cover slips and sealed. Fluorescence images were recorded at an excitation wavelength  $\lambda_{\text{ex}} = 580$  nm and an emission wavelength  $\lambda_{\text{em}} = 635$  nm.

## **7.7. Biological assay**

### **7.7.1. Antimicrobial assays**

Bacterial biofilm formation: Overnight cultures of *E. coli* (NCTC 8196) and *S. aureus* (NCTC 6571) were prepared by inoculating 10 mL nutrient broth and incubating at 37°C for 18 h on a rotary shaker (Stuart Scientific) at 120 rpm. After incubation, the cultures were diluted to OD<sub>600</sub> of 0.1 in nutrient broth at a final volume of 100 mL, and a 96-well plate was set up as follows. Each assay sample required 6 wells, with another 6 wells for a negative control/blank, which consisted of 125 µL of sterile nutrient broth. Next, 110 µL of culture plus 15 µL of PBS were pipetted into next 6 wells to act as the positive growth control. In the remaining wells, the assay was set up as follows: 110 µL of culture and 15 µL of the appropriate NDs and ampicillin solutions. Sterile nutrient broth and NDs, and sterile nutrient broth and ampicillin were also set up in sets of six wells each to act as controls. The 96-well plate was incubated at 37 °C for 24 h with no agitation. After 24 h, the plate was removed from the incubator, and the supernatant of each well was removed by pipetting. The plates were subsequently allowed to dry for 15-20 min in a Class Two Microbiological Hood. Next, 125 µL of PBS was transferred into each well in order to remove any non-adhering cells. The PBS was then removed by pipetting, and the plates

were again allowed to dry in the Class Two Microbiological Hood for 15 min. All wells were stained by adding 150  $\mu$ L of 0.9% crystal violet in sterile reverse osmosis water, and the plates were incubated at room temperature for 15 min. After this time, the stain was removed by pipetting, and excess dye was washed off by manually adding and then removing 165  $\mu$ L PBS. To solubilize the crystal violet, 175  $\mu$ L of 95% ethanol was added to each well, and the plates incubated at room temperature for 30 min. The bacterial cell density was determined by the optical density of each well at 595 nm, using the negative control wells as blanks.

Viability of bacterial biofilms: The LIVE/DEAD<sup>®</sup> BacLight<sup>™</sup> assay kit was used to determine the effect of ND-menthol (100  $\mu$ g/mL) on bacterial cell viability. Overnight cultures of *E. coli* and *S. aureus* were prepared by inoculating 10 mL nutrient broth and incubating at 37 °C for 18 h on a rotary shaker (Stuart Scientific) at 120 rpm, and subsequently diluted to OD<sub>600</sub> of 0.01 in nutrient broth. ND-menthol (100  $\mu$ g/mL) was suspended in sterile nutrient broth and added to respective cultures. The cultures were incubated in the presence of ND-methanol for 3 h (logarithmic growth phase) at 37 °C at 120 rpm. After incubation, the cultures were centrifuged at 10,000 rpm for 5 min, and the supernatant solution was discarded. The resulting cell pellets were washed with 1.5 mL sterile PBS, and centrifuged at 10,000 rpm for 5 min, three times to remove media constituents that may interfere with the stain. After each wash the supernatant was discarded and the pellet collected. After the final wash in PBS, the cells were re-suspended in 1 mL PBS. On ice, equal volumes of component A and component B of the LIVE/DEAD<sup>®</sup> BacLight<sup>™</sup> stains were added to the cell suspensions and thoroughly mixed by vortexing. Next, 3  $\mu$ L of stain was added to 1 mL of culture suspension and the samples were incubated in the dark at room temperature for 20 min. Finally, 5  $\mu$ L of the stained bacterial suspension were captured between a clean microscope slide and an 18 mm coverslip. Samples were visualized using a Leica TCS SP5 Confocal Laser Scanning Microscope.

### **7.7.2. Cell culture and cellular uptake of Au NRs@rGO-PEG-FITC and Au NRs@rGO-PEG-Tat/FITC**

U87MG (human glioblastoma astrocytoma) cells were cultured in DMEM supplemented with

fetal bovine serum FBS (10% (v/v)) and antibiotics ((penicillin/streptomycin) 1% (v/v)) at 37 C in a 5% CO<sub>2</sub> atmosphere.

The U87MG cells ( $5 \times 10^4$  cells per well) were seeded on glass cover slips in 24-well culture plates and infected with Au NRs@rGO-PEG-FITC and Au NRs@rGO-PEG-Tat/FIT at  $50 \text{ mg mL}^{-1}$  for 1, 4 and 24 h at 37 C. Cells were washed twice with PBS, and treated using next protocol: staining with 0.05 CellMask (10 minutes, dark, 20 C), PBS 2, fixing in paraformaldehyde (4% in PBS, dark, 20 C), PBS 3, staining with  $2 \text{ mg mL}^{-1}$  Hoechst 33342 (15 min dark, 20 C), PBS 2, prior mounting on microscopic slides staining by means of Fluoroshield<sup>TM</sup> with 1,4-diazobicyclo[2.2.2]octane. Experiments were carried out with a Leica AF600 LX microscope (Leica Microsystems GmbH) equipped with a HCX PL APO CS 100 / 1.40 DIC (Oil) objective, an Andor iXon DU-885 EM-CCD camera (Andor Technology Ltd) and appropriate filter cubes. The excitation/emission wavelengths (nm) were 350/460 for Hoechst 33342, 492/534 for FITC, 575/632 for CellMask.

### **7.7.3. Cellular toxicity of Au NRs@rGO-PEG**

To examine the biological effects of Au NRs@rGO-PEG on U87MG cells in terms of cell viability, colorimetric MTS [3-(4,5-dimethylthiazol-2-yl)-5-(3-carboxymethoxyphenyl)-2-(4-sulfo-phenyl)-2H-tetrazolium] metabolic activity assays were performed using a PHERAstar FS by BMG LABTECH. In brief, U87MG cells were seeded in 96-wells plate (100 mL, DMEM) at a density 15 000 cells per well. After 6 h, the medium was replaced with fresh DMEM containing Au NRs@rGO-PEG ( $1\text{--}200 \text{ mg mL}^{-1}$ ) and incubated for 48 h. The old medium was aspirated and fresh DMEM (100 mL) and MTS tetrazolium dye (10 mL, Promega) was added. After 3 h the optical density of each well at 490 nm was recorded using a microplate reader. Each sample was measured in triplicate and Au NRs@rGO-PEG and DMEM only taken as false positive controls.

## **7.8. Phothermal experiments**

### **7.8.1. <sup>1</sup>O<sub>2</sub> quantum yield estimation**

To estimate the  $^1\text{O}_2$  quantum yield ( $\Phi_x$ ) of VP and AuNRs@SiO<sub>2</sub> and Au NRs@SiO<sub>2</sub>-VP nanostructures,  $(\ln A/A_0)$  of ABDA at 378 nm was plotted vs. the photo-irradiation time and fitted to a pseudo-first-order kinetic model. The  $^1\text{O}_2$  quantum yield was estimated using methylene blue (MB) as reference ( $\Phi_{MB} = 0.52$  in H<sub>2</sub>O) according to equation 1:

$$\Phi_x = \Phi_{MB} * \frac{k_x}{I_x} * \frac{I_{MB}}{k_{MB}}$$

where,  $\Phi_{MB}$  is the  $^1\text{O}_2$  quantum yield of MB in H<sub>2</sub>O,  $k_x$  and  $k_{MB}$  the rate constants for the photoreaction of ABDA with AuNRs and MB, respectively, and  $I_x$  and  $I_{MB}$  the optical density of AuNRs and MB in H<sub>2</sub>O at 710 nm wavelengths of irradiation.

### 7.8.2. Single oxygen detection

Singlet oxygen generation was monitored through the chemical oxidation of an aqueous solution of 9,10-anthracenediylbis (methylene)dimalonic acid (ABDA) (10  $\mu\text{M}$ ) in presence of VP (4  $\mu\text{M}$ ) and AuNRs@SiO<sub>2</sub> and Au NRs@SiO<sub>2</sub>-VP each at 230 pM respectively. The decrease in the ABDA absorbance at 378 nm was first monitored under irradiation at 710 nm and a laser power of 0.5 W cm<sup>-2</sup> using a continuous laser (CW, unmodelocked MIRA-900, France) or a femtosecond pulsed titanium:sapphire laser (Chameleon model, Coherent) that delivers 100 fs pulses at a repetition rate of 80 MHz. The laser beam was focused onto a cuvette (1 cm path length and 2 mm width) containing 1 mL of solution. Irradiation was stopped at 1, 2, 5, 10, 20, 30 min and absorption spectra were recorded.

### 7.8.3. Photodynamic ablation of bacteria solutions

All bacteria were used from fresh night pre-culture (LB medium, OD<sub>600</sub> = 1.0). In a total volume of 110  $\mu\text{L}$  in 96-wells plate, bacteria (10<sup>4</sup> cfu mL<sup>-1</sup>) have been mixed with the corresponding testing compounds PBS (control), VP (5  $\mu\text{M}$ , 0.5 % DMSO), Au NRs (100 pM), AuNRs@SiO<sub>2</sub> (100 pM), Au NRs@SiO<sub>2</sub>-VP (100 pM) in a sterile PBS. Both irradiated and non-irradiated controls have been created (3 wells per condition). The laser beam diameter was adjusted exactly

to the square of the well to be  $\sim 0.3 \text{ cm}^2$ . Wells were irradiated for 10 and 30 min at  $1 \text{ W cm}^{-2}$ . The conditions of the experiment are constructed in a way to complete the treatment within 2 h to prevent long exposure of bacteria to PBS solution.

Bacteria titer assay was used to determine the residual concentration of bacteria in wells. To perform a titer assay, 10-fold dilutions of a bacteria stock  $10^4 \text{ cfu mL}^{-1}$  are prepared, and  $10 \mu\text{L}$  aliquots are dropped on the LBagar + Kanamycin plates. After an incubation period of 20 h at  $37^\circ\text{C}$  in a conventional thermostat, colonies were counted.

#### **7.8.4. Photothermal *in vitro* experiment**

*In vitro* photothermal ablation tests on U87MG cells were performed in standard 96-well plates with a continuous wave laser (Gbox model, Fournier Medical Solution, France) with a wavelength at 808 nm and power density of  $0.5\text{--}1.0 \text{ W cm}^{-1}$  for up to 10 min in the presence of rGO-PEG, Au NRs and Au NRs@rGO-PEG ( $5\text{--}40 \text{ mg mL}^{-1}$ ). Prior to irradiation, U87MG cells were incubated with the respective nanomaterial for 4 h followed by washing and post-incubation for 48 h. To examine toxic effect MTS test was performed.

#### **7.8.5. *In vivo* photothermal therapy and histology**

Studies involving animals, including housing and care, method of euthanasia, and experimental protocols, were conducted in accordance with the local animal ethical committee in the animal house (C59-00913; protocol CEEA 202012) of the University of Sciences and Technologies of Lille, under the supervision of Dr P. Mariot (59-009243).

Six-week old male Swiss nude mice (Charles River, France) were used for this investigation. The mice were housed in cages covered with air filters in a temperature-controlled room with a 12 h light/12 h dark schedule and kept on a standard diet with drinking water available ad libitum. All animal experiments were performed in accord with institutional ethical guidelines.

To evaluate the *in vivo* PTT efficiency of Au NRs@rGO-PEG- Tat/Cy7, tumor-bearing mice (subcutaneous U87MG xeno- grafts) were prepared by inoculating a suspension of  $5 \times 10^6$

U87MG cells per mouse in 50% (v/v) Matrigel. Tumor growth was monitored with caliper every two days by measuring its dimensions and calculating the volume. When the tumor grew to about 500 mm<sup>3</sup> in volume, Au NRs@rGO-PEG-Tat/Cy7 (150  $\mu$ L for 1 mg mL<sup>-1</sup> per mouse) was injected intravenously. To assure significant statistical data, 3 animals were used in each group for monitoring tumor growth. After 20 h post-injection of the nanostructures, the tumor tissue was irradiated using a portable continuous wave laser (Gbox model, Fournier Medical Solution, France) at 808 nm and power density of 0.5–2.0 W cm<sup>-1</sup> for up to 5 min, 2 times, with 2 min interval. The surface temperature of the irradiated areas of skin was controlled by Infrared Camera (Thermovision A40). 24 h after irradiation some animals were sacrificed. Tumor progression in treated and untreated group was evaluated by measuring the tumor volume for 15 days.

*In vivo* tracking of Au NRs@rGO-PEG-Tat/Cy7 was performed with a Bruker Xtreme *in vivo* machine supplied with interline front-illuminated (FI) 16 MP CCD detector, 400 W Xenon Fluorescence illuminator (excitation wavelength range: 410–760 nm, emission filter wavelength range: 535–830 nm) and module for animal warming air 20–40 °C. The data was analyzed by high-performance Bruker Molecular Imaging (MI) software. The data represents mirror images of the mice.

For histological analysis, mice were sacrificed with cervical dislocation under anesthesia and tissues (heart, liver, kidneys, lung, lymph node, tumor), excised from the mice at day 1 post injection, were fixed with 4% neutral buffered formalin solution and embedded in paraffin according to the standard laboratory protocol. The sliced tissues were stained with haematoxylin and eosin (H&E), and images were taken using an optical microscope (Zeiss AxioImager A1) using 10, 40 and 100 objectives with normal (halogen) light and using color filter with transmission of 620–650 nm to visualize Au NRs@rGO-PEG-Tat/ Cy7.

## **7.9. Instrumentations**

### **7.9.1. Fourier transformed infrared spectroscopy**

Fourier transform infrared (FT-IR) spectra were recorded using a ThermoScientific FTIR instrument (Nicolet 8700) with a resolution of  $4\text{ cm}^{-1}$ . Dried nanoparticles (1 mg) were mixed with KBr powder (100 mg) in an agate mortar. The mixture was pressed into a pellet under 10 tons load for 2-4 min and the spectrum was recorded immediately. Sixteen accumulative scans were collected. The signal from a pure KBr pellet was subtracted as a background.

### **7.9.2. Micro-Raman spectroscopy**

Micro-Raman spectroscopy measurements were performed on a Horiba Jobin Yvon LabRam HR micro-Raman system combined with a 473 nm (1 mW) laser diode as an excitation source. Visible light was focused by a 100 objective. The scattered light was collected by the same objective in the backscattering configuration, dispersed by a 1800 mm focal length monochromator and detected using a CCD camera.

### **7.9.3. X-ray photoelectron spectroscopy**

X-ray photoelectron spectroscopy (XPS) measurements were performed in a Specs analysis chamber, equipped with a monochromatized Al  $K\alpha$  X-ray source ( $h\nu = 1486.74\text{ eV}$ ) and a Phoibos 150 mm radius hemispherical electron energy analyzer. The analyzer (constant) pass energy was set to 100 eV for survey spectra and at 20 eV for high resolution scans, with an estimated total (source + analyzer + core hole width) resolution of 0.85 eV for the latter case (for the N 1s spectra). The pressure in the analysis chamber was in  $10^{-8}$  Pa vacuum range, and an electron flood gun operating at 1 eV energy and 100  $\mu\text{A}$  electron current was used to ensure sample neutralization. Electrons are recorded at normal emission in "Large Area Mode" of the Phoibos analyzer. The data are deconvoluted by using mixed Lorentz/Gauss profiles with the CasaXPS software. The samples were prepared by casting 50  $\mu\text{L}$  aqueous suspensions of nanoparticles on a clean silicon wafer and followed by drying under room temperature.

### **7.9.4. Absorption spectra**

Absorption spectra were recorded using a Jasco V-570 UV/VIS/NIR Spectrophotometer from Jasco Int. Co. Ltd., Tokyo, Japan.

### **7.9.5. Transmission electron microscope (TEM)**

TEM measurements were performed in a FEI Tecnai G2 20 equipped with EDS micro-analysis, Gatan energy filter (EELS), electron precision and tomography.

### **7.9.6. Scanning electron microscope (SEM)**

SEM images were obtained using an electron microscope ULTRA 55 (Zeiss, France) equipped with a thermal field emission emitter and three different detectors (BSE detector with filter grid, high efficiency In-lens SE detector and Everhart–Thornley secondary electron detector). The sample was prepared by casting a concentrated aqueous solution of the material onto a silicon substrate followed by drying at 100 C for 1 h.

### **7.9.7. Confocal microscopy**

Transfected cells were washed with warm PBS, and fixed with 4% paraformaldehyde at room temperature for 15 min. Cells were then washed three times with PBS, mounted and observed using a Nikon A1-R (Nikon Instruments, Tempe, AZ) laser confocal microscope (Nikon Ph1 DLL 10\_/0.30 Plan Fluor objective) excited at 488 nm.

### **7.9.8. Thermogravimetric analysis (TGA)**

Thermogravimetric analysis (TGA) measurements were made in Al<sub>2</sub>O<sub>3</sub> crucibles in an atmosphere of nitrogen at a heating rate of 10 °C min<sup>-1</sup> using a TA Instruments Q50 thermogravimetric analyzer.

### **7.9.9. Particle size measurements**

Particle suspensions ( $40 \mu\text{g.mL}^{-1}$ ) in water were sonicated. The particle size of the nanoparticles suspensions was measured at  $25^{\circ}\text{C}$  using a Zetasizer Nano ZS (Malvern Instruments S.A., Worcestershire, U.K.) in  $173^{\circ}$  scattering geometry and the zeta potential was measured using the electrophoretic mode.

#### **7.9.10. Measurements of the photothermal effect**

All irradiations were performed in standard 96-well plates. The temperature changes were captured by an Infrared Camera (Thermovision A40) and treated using ThermaCam Researcher Pro 2.9 software. A 808 nm-CW LASER (Gbox model, Fournier Medical Solution) was used for the photo- thermal experiments. This laser was injected into a 400  $\mu\text{m}$ - core fiber which output was placed around 6 cm away from the bottom of the wells. This output was not collimated and the resulting beam divergence allowed us to illuminate uniformly up to 4 wells. This LASER also comprises a red pointing LASER with a power of less than 5 mW which allows the fine positioning of the fiber without interfering in the measurements.

## LIST OF PUBLICATION

### 1. Toward Multifunctional “Clickable” Diamond Nanoparticles

Manakamana Khanal, Volodymyr Turcheniuk, Alexandre Barras Elodie Rosay, Omprakash Bande, Aloysius Siriwardena, Vladimir Zaitsev, Guo-Hui Pan, Rabah Boukherroub, and Sabine Szunerits

*Langmuir*, **2015**, *31* (13), pp 3926–3933

DOI: 10.1021/acs.langmuir.5b00643

### 2. Highly effective photodynamic inactivation of *E. coli* using gold nanorods/SiO<sub>2</sub> core–shell nanostructures with embedded verteporfin

Kostiantyn Turcheniuk Volodymyr Turcheniuk, Charles-Henri Hage, Tetiana Dumych, Rostyslav Bilyy,<sup>c</sup> Julie Bouckaert, Laurent Héliot, Vladimir Zaitsev, Rabah Boukherroub<sup>a</sup> and Sabine Szunerits

*Chem. Commun.*, **2015**, 51, 16365-16368

DOI: 10.1039/C5CC06738C

### 3. Antimicrobial activity of menthol modified nanodiamond particles

Volodymyr Turcheniuk<sup>a, b</sup>, Viktoria Raks<sup>b</sup>, Rahaf Issa<sup>c</sup>, Ian R. Cooper<sup>c</sup>, Peter J. Cragg<sup>c, ,</sup>, Roxana Jijie<sup>a, d</sup>, Nicoleta Dumitrascu<sup>d</sup>, Lyuba I. Mikhalovska<sup>c</sup>, Alexandre Barras<sup>a</sup>, Vladimir Zaitsev<sup>b, e</sup>, Rabah Boukherroub<sup>a, ,</sup>, Sabine Szunerits<sup>a, ,</sup>

*Diamonds and Related Materials*, **2015**, *47*, 2–8

#### **4. Selective Antimicrobial and Antibiofilm Disrupting Properties of Functionalized Diamond Nanoparticles Against *Escherichia coli* and *Staphylococcus aureus***

Manakamana Khanal<sup>1</sup>, Viktoria Raks<sup>2</sup>, Rahaf Issa<sup>3</sup>, Volodymyr Chernyshenko<sup>4</sup>, Alexandre Barras<sup>1</sup>, Jose M. Garcia Fernandez<sup>5</sup>, Lyuba I. Mikhalovska<sup>3</sup>, Volodymyr Turcheniuk<sup>1,2</sup>, Vladimir Zaitsev<sup>2,6</sup>, Rabah Boukherroub<sup>1</sup>, Aloysius Siriwardena<sup>7,\*</sup>, Ian R. Cooper<sup>3</sup>, Peter J. Cragg<sup>3,\*</sup> and Sabine Szunerits<sup>1</sup>

**Particle & Particle Systems Characterization**, 2015, 32, 822–830,

DOI: 10.1002/ppsc.201500027

#### **5. Reduced graphene oxide nanosheets decorated with AuPd bimetallic nanoparticles: a multifunctional material for photothermal therapy of cancer cells**

Gitashree Darabdhara,<sup>ab</sup> Manash R. Das,<sup>\*ab</sup> Volodymyr Turcheniuk,<sup>cd</sup> Kostiantyn Turcheniuk,<sup>c</sup> Vladimir Zaitsev,<sup>de</sup> Rabah Boukherroub<sup>c</sup> and Sabine Szunerits<sup>\*c</sup>

*J. Mater. Chem. B*, 2015, 3, 8366-8374

DOI: 10.1039/C5TB01704A

#### **6. Affinity of Glycan-Modified Nanodiamonds towards Lectins and Uropathogenic *Escherichia Coli***

Volodymyr Turcheniuk<sup>1,2</sup>, Dr. Kostiantyn Turcheniuk<sup>1</sup>, Dr. Julie Bouckaert<sup>3</sup>, Dr. Alexandre Barras<sup>1</sup>, Dr. Tetiana Dumych<sup>3,4</sup>, Dr. Rostyslav Bilyy<sup>4</sup>, Prof. Vladimir Zaitsev<sup>2,5</sup>, Dr. Aloysius Siriwardena<sup>6</sup>, Dr. Qi Wang<sup>7</sup>, Dr. Rabah Boukherroub<sup>1</sup> and Prof. Sabine Szunerits<sup>1,\*</sup>

**CHEMNANOMAT**

Early View (Online Version of Record published before inclusion in an issue) 2016

DOI: 10.1002/cnma.201500229

#### **7. Plasmonic photothermal cancer therapy with gold nanorods/reduced graphene oxide core/shell nanocomposites**

Kostiantyn Turcheniuk,<sup>a</sup> Tetiana Dumych,<sup>b</sup> Rostyslav Bilyy,<sup>bc</sup> Volodymyr Turcheniuk,<sup>ad</sup>  
Julie Bouckaert,<sup>b</sup> Volodymyr Vovk,<sup>c</sup> Valentyna Chopyak,<sup>c</sup> Vladimir Zaitsev,<sup>de</sup> Pascal  
Mariot,<sup>f</sup> Natasha Prevarskaya,<sup>f</sup> Rabah Boukherroub<sup>a</sup> and Sabine Szunerits\*<sup>a</sup>

*RSC Adv.*, 2016,6, 1600-1610

**DOI:** 10.1039/C5RA24662H